Ultra-cold atomic magnetometry: realisation and test of a ^{87}Rb BEC for high-sensitivity magnetic field measurements

Michela Venturelli

A dissertation submitted in partial fulfillment

of the requirements for the degree of

Doctor of Philosophy

of

University College London.

Department of Physics and Astronomy

University College London

August 16, 2018

I, Michela Venturelli, confirm that the work presented in this thesis is my own. Where information has been derived from other sources, I confirm that this has been indicated in the work.

Abstract

The development of an experimental apparatus to produce Bose-Einstein condensates (BECs) of ^{87}Rb atoms and their application to magnetometry are discussed. Optical detection of atomic Larmor precession is a widely explored method for high-sensitivity measurements of magnetic fields. In this context, short laser/atom interaction time, atomic thermal diffusion and decoherence effects are among the main limitations. In this thesis, we overcome such problems by using spin-polarised ^{87}Rb ultra-cold atoms as the sensing element. After the atoms are polarised, a resonant pulse of radio-frequency excites Larmor precession, which is sensitive to external magnetic fields. By measuring the perturbations of the radio-frequency induced spin precession, information on the magnetic fields of interest. This is achieved by monitoring the polarisation plane's rotation of a linearly polarised resonant laser probe.

In the first part of this thesis, the building and optimisation of a laser-cooling set up to obtain a BEC in a hybrid trap is reported. In order to achieve the Phase Space Density (PSD) required for BEC, several different stages of trapping and cooling are necessary. Each phase has been implemented and optimised. The first step consists in the magneto-optical trap (MOT). Here a velocity dependent damping force and a spatially dependent confining force give the largest changes in PSD. Then atoms are loaded into a hybrid trap obtained by overlapping a quadrupole magnetic potential and a far detuned optical crossed dipole trap. The final stage for the condensation consists of forced evaporative cooling, both via magnetic and optical evaporation.

In the second part of the thesis, a general overview of the principles of optical atomic magnetometry is provided and the advantages of using ultra-cold atoms with respect

to conventional thermal vapours are discussed. The implementation, operation and a preliminary characterisation of the ultra-cold atom magnetometer are described along with the preliminary results collected. Finally, a plan for future improvements of its sensitivity is presented.

Acknowledgements

I would like to thank my supervisor, Prof. Ferruccio Renzoni, for his support, encouragement and for the many wise advice. I want also to thank Prof. Philip Jones, for being my second supervisor. I want to express my gratitude to Dr. Luca Marmugi, for his constant guidance through this long path, without which I would have been lost. Thanks also to all the people, and friends, with whom I collaborated and shared these years in the laboratory. Thanks to Dr. Arne Wickenbrock, for introducing me to the basics of the laboratory, and to the English language. Thanks to Dr. Raffaele Nolli, without whom everything would have been boring. Thanks to Cameron, for the infinite patience and availability, to Sarah, for being the perfect office companion. Thanks to Pik, for the many laughs and words of wisdom. Thanks to Krishna and Yuval, your joy and enthusiasm is a source of inspiration for me. A special thanks also to all the other people I met, that made my UCL experience unique. Each word, coffee break or drink on the stairs has enriched this experience, which I can't stop to appreciate. Thanks in particular to Robi, that has been "my rock" during all these years, and to Johnny and Chris, for their "ever present presence" and encouraging smile. I probably could have not finished this PhD without the constant support (Whatsapp-based) from across the Channel. Thanks Ste, for the endless messages that have kept me much more company than you can ever imagine. Such adventures would not even have started if there had not been such a determined and strong person in my life as Gherardo, great source of inspiration. Thanks to Vale, which has always been there. Thanks to that saint man of Sam, who supported me and trusted my abilities much more than I ever did. Thank you for your patience and your love. Finally I would like to thank my family, whose love

and affection I have felt more than ever, despite the 1,300 km that separate us. I would never have made it without your support.

Contents

List of Figures

Chapter 1

Introduction

This chapter is intended to introduce the concept of Bose-Einstein condensates and to give an overview of the physics governing these quantum objects. The variety of research fields involving the study of BECs are mentioned, and the field investigated during this PhD project is presented: how the interaction between a coherent source of light and an ultra-cold atomic sample can be an extremely sensitive sensor to detect external magnetic fields.

1.1 Bose-Einstein condensate

Bose-Einstein condensation was first predicted in 1924 following the collaborative efforts of the physicists Bose and Einstein. Inspired by Planck's work on black-body radiation, Bose's work focused on the statistics of photons [1] and on their distribution over energy levels. Einstein then extended Bose's ideas to matter [2, 3], considering a gas containing a fixed number of non-interacting, massive bosons. The result of their work is the concept of a Bose gas, governed by Bose-Einstein statistics, which describes the statistical distribution of identical particles with integer spin. Bose-Einstein condensation was theoretically hypothesized for a Bose gas which underwent a cooling process. Below a certain temperature (critical temperature), bosonic atoms would fall (or "condense") into the lowest accessible quantum state which eventually, in the limit $T \rightarrow 0$, contains all the particles in the system resulting in a new form of matter. The macroscopic occupation of the lowest energy quantum state represents a phase transition that a bosonic gas experiences under

certain thermodynamic conditions. It is the result of two important features that characterise a Bose gas: the same quantum state can be occupied by a limitless number of particles and, once in that state, the particles are indistinguishable from one another.

For an ideal Bose gas in thermal equilibrium the occupation number of an atomic state i with energy ε_i is given by

$$N_i = \frac{1}{e^{(\varepsilon_i-\mu)/k_BT}-1}, \tag{1.1}$$

where μ is the chemical potential depending on the total number of atoms N, k_B is the Boltzmann constant and T is the macroscopic temperature of the gas. The population distribution between the atomic states is dictated by the Bose−Einstein distribution function

$$f_{BE}(\varepsilon) = \frac{1}{e^{(\varepsilon-\mu)/k_BT}-1}, \tag{1.2}$$

where the total number of particles must be conserved

$$N = \sum_i N_i = \sum_i f(\varepsilon_i) \tag{1.3}$$

along with the total energy of the system $E = \sum_i f(\varepsilon_i)\varepsilon_i$. Limitations regarding the particles' distribution, which cannot be negative or diverging, imply that the chemical potential μ should always be smaller than the ground state energy ε_0. In order to better understand the idea behind the concept of BECs, as suggested in [4], it is useful to split the total atom number into two distinct populations that can exchange atoms between each other: the atoms in the condensed state (N_0) and the atoms in all other states (N_{Th}, Thermal component). The total number of atoms is given by the sum over the occupation numbers, respectively

$$N = N_0 + N_{\mathrm{Th}} = \frac{1}{e^{(\varepsilon_0-\mu)/k_BT}-1} + \sum_{i=1}^{\infty} \frac{1}{e^{(\varepsilon_i-\mu)/k_BT}-1}. \tag{1.4}$$

During a cooling process the value of μ increases, until $\mu \to \varepsilon_0$ for $T \to 0$, resulting in $N_{\mathrm{Th}} \to 0$. The behaviour of the thermal fraction of atoms during the cooling pro-

cess resembles the behaviour of a population of photons in similar circumstances: the atoms in the excited states behave as if the number of particles is not conserved. Because of this similarity, the thermal component of the atomic ensemble, that comprises all the atoms that are not in the ground state of the system, can be rewritten as

$$N_{\mathrm{Th}} = \int_0^\infty f(\varepsilon)D(\varepsilon)d\varepsilon = BV(k_BT)^{3/2}\zeta, \tag{1.5}$$

where $D(\varepsilon) = BV\varepsilon^{1/2}d\varepsilon$ is the density of states for particles, $B = 2\pi(2m)^{3/2}/h^3$ (with m being the mass particle and h the Planck's constant), V is the volume occupied by the particles, $\zeta(3/2)$ is the Riemann function, which is 2.61 [4] for a three dimensional system, and $f(\varepsilon)$ is the photon distribution function, that corresponds to Equation 1.2 in the limit $\varepsilon \gg \mu$. Substituting Equation 1.5 in Equation 1.4 and rearranging it, it is possible to calculate the number of particles in the ground state as

$$N_0 = N - N_{\mathrm{Th}} = N - BV(k_BT)^{3/2}\zeta. \tag{1.6}$$

The BEC phase transition begins when the temperature of the gas goes below a critical value T_C, which is the limit temperature when the ground-state occupation goes to zero, $N_0 = 0$. The critical temperature of an atomic ensemble depends on the spatial density $n = N/V$ and is given by

$$T_C = k_B\left(\frac{n}{B\zeta}\right)^{2/3}. \tag{1.7}$$

As the temperature T of the gas decreases below the critical temperature T_C, the thermal component N_{Th} becomes much smaller than the total number of atoms N. Since the total number of atoms is conserved, these "former thermal" particles are now populating the ground state resulting in a macroscopic occupation of the lowest state of the system, which is the signature of Bose-Einstein condensation. The occupation number in the ground state increases as the temperature goes below T_C as

$$\frac{N_0}{N} = 1 - \left(\frac{T}{T_C}\right)^{3/2} \tag{1.8}$$

until all the atoms are in the ground state ($N_0 = N$) and a pure BEC is obtained. As the atoms are cooled, the uncertainty in position increases and the atoms are conveniently described as wave packets with a thermal de Broglie wavelength

$$\lambda_{dB} = \sqrt{\frac{2\pi\hbar^2}{mk_BT}}, \tag{1.9}$$

whose value is determined by the temperature T and the mass m of the particles. The number of particles contained in a volume equals to the cube of the thermal de Broglie wavelength is known as the phase-space density

$$PSD = n\lambda_{dB}^3, \tag{1.10}$$

which fully describes the characteristics of the atom cloud by linking the spatial density of the particles n and their temperature T. Quantum effects become important when λ_{dB} becomes greater than the distance between the atoms, resulting in the formation of a coherent matter wave when the particles collapse in the lowest energy quantum state of the system at $PSD \approx 1$. In Figure 1.1, the trend of the PSD

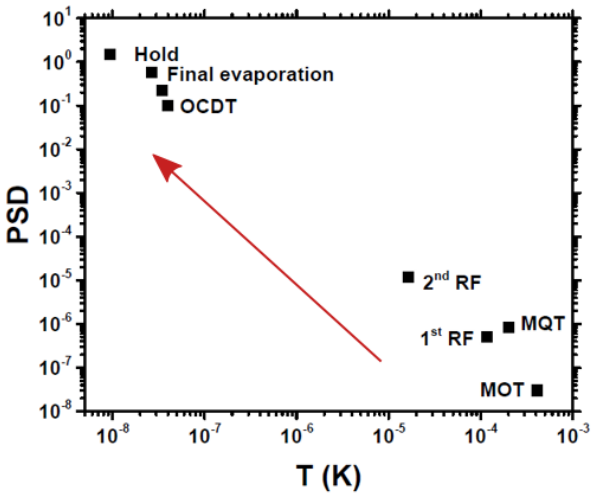

Figure 1.1: Variation of the atomic cloud PSD as a function of the temperature during the cooling process. The figure represents data acquired during the realisation of this work published in [5]. Copyright (2016) by the American Institute of Physics.

during the experimental sequence performed in this work is presented: in order to achieve the BEC, characterised by $PSD \geq 1$, the temperature of the atoms needs to be few tens of nK, with a spatial density of 10^{12} atoms/cm^3 .

The first practical step towards the creation of the BEC was the success of the first laser cooling experiment in 1978 [6]. In the following years many cooling techniques were developed but the introduction of the evaporative cooling was the decisive step in the production of BECs. Initially studied in relation to spin polarised hydrogen [7, 8], evaporative cooling was then applied to the cooling process of alkali atoms, allowing to reach a new range of low temperatures and the condensation phase transition. The first experimental proof of this new state of matter was observed in 1995 [9], when the first condensate was produced by Eric Cornell and Carl Wieman at the University of Colorado at Boulder NIST-JILA Laboratory. The first experiment was realised with ^{87}Rb atoms, but other alkali species were subsequently used for the production of condensates, like sodium [10] and lithium [11].

1.2 Realisation of a BEC

Efficiently cooling the atoms while increasing their spatial density is the aim of an optimal sequence routine, that can rapidly produce a BEC. An atomic ensemble needs to undergo a huge variation in PSD to reach the condensation phase, as shown in Figure 1.1. The PSD that characterises an atomic system at room temperature is $\sim 10^{-18}$, when the vapour density of ^{87}Rb is $\sim 10^9$ atoms/cm^3 (not represented in Figure1.1). Therefore 18 orders of magnitude of PSD needs to be covered during the process that leads to a BEC, through several different stages of confinement and cooling.

The first and bigger change in PSD is obtained via Magneto-Optical Trap (MOT) [6, 12, 13], which is realised by using 3D laser cooling and a magnetic field gradient to confine the cooled atoms. The MOT phase is usually followed by a compression phase, to increase the spatial atomic density of the cloud [14], and by a polarisation gradient cooling mechanism [15, 16] that decreases the temperature of the atomic

cloud below the Doppler cooling limit

$$T_D = \frac{\Gamma\hbar}{2k_B} \tag{1.11}$$

which is $T_D = 145.57\ \mu K$ for ^{87}Rb atoms with natural line width of $\Gamma = 2\pi \cdot 6.066$ MHz. After the sub-Doppler cooling stage, a BEC can be achieved by means of a pure magnetic trap, of an all-optical trap, or of a hybrid trap, where the atomic confinement is given by the overlapping of a magnetic and an optical trap. In these traps, the condensation is always obtained by evaporation process, which is the selective removal of the most energetic atoms of the ensemble with the subsequent re-thermalisation of the gas by elastic collisions. Forced evaporative cooling can be implemented both in the magnetic trap and in the optical trap, with different techniques.

To magnetically trap the atoms, a magnetic field gradient is created in order to confine the particles in the local minimum [17]. The standard configuration used to trap cold atoms is a magnetic quadrupole trap [18], which is usually realised with a pair of coils in anti-Helmholtz configuration. The main shortcoming of magnetic quadrupole traps is the presence of a zero magnetic field minimum in the trapping region. Atoms approaching this zero-field point can undergo non-adiabatic spin flips [19] and leave the trap. To overcome this problem many different solutions have been implemented. Among them, the use of a time-averaged orbiting potential trap (TOP) [20], where a rotating uniform magnetic field is superimposed to a static quadrupole field, and the creation of the Ioffe-Pritchard trap [21], which is a static magnetic trap with a non-zero local minimum in the magnetic field, are worth mentioning. The initial configuration of the Ioffe-Pritchard trap was then modified to obtain alternative trapping geometries (e.g. the baseball configuration [22], the QUIC trap [23], the cloverleaf trap [24]), each characterised by different degrees of efficiency and optical access, but equally able to produce tight trapping potentials. During the magnetic trap stage, RF-induced evaporative cooling is performed on the atomic sample that leads to quantum degeneration of the atoms.

A completely different path towards a BEC can be chosen if the trapping mechanism

is given by an optical dipole potential, usually constituted by a far red-detuned laser beam or by two beams in a crossed configuration [25, 26], where the evaporation is obtained by lowering the trap intensity [27]. Few advantages are entailed when optical traps are implemented. An all-optical trap does not require the presence of strong magnetic field gradients, usually obtained by coils positioned relatively close to the atoms, resulting in a less bulky setup, with more optical and mechanical access to the vacuum chamber. Also, the confining potentials given by optical traps do not depend on the orientation of the atomic magnetic dipole momentum, therefore their trapping efficiency is independent of the distribution of the atomic populations in the ground state magnetic sub-levels. The main shortcoming of optical trapping is the limit in the efficiency of evaporative cooling, given by the reduction of the trap confinement when the laser beam intensity is lowered, resulting in a less efficient re-thermalisation process. This downside can be minimised by adopting strategies that can increase the collisional rate during the evaporation process (e.g. by tuning the Feshbach resonances [28] or by adding a tight dimple potential [29] perpendicular to the dipole trap potential).

The advantages of optical and magnetic trapping can be combined to obtain a hybrid trap [30], where the two potentials are overlapped to ensure optimal confinement of the atoms and to guarantee an efficient evaporation process. In the hybrid trap configuration, the atoms are firstly magnetically trapped and then cooled via forced RF evaporation while being loaded into the optical trap. The final stage to obtain macroscopic quantum degeneracy is given by evaporation in the pure optical trap.

All the experimental ways toward BEC described so far usually require a large vacuum apparatus, where the vapour pressure in the cell must be kept below 10^{-10}mbar. These apparatus are sometimes constituted by a double chamber experimental setup [31] or by a single chamber setup with a Zeeman slower [32] as a source of pre-cooled atoms. An alternative way to create a BEC, without the need of these bulky setup, is the use of compact lithographic atom microtraps [17, 33, 34]. Strong confining magnetic fields are created by these devices via miniaturised current-carrying conductors, leading to high atomic densities and fast evaporative processes. Al-

though the number of trapped atoms is limited by the size of the trap region and the stability of the trap is affected by thermal noise, they are nowadays widely used in atomic interferometry [35] and in microgravity studies [36].

A BEC was realised in our research group in 2013 [37], by means of evaporative cooling in a QUIC trap. During my PhD, the experimental setup was modified to obtain a hybrid trap, via the addition of a far-detuned optical crossed dipole trap, in order to have more optical access to the chamber and develop application aimed at studying the properties of the condensate.
The apparatus implemented is a double chambers system where a Rubidium ampoule, attached to the first chamber, constitutes the atoms reservoir for the experiment. The pre-cooled atoms are then transferred to the second chamber via LVIS (Low-Velocity Intense Source of atoms) [38] beam, and after having been recaptured by the MOT beams they are loaded into the hybrid trap. The final stage for the condensation consists of evaporative cooling, both via magnetic evaporation and via optical evaporation. Since atomic heating and the resulting losses would inhibit high phase space densities, the optical dipole trap must be highly stable in position and in intensity. Therefore, part of our work has been to assemble a mechanically solid optical setup to stabilise the intensity of the laser beam. Condensation is achieved after an optical evaporation cooling of 6 s and the total number of atoms in the condensate is about 5×10^4. The corresponding critical temperature is about 130 nK. An overview of the experimental apparatus and a characterisation of the BEC obtained can be found in

Raffaele Nolli, Michela Venturelli, Luca Marmugi, Arne Wickenbrock, and Ferruccio Renzoni. Compact setup for the production of ^{87}Rb $|F = 2; m_F = +2\rangle$ Bose-Einstein condensates in a hybrid trap. *Review of Scientific Instruments*, 87(8):083102, 2016.

1.3 Experiments with Bose-Einstein condensates

Bose-Einstein condensation has been widely explored to investigate the property of ultra-cold quantum objects. From the very early stage of the research, when the first observation and characterisation of the BEC was made in 1995 [9], to the present time, this research field has witnessed an enormous amount of progress.

The low temperatures of BECs enabled the study of coherent matter-wave properties in weakly interacting gas, along with the investigation of the low-temperature scattering theory [39]. The first successful experiment on BEC was obtained using ^{87}Rb atoms, where repulsive interactions between atoms take place. Further experiments were performed on condensates with attractive atomic interactions in the subsequent years [11, 39, 40], culminating with the realisation of a stable ^{85}Rb BEC in 2000 [41], where the Feshbach structure allows the full control over the s-wave scattering length that characterises the dynamics of elastic collisions. The possibility to produce BECs in a variety of geometries, coupled with the ability to control atomic interactions, led to the observation of bright solitary matter-waves from BECs from 1999 [42], along with the development of optical lattices experimental techniques [43]. The tunability and the variety of configurations of optical lattices have permitted, among other applications, the study of Mott insulators [44] which have proved to be interesting systems for quantum information research [45], and the observation of direct transport of cold atoms via ratchet effect [46, 47, 48].

The coherence properties that characterise an ensemble of quantum degenerate particles have been demonstrated by interference experiment between two condensates [49, 50] and make this object the ideal candidate for the realisation of atom lasers [51, 52].

Rotating BECs [53] have proven to be extremely resourceful for studying vortices in weakly interacting superfluids. There are several techniques through which vortices can be generated and above a certain critical vortices velocity, the production of quantised vortices can be observed. The study of these phenomena brought to the characterisation of the vortex structures and to the creation of the vortex lattices [54]. Systems with multiples vortices have been generated in order to study the

overall dynamics.

Observation of degeneracy in a Fermi gas [55] has been realised by cooling fermions to extremely low temperatures. Moreover, fermions can also couple in order to create bosonic compound particles and simulate a bosonic behaviour. The concept of paired-up particles led also to the idea of creating a molecular condensate [56] and to its subsequent realisation in 2003 [57].

Furthermore, the high phase coherence and the extremely low temperature of BECs make them ideal material for high precision measurements, such as measurements of time standards (e.g. atomic fountains [58]) and of fundamental physical constants (e.g the measurement of Planck's constant via contrast interferometry [59]).

1.3.1 Atomic Magnetometry with cold atoms

A variety of methods for detecting and measuring magnetic fields have been developed in recent years, each of them characterised by different degrees of sensitivity, flexibility and ease of construction and therefore addressed to different applications. Among them, there are Optical Atomic Magnetometers (OAM), which nowadays are among the most sensitive magnetic field detectors available.

In optical atomic magnetometry, a coherent source of light is used to detect the response of polarised atomic spins to magnetic fields. Firstly proposed in 1957 by Dehmelt [60], it was experimentally observed soon after, when Bell and Bloom [61] optically detected magnetic resonances in alkali metal vapour.

In order to create a sensitive magnetic field sensor the atomic sample must be appositely prepared: the spins of the atomic ensemble firstly need to be oriented in the atomic ground state. This atomic polarisation is obtained through optical pumping [62, 63], where the photons of a resonant beam of circularly polarised light transfer angular momentum to the atomic ensemble. When exposed to a magnetic field $\mathbf{B}$ the atoms will undergo a Larmor spin precession with a frequency

$$\omega = \gamma|\mathbf{B}| \tag{1.12}$$

which is only dependent on the magnetic field strength, considering that γ, the gyromagnetic ratio, is a fundamental physical constant. The absorptive and dispersive properties of the atoms are altered by the precession motion of the spins, therefore, by analysing the transmitted light through the atomic sample, information about the precession can be obtained. Specifically, the information on the magnetic field is extracted by probing the atoms with a linearly polarised laser beam and detecting how its polarisation, which rotates while travelling through the sample, is modulated by the precessing atoms.

Magnetometers are usually characterised by their sensitivity, which mainly depends on the signal-to-noise ratio of the detected signal and on the polarisation lifetime of the atomic sample. Many of the spin relaxation processes that affect the sensitivity of an OAM operated at room temperature are completely negligible if the temperature of the atoms is drastically decreased. By lowering the macroscopic temperature of an atomic ensemble, through cooling and trapping techniques, its average thermal motion is reduced. The result is a spatially confined atomic sample with a higher local atomic density and a longer polarisation lifetime, that increase the local sensitivity of the magnetometer. Despite these advantages, the small volume of atomic traps and the finite lifetime of the atomic cloud limit the overall number of atoms interrogated by the probe beam, which results to be small compared with a room temperature magnetometer. This implies that trapped atoms, characterised by long coherence times [64, 65] and a small Doppler broadening, cannot provide the highest sensitivity to uniform magnetic fields but they are the ideal candidate for high spatial resolution measurements. Studies of the linear Faraday rotation with cold atoms have been performed since 1999 [66, 67, 68], culminating with the development of atomic magnetometers with BECs in 2007 [69], able to reach a sensitivity of the order of 1 $\mathrm{pT}/\sqrt{\mathrm{Hz}}$.

In the past few decades, the sensitivity and the accuracy of OAMs have largely improved and the current variety of alkali metal magnetometers, each one characterised by its own strength, enabled their use in applications previously dominated by other detection techniques. The spin-exchange relaxation-free (SERF) magne-

tometers are currently the atomic magnetometers that can achieve the maximum sensitivity. Firstly realised in 2002 [70], the SERF magnetometer has the potential to achieve a sensitivity of the order of 1 aT/$\sqrt{\text{Hz}}$ via suppressing the spin-exchange collisions in alkali atoms by operating at zero field and therefore maximising the atomic polarisation lifetime. Another type of ultra-sensitive OAMs are the Radio-Frequency (RF) magnetometers [71, 72, 73, 74, 75], that can reach a sensitivity of the order of sub-fT by tuning the Zeeman resonance frequency of the atoms accordingly to the frequency of the magnetic field to be measured. The sensitivity of RF magnetometers is nearly independent by the measured frequency [76] and thanks to their tunability, they can be used to detect both high frequency and low frequency signals. All-optical atomic magnetometers have been realised, in the form of coherent population trapping (CPT) magnetometers [77] and as non-linear magneto-optical rotation (NMOR) magnetometers [78], while portable magnetometers setup have been developed by using microfabricated vapour cells and extremely compact laser systems [79, 80].

Atomic magnetometers have nowadays the potential to be a relevant alternative to superconducting quantum interference devices (SQUIDs) [81, 82], which have dominated the low-frequency magnetic field measurements for the past decades. The possibility to achieve a better sensitivity and the advantage of not requiring cryogenics cooling[1], along with the possibility to perform high sensitivity measurements over a wide frequency range, make modern OAMs more adaptable and flexible devices compared to SQUIDs. OAMs are a more sensitive alternative also to fluxgate magnetometers, typically used for application where the portability of the detectors is required.

Given their versatility, atomic magnetometers have been used to address a variety of applications: ranging from biomedical applications [83], where they have been employed in nuclear magnetic resonance detection [84, 85], to investigative defence techniques, where shielded or rotating objects need to be identified [80]. Alkali atoms magnetometers have also been tested as detectors for magnetic fields gen-

[1] SQUIDs require constant cooling to reach the superconductive state, resulting in bulky detectors not ideal for portable applications

erated by biological tissues, such as the human heart [86] and the human brain [87, 88], and can be extremely resourceful instruments in biomedical imaging, where they have been proposed for obtaining a map of the dielectric properties of tissues via magnetic induction tomography [89].

In this thesis the implementation of an RF optical atomic magnetometer (RF-OAM) is presented, where the sensor is constituted by ultra-cold atoms. The combination of the advantages in terms of sensitivity and tunability of an RF-OAM along with the long coherence times and excellent spatial localisation of cold atoms results in a magnetic sensor with high sensitivity at high spatial resolution.

1.4 Thesis outline

The aim of this thesis is to give an overview of the steps taken to successfully obtain Bose-Einstein condensation of ^{87}Rb atoms and to describe the implementation of a cold atoms magnetometer. It is not possible to describe in this thesis the full theoretical details of all the physics process involved in the experiment, the focus is therefore on the technical and practical aspects of the project, which has been developed over the past few years.

In the first three chapters of the thesis, the development, realisation and characterisation of an experimental apparatus to produce Bose-Einstein condensates of ^{87}Rb atoms in a hybrid trap are described. In the last chapter, the possibility to employ ultra-cold atoms as sensors in high sensitivity atomic magnetometry measurements is investigated. In particular, a brief overview of the physics behind the concept of atomic magnetometry is presented along with a detailed description of the setup developed for this specific application, as well as the preliminary results obtained with it.

The work is organised as follows:

- Following the introduction given in the previous section, regarding BECs and their central role in many research fields, the main steps that lead to the production of a BEC are presented in Chapter 2. The physics concepts behind the hybrid trap mechanism and the forced evaporation process are introduced

along with the main fingerprints of BECs in harmonic potentials.

- In Chapter 3, the description of the BEC experimental apparatus is presented: the technical details of the vacuum chambers, of the laser system, of the crossed dipole trap and of the quadrupole trap system used in this work are reported. A detailed description of some techniques implemented to have a more efficient trapping and subsequent evaporation efficiency in order to maximise the number of atoms in the BEC is presented. The imaging systems used to observe and characterise the behaviour of atoms are illustrated at the end of this chapter.

- In Chapter 4, the optimisation of the apparatus is described through a detailed characterisation of each step of the experimental sequence performed: all the stages from the magnetic optical trap (MOT) phase to the optical evaporation in the crossed optical trap are discussed, with a particular focus on the hybrid trap potential and its peculiarities. A discussion on the results achieved with our setup is presented at the end of the chapter, along with a characterisation of the BEC obtained.

- In Chapter 5, the concept of atomic magnetometer is introduced and the theoretical background relevant for the implementation and the understanding of this detection technique is discussed. Focus is given on cold atom magnetometers features, where the advantages of ultra-cold atoms with respect to conventional thermal vapours are discussed. The implementation, operation and characterisation of the ultra-cold atomic magnetometer are described, along with the preliminary measurements performed.

- Finally, the results obtained in this thesis are summarised. An outlook to future work and improvement that can be carried out on the system in order to optimise the performance of the cold atoms magnetometers is reported.

Most of the work presented in this manuscript was realised collectively with Dr Luca Marmugi and Dr Raffaele Nolli, while Dr Arne Wickenbrock contributed to the initial stage of the experiment.

Chapter 2

Towards the realisation of a ^{87}Rb Bose-Einstein Condensate in a hybrid trap potential

In this chapter, the main steps that lead to the production of a ^{87}Rb BEC are presented. The physics concepts behind the hybrid trap mechanism and the forced evaporative cooling performed in this work are introduced along with the main fingerprints of BECs in harmonic potentials. The preliminary stages of the experimental routine (namely the MOT, the sub-Doppler cooling and the optical pumping) are not described in this chapter but a comprehensive description of the theoretical background behind these laser cooling techniques is presented in [4].

2.1 Hybrid Trap

A BEC was obtained in our experimental group [37] by means of evaporative cooling in a pure magnetic trap. Subsequently the experimental apparatus was converted to a hybrid trap setup where, with the addition of an optical potential, the benefits of both magnetic and optical trapping techniques were exploited. The coils providing axial confinement in the QUIC trap were removed and an optical trap was installed. The optical trap consisted of a tightly focused, red-detuned, high power CW laser, used in a crossed configuration, overlapping the magnetic quadrupole potential. The quadrupole potential significantly improves the loading of the crossed dipole trap

by increasing the trapping volume as atoms are confined not only in the crossed region but also along the dipole beams. This is of major importance for the achievement of quantum degeneracy: the high PSD achievable with evaporative cooling in the magnetic trap combined with the optical trap tight potential allow higher PSD values when the optical trap is loaded. This speeds up evaporation by increasing the thermalisation rate. This technique has been successfully demonstrated in several BEC experiments and combines the efficient magnetic trapping of cold alkali atoms with the rapid evaporation in optical dipole traps.

2.1.1 Magnetic trapping

Alkali atoms are sensitive to magnetic fields because of the interaction with the magnetic dipole moment of the unpaired electron. As a consequence, magnetically trapping these atoms is very efficient. The energy of the interaction between a magnetic dipole moment $\boldsymbol{\mu}$ and a magnetic field $\mathbf{B}$ is given by

$$V = -\boldsymbol{\mu} \cdot \mathbf{B}, \tag{2.1}$$

where $\boldsymbol{\mu} = g_F \mu_B \mathbf{F}$, with g_F the total momentum g-factor, μ_B the Bohr magneton and $\mathbf{F}$ the total angular momentum of the atom. According to Equation 2.1, an atom at a radial position $\mathbf{r}$ from the field minimum, in the state $|F, m_F\rangle$ and exposed to a magnetic field $\mathbf{B}$ with uniform radial gradient b', experiences the trapping potential given by

$$V(\mathbf{r}) = g_F \mu_B m_F |\mathbf{B}(\mathbf{r})| = g_F \mu_B m_F b' |\mathbf{r}|, \tag{2.2}$$

where m_F is the Zeeman sub-level and corresponds to the projection of $\mathbf{F}$ along the direction of the magnetic field $\mathbf{B}$. When exposed to a magnetic field, the degeneracy of the magnetic sub-states is lifted: each hyperfine state has a 2F+1 degeneracy associated with the different possible values of m_F which corresponds to different orientations of the total atomic angular momentum with respect to the quantisation axis. The magnetic energy has a linear dependence on the radial coordinate and the resultant potential has a conical shape. The force experienced by the atoms along

the radial direction in the potential given by Equation 2.2 is:

$$\mathbf{F} = -\nabla V = -g_F \mu_B m_F b' \widehat{\mathbf{e}}_\mathbf{r}, \tag{2.3}$$

where $\widehat{\mathbf{e}}_\mathbf{r}$ is the radial versor. Considering that the potential felt by the atoms is position-dependent, a magnetic field gradient can be used to spatially confine the atoms. The increasing-energy states, or low-field seeking states ($g_F m_F > 0$), can therefore be trapped in a magnetic field configuration having a local minimum. This is the idea behind the magnetic trapping performed in our experiment, where atoms are accumulated in a low-field seeking state via optical pumping in order to maximise the trap loading.

We are working with ^{87}Rb, specifically on the cycling transition between the ground state $|F = 2\rangle$ and the excited state $|F' = 3\rangle$ of the D2 line transitions. The Zeeman sub-levels of the ground state attracted to the minimum of the local field are $|F = 2, m_F = +1\rangle$ and $|F = 2, m_F = +2\rangle$, considering g_F is 1/2 for the state $|F = 2\rangle$ [90]. Using $\sigma+$ light polarisation is possible to optically pump the atoms towards the low-field seeker states and accumulate them in the sub-state $|F = 2, m_F = +2\rangle$, to achieve an efficient loading in the magnetic trap.

The requirement for a stable trapping is the adiabaticity of the interaction between the atomic magnetic moment and the magnetic field, which is guaranteed when the kinetic energy of the atom is sufficiently low. The coherence of the polarisation of the atomic sample increases when the temperature of the atoms is lowered, resulting in stable orientation of the atomic magnetic moment with respect to the field during the loading of the magnetic trap. This is experimentally obtained by cooling the atoms to sub-Doppler temperatures before transferring them in a suitable magnetic field gradient.

A magnetic field potential with a zero-field minimum imposes a strong limiting factor when the temperature of the atoms is low. At low temperature the thermal diffusion of the atoms is reduced and a large number of atoms will accumulate near the zero-field region. Trapped atoms approaching this zero field point can undergo Majorana spin flips [19] and leave the trap as a consequence of the transition into

a strong field seeking state. Therefore the presence of zero-field minimum causes atom loss and results in an unstable configuration. To overcome this problem an additional potential V_0 can be placed in the region of the zero-field thus creating a magnetic offset and giving a total potential of

$$V(r) = V_0 + \frac{1}{2}m\omega^2 r^2, \tag{2.4}$$

where m is the atom mass, r is the module of the position's vector and ω the trapping frequencies. It is noteworthy to mention that Equation 2.4 justifies the description of the magnetic trap as an harmonic trap for a small value of r, when $b'r << B_0$ where B_0 is the magnetic field that provides the additional potential. The radial oscillation has an angular frequency given by [4]

$$\omega_r = \sqrt{\frac{g_F \mu_B m_F}{m B_0}} \times b'. \tag{2.5}$$

2.1.2 Optical dipole trap

Optical dipole traps are produced by the interaction of the induced electric atomic dipole moment $\mathbf{p}$ with the spatially varying electric field $\mathbf{E}$ of an intense, tightly focused laser beam. This interaction can be represented as

$$\mathbf{p} = \alpha \mathbf{E}, \tag{2.6}$$

where α is the frequency-dependent atomic polarizability of the trapped atoms and is given by the product of the electric constant ε_0 and the electric susceptibility χ_a. The energy associated with the interaction between the induced dipole moment and the electric field is given by

$$U = \frac{1}{2}\mathbf{p}\cdot\mathbf{E} = \frac{1}{2}e\mathbf{r}\cdot\mathbf{E} = -\frac{1}{2}\varepsilon_0\chi_a E^2, \tag{2.7}$$

where E is the amplitude of the electric field, e is the electron charge and $\mathbf{r}$ represents the vector position of the atom's electron with respect the centre of mass of

the atom. Considering a radiation of angular frequency ω, propagating along the z-direction and linearly polarised along the x-axis, the associated electric field can be written as $\mathbf{E} = E_0 cos(\omega t - kz)\widehat{\mathbf{e}}_{\mathbf{x}}$. By differentiating the dipole energy in Equation 2.7, it is possible to obtain the component of the force along the direction of propagation of the radiation

$$F_z = -\frac{\partial U}{\partial z} = -ex\left(\frac{\partial E_0}{\partial z}cos(\omega t - kz) + kE_0 sin(\omega t - kz)\right) \tag{2.8}$$

To qualitatively understand how the two components of the force act on the induced dipole atomic moment, both the classical and quantum approach can be considered. On a quantitative level, the result given by the quantum approach provides a better model of the interaction and is therefore the one presented in this work. The force experienced by the induced dipole along z is calculated by using the dipole moment in terms of the components of the Bloch vector u and v

$$F_z = \frac{-eX_{12}}{2}\left\{u\frac{\partial E_0}{\partial z} - vE_0 k\right\} \tag{2.9}$$

where $-eX_{12}$ is the dipole moment associated with the transition between two states 1 and 2 and the values of the Bloch vector components u and v depend on the coherences value of the two-level system[1] and on the detuning of the radiation from the atomic resonance. The force can be expressed as a sum of two terms: the first one proportional to the gradient of the electric field, that is the dipole force, and the second one proportional to the amplitude, representing the dissipative component.
If the frequency of the electric field is red-detuned with respect to the atomic resonance, the resulting optical potential exerts a dipole force on the atoms that is attractive towards the region of high intensity, while it is repulsive if the frequency is blue detuned. The dipole force is suppressed when the detuning is zero.

[1]The off-diagonal elements of the density matrix that represent the response of the system at the driving frequency.

For large detuning ($\delta >> \Gamma$) the dipole trap potential U_{dip} can be approximated by

$$U_{dip} \simeq \frac{\hbar \Gamma^2 I}{8 \delta I_{sat}}, \tag{2.10}$$

where $\delta = \omega - \omega_0$ is the detuning of the laser frequency from the transition frequency, Γ is the transition linewidth, I the intensity of the light field and $I_{sat} = \pi hc\Gamma/3\lambda^3$ the saturation intensity for the transition. Usually, the frequency of a dipole trap is largely detuned from the resonance frequency, therefore the scattering rate can be approximated as

$$\Gamma_{sc} \simeq \frac{\Gamma^3 I}{8 \delta^2 I_{sat}}. \tag{2.11}$$

Equations 2.10 and 2.11 show how the dipole potential and the scattering rate depend on the detuning and intensity of the laser beam and therefore become intuitive to understand why dipole traps are normally characterised by large detunings and high intensities in order to keep low scattering rates for a certain potential depth. A red-detuned focused Gaussian laser beam represents the simplest configuration to create a dipole trap that attracts the atoms towards the region of high intensity, both in the radial direction and along the axis of the beam. The optical potential created by a single beam dipole trap can be well approximated by a cylindrically symmetric harmonic oscillator when the thermal energy of an atomic ensemble is much smaller than the potential depth U (which is the requirement for an efficient loading). Considering this approximation, the oscillation frequencies of the trapped atoms, respectively in the radial and in the axial direction of the Gaussian beam, are given by

$$\omega_r = \sqrt{\frac{4U}{mw^2}} \qquad\qquad \omega_z = \sqrt{\frac{2U}{mz_R^2}}, \tag{2.12}$$

where m is the mass of the trapped particle, w is the beam waist and z_R is the Rayleigh length[2]. Usually the radial and the axial trap frequencies of a single beam dipole trap are quite different from each other (commonly $z_R >> w_0$) resulting in a

[2]Calculated as $z_R = \frac{\pi w_0^2}{\lambda}$ with w_0 being the minimum waist of the laser beam when the focus is maximum.

much tighter confinement along the radial direction compared to the one along the axial direction and in an asymmetric trap. To overcome this problem an additional potential can be added along the axial direction, by means of a magnetic or optical confinement. In this work, both these solutions have been adopted by superimposing a crossed dipole trap to a magnetic quadrupole trap. It's noteworthy mentioning that, differently from the magnetic trap, the optical dipole force can confine atoms in all hyperfine states, also the high field seeking atomic sub-levels in the ground states.

2.2 Evaporative cooling

Forced evaporative cooling of a dilute atomic gas relies on the selective removal of the most energetic atoms of the ensemble and on the subsequent thermalisation of the gas by elastic collisions. In other words, forced evaporation is a process in which energetic particles are selectively pushed to leave a system with a controlled confining energy. This process results in a cooling mechanism: since the evaporating particles carry away more than the average thermal energy of the particles distribution, the temperature of the system decreases. The process can be understood by considering evaporation as a sequence of steps. At the beginning, the atoms have a Boltzmann distribution of energies, with a characteristic temperature T_1. All atoms with energies greater than a certain value $E > E_{cut} = \eta k_B T_1$ leave the trap, where η is the truncation parameter and indicates the fraction of velocity distribution removed by the evaporative process. The new distribution has a lower average energy per atom and so, after the thermalisation of the gas via elastic collisions, a lower temperature $T_2 < T_1$. If this mechanism is repeated with a lower energy cut-off than in the first step, further cooling will be provided. For many small steps, this model gives a reasonable approximation to real experiments where evaporation proceeds by continuously ramping down the cutting energy. During evaporation in an harmonic trap, atoms sink lower in the potential as they get colder, leading to an increase in the spatial density and, as a consequence, in phase-space density.

2.2.1 Evaporative cooling in a magnetic trap

We perform a first stage of evaporative cooling when the atoms are confined in the magnetic trap. For this purpose, we use RF-induced evaporative cooling of ^{87}Rb atoms confined in the quadrupole magnetic trap. By applying an RF-driving field with frequency ω_{RF}, resonant with the transition between Zeeman energy levels, the most energetic atoms can be removed. Specifically, this means that transitions between magnetic sub-levels are allowed if

$$g_F \mu_B b' r = \hbar \omega_{RF} \tag{2.13}$$

is satisfied, resulting in RF-driven transitions to unbound states with $\Delta m_F = \pm 1$. The RF signal flips the spins of the atoms, which eventually couple into untrapped states and are removed from the trap, as schematically illustrated in Figure 2.1. RF-

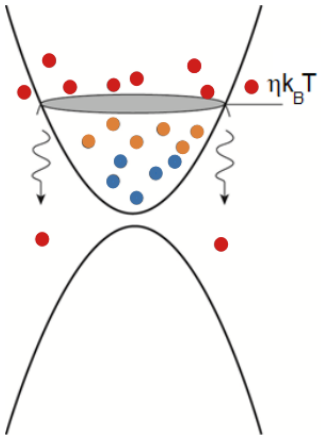

Figure 2.1: Evaporation in a magnetic trap: By applying a radio-frequency (RF) driving field, resonant with only the highest Zeeman energy levels, the most energetic atoms of the distribution can be removed. The RF signal changes the spins of the atoms, which eventually couple into untrapped states and leave the trap.

evaporative cooling in magnetic traps has the advantage to decouple the control of the trap depth from the control of the trap confinement. In this way the trapping strength remains unaltered during the process and does not compromise the elastic collisions rate between atoms. The main requirement for the application of evaporative cooling is that the thermalisation time has to be short compared to the lifetime of the trap (the magnetic trap in our case). The lifetime might be technically de-

termined by loss or heating processes, or could be intrinsically limited by inelastic collisions. Eventually, since elastic collisions are necessary for evaporative cooling, it is the ratio of elastic to inelastic collisions which sets the limitations to evaporative cooling. As long as collisions lead to re-thermalisation, they are considered 'good'. They are 'bad' when they only cause loss of atoms and no longer contribute to lower the average temperature of the sample. If the process is too quick then the situation becomes similar to that for a non-interacting gas (with no collisions) where cutting away the hot atoms does produce only losses in the trap, because of prevented re-thermalisation of the remaining atoms. There is not a proper lower limit associated with evaporative cooling and temperatures of tens nK have been reached with this technique [91, 92], using alkali metals. The real disadvantage of this technique is the loss of atoms that comes with the cooling process, which increases as the target temperature gets lower. A consistent loss of atoms can, on one side, decrease the effectiveness of the thermalisation process and, on the other side, prevent the occurrence of the condensation phase because of an insufficient number of atoms.

2.2.2 Evaporative cooling in an optical trap

Optical dipole traps are usually implemented by using a high power far-detuned laser that minimises the photon scattering rates while reaching a deep trap potential. The photon scattering rate in these traps is low enough to consider the optical potential conservative. In other words, unlike the MOT, an optical dipole trap cannot decreases the temperature of the trapped atoms, unless dedicated evaporation procedures are implemented. Therefore, a suitable adaptation of the forced evaporation introduced in the context of magnetic trapping is implemented. The evaporative cooling process in the optical trap involves a controlled progressive reduction of the trap depth by ramping down the trapping laser intensity, as schematically represented in Figure 2.2. Evaporative cooling requires a high atomic density in the trap to enable fast thermalisation by elastic collisions between atoms. Efficient evaporative cooling in an optical dipole trap is limited by the fact that lowering the trap depth causes relaxation of the trapping parameters, in particular of the trap fre-

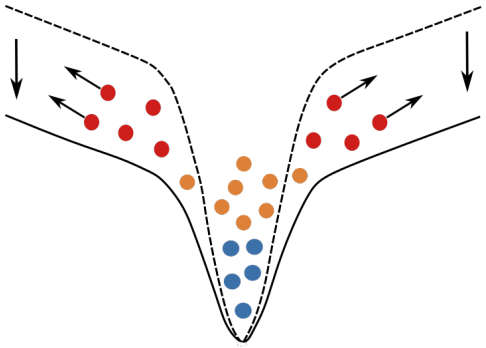

Figure 2.2: Evaporation in an optical dipole trap: By decreasing the trapping laser intensity it is possible to reduce the trap depth and remove the hottest atoms. As a consequence, the trap frequencies and the collisional rates are reduced.

quencies and hence of the collision rates, slowing down the rethermalisation stage. However, the very high phase space densities that have been observed in optical dipole traps, and the high trapping frequencies that can be found in crossed beams configurations mean that the initial collisional rates are also very high and evaporation proceeds rapidly.

2.3 A Bose Gas in a Harmonic Trap

The traps used to confine ultra-cold atoms in this experiment create an effective potential

$$U_{TOTAL} = U_{CDT} + U_{MAG} + U_g + U_0 \tag{2.14}$$

given by the combination of a crossed optical dipole trap potential U_{CDT}, a magnetic quadrupole potential U_{MAG}, the earth's gravitational potential U_g and the bias field U_0 provided via a DC magnetic offset to improve forced optical evaporation, by controlling and varying the relative position of the magnetic trap centre and the optical trap. A schematic representation of the hybrid trap geometry is presented in Figure 2.3.

Equation 2.14 can be re-written as

$$\begin{aligned} U(x,y,z) = -\frac{U^0_{CDT}}{2}\left[\frac{e^{-2(y^2+(z-z_0)^2)/w(x)^2}}{(w(x)/w_{CDT})^2} + \frac{e^{-2(u^2+(z-z_0)^2)/w(v)^2}}{(w(v)/w_{CDT})^2}\right] + \\ \mu b' \sqrt{\frac{x^2}{4}+\frac{y^2}{4}+z^2} + mgz + U_0. \end{aligned} \tag{2.15}$$

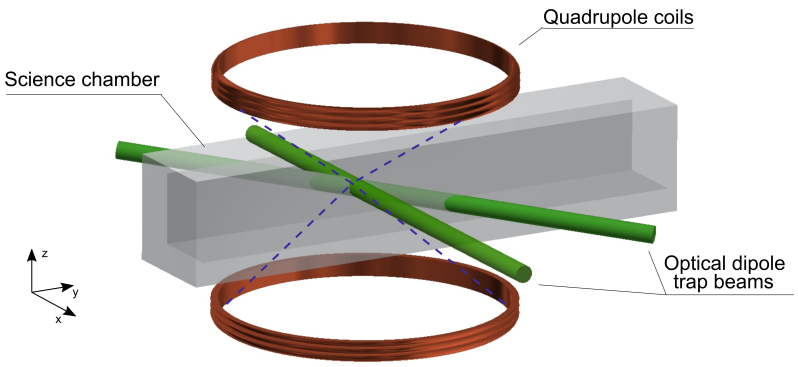

Figure 2.3: Schematic representation of the hybrid trap geometry: The solid green lines represent the dipole trap beams, that overlap at the centre of the science chamber, where the atoms are magnetically trapped by the quadrupole magnetic gradient. The displacement of the magnetic trap centre and the optical trap is along the z-direction. The magnetic trap, schematically represented by the dashed blue lines, confine the atoms in the x-y plane. Gravity acts towards $-\mathbf{z}$.

In Equation 2.15, b' is the quadrupole field gradient along $\widehat{z}$, U^0_{CDT} and w_{CDT} are the crossed dipole trap depth and waist from the zero-field point $(x=0, y=0, z=z_0)$, μ and m are the magnetic moment and mass of ^{87}Rb atom, respectively, and g is the acceleration due to gravity. The first dipole trap beam propagates along $\widehat{x}$ axis and is displaced by an amount z_0 vertically along $\widehat{z}$ below the magnetic field zero. The second beam, with a slightly different beam waist and intensity, intersects the first one with an angle θ at the point $(x=0, y=0, z=z_0)$ and lies on the plane x,y. Also, w is calculated as $w(x) = w_{CDT}\sqrt{1+x^2/x_R^2}$, with x_R being Rayleigh length for the first beam. An identical approach applies to the second beam by considering the rotated coordinates $(u,v) = (ycos(\theta)+xsin(\theta), -ysin(\theta)+xcos(\theta))$ as its reference frame. In Figure 2.4 an example of the hybrid potential used in this experiment is plotted.

At low temperatures, when the atomic maximum displacement is small compared with the spatial confinement of the trap, the potential experienced by the atoms is approximately harmonic

$$U(x,y,z) = \frac{1}{2}m(\omega_x^2x^2 + \omega_y^2y^2 + \omega_z^2z^2). \tag{2.16}$$

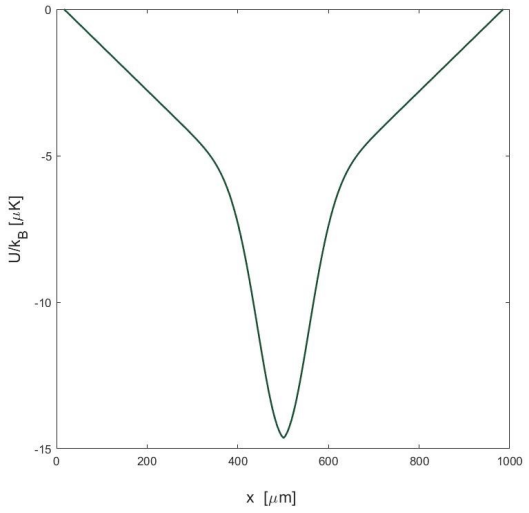

Figure 2.4: Cross section along the x-axis of hybrid trap potential, given by the superposition of a crossed dipole trap and a magnetic quadrupole trap. The maximum magnetic trap gradient is 225 G/cm while the power of the dipole trap beams are 5 W for the first beam and 3.5 W for the second one, with a beam waist in the overlapping region of 80 μm and 110 μm, respectively. The crossing angle between the first and the second beam of the dipole trap is 28°.

For a gas trapped in a 3D harmonic potential the conditions for Bose-Einstein condensation can be calculated and the critical temperature is given by [93]

$$T_c = \frac{\hbar\omega_{ho}}{k_B}\left(\frac{N}{1.202}\right)^{1/3}, \tag{2.17}$$

with N the number of atoms and ω_{ho} the geometric mean of the harmonic trap frequencies. The peak atomic density, n_0, is given by dividing the number of atoms by the effective volume of the trap $V_E = \int \exp\left(\frac{-U(r)}{k_B T}\right) d^3r$. At temperatures close to or below T_c, a semi-classical approximation is used to calculate the density of the thermal atom cloud (n_{th}) in the trap [94]

$$n_{th}(\mathbf{r}) = \frac{g_{3/2}(e^{-(U(\mathbf{r}))/k_B T})}{\lambda_{dB}^3} \tag{2.18}$$

with the corresponding peak density $n_0 = n_{th}(r = 0)$ and the function $g_{3/2}$ in the form $g_\alpha(z) = \sum_{n=1}^{\infty} z^n/n^\alpha$ [95]. The value of the atomic density obtained with Equa-

tion 2.18 is then used to calculate the PSD of the atomic cloud. The critical PSD to obtain a BEC is $\rho_C \approx 2.612$ [94].

All calculations in this section have neglected atom-atom interactions within the BEC because corrections for these interactions are typically of the order of just a few percents [96]. The properties of condensates consisting of interacting particles can be calculated using a many-body Hamiltonian for N particles in an external potential. However this method becomes impractical for systems with large N. To solve this problem a mean-field description for dilute Bose gases was proposed by Bogoliubov [97]. In dilute cold gases binary collisions are the main contribution to particle interactions. The condition for such a weakly interacting system is $\langle n \rangle |a|^3 << 1$, with $\langle n \rangle$ being the mean atomic density and a being the s-wave scattering length. This simplification allowed both Gross [98] and Pitaevskii [99] to replace the interaction potential between the particles with an effective interaction potential

$$V(\mathbf{r}-\mathbf{r}') = g\delta(\mathbf{r}-\mathbf{r}') \tag{2.19}$$

with $g = \frac{4\pi\hbar^2 a}{m}$. This resulted in the formulation of the Gross-Pitaevskii equation (GPE), with the form of a non-linear Schrödinger equation:

$$\left\{ -\frac{\hbar}{2m}\frac{\partial^2}{\partial \mathbf{r}^2} + U(\mathbf{r}) + g|\Psi(\mathbf{r})|^2 \right\} \Psi(\mathbf{r}) = \mu\Psi(\mathbf{r}) \tag{2.20}$$

which reduces to the Schrödinger equation when $g = 0$, i.e. there are no interactions. Atom-atom interactions influence many properties of condensates and are well described by a self-interaction energy, E_{int}. To estimate the effect of interatomic interactions the following expression is adopted

$$\frac{E_{int}}{E_{kin}} = \frac{N_0|a|}{a_{ho}}, \tag{2.21}$$

where N_0 is the number of condensed atoms and a_{ho} is the harmonic oscillator length. In a mean-field model this depends only on the density of the condensate, n, and the s-wave scattering length, a. For sufficiently large condensates this ratio is much larger than one and allows the ground state energy to be obtained by ne-

glecting the kinetic energy term, E_{kin}, in the GPE equation 2.20. This is called the Thomas-Fermi approximation. In this model the atomic density, which is proportional to the density distribution $|\Psi(\mathbf{r})|^2$, reflects the shape of the potential, e.g. for a harmonic potential the density would be an inverted parabola. An important indicator of the condensation phase is indeed the presence of a bi-modal distribution in the atomic cloud spacial density. When a fraction of the total number of atoms N is in the lowest quantum state, it is possible to observe a spacial density distribution given by the sum of a Gaussian distribution (corresponding to the thermal component N_{Th}) with a narrow parabolic distribution (representing the condensed fraction N_0).

Chapter 3

Experimental Apparatus

This chapter is devoted to describe the apparatus built for the production of a BEC in a hybrid trap. The technical details and the features designed to optimise the condensation process are presented, with a focus on the method used to stabilise the power of the optical trap in order to have a more efficient trapping and subsequent optical evaporation efficiency. The diagnostic technique adopted in this work to observe and characterise the behaviour of the atoms is also illustrated.

3.1 Vacuum system

In order to produce a BEC, a vacuum system capable of maintaining ultra-high vacuum (UHV) must be utilised. In this experiment, a two MOTs system is adopted, consisting of a dual vacuum chamber. This allows to separate the source of atoms, here constituted by a thermal vapour produced by a solid reservoir, from the science chamber where the BEC is produced. The need of a thermal source increases the pressure up to 10^{-8} Torr. This would prevent the realisation of BECs. Therefore, a second volume ("science chamber") decoupled from the "loading chamber" is necessary. The two chambers are connected through a differential pumping duct that allows the transport of atoms from the high pressure to the low pressure chamber. The first chamber is connected to a 20 ls^{-1} ion pump (Varian VacIon Plus 20 StarCell). Here, atoms are loaded in a Magneto-Optic Trap (MOT) from thermal vapour obtained by a solid reservoir of Rb contained in an ampoule, as anticipated. The vapour is obtained by gentle heating the ampoule to 40C. The laser-cooled

atoms are then transferred via LVIS beam into the UHV chamber where a second MOT is created[1]. The science chamber is evacuated by means of a second ion pump

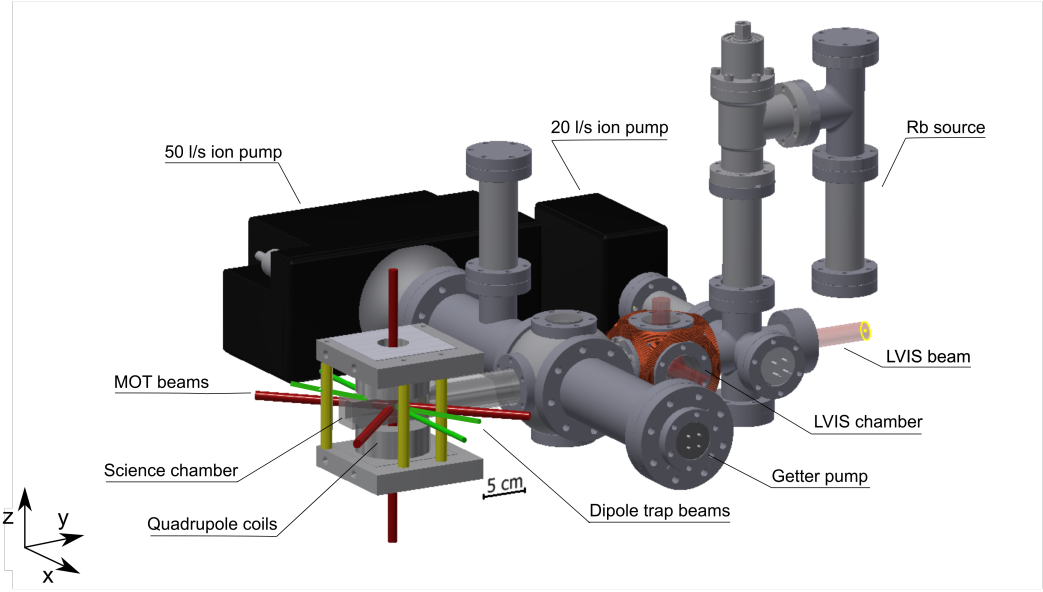

Figure 3.1: Overview of the vacuum setup

(VarianVacIon Plus 50 StarCell, with 50 l s^{-1} capacity) that achieves a pressure of $\sim 10^{-10}$ mbar and it is positioned between the differential pumping duct and the glass cell, as shown in Figure 3.1. A SAES getter pump is permanently mounted on the apparatus and is occasionally activated when baking is required. The pre-cooled atoms from the first MOT are loaded, at a rate of 20×10^6 atoms/s via LVIS beam into the second MOT, that is created in the science chamber. The science chamber is made of glass and has a cuboid shape with dimensions of 30 mm $\times$ 30 mm $\times$ 100 mm, along x,z,y -direction respectively. Optical access close to the chamber is limited due to the presence of anti-Helmholtz coils providing the magnetic quadrupole trap that confines the atoms in the x-y plane. Each coil is made with a total of 170 turns of copper wire (1 mm diameter with a thin enamel coating), arranged in 12 layers containing 15 turns each. The internal diameter of the coil is 23 mm, while the external one is 68 mm. Cooling is required to avoid the over-heating

[1]The atomic beam goes from the loading chamber to the science chamber through a 1.5 mm differential pumping hole which is drilled in the centre of the mirror used to retro-reflect one of the MOT beams in the loading chamber. The hole creates unbalanced radiation pressure that pushes the atoms in the second chamber.

of the wires and therefore the coils are connected to a water cooling system that provides a constant flow through a central hydraulic system (not illustrated in Figure 3.1). The current flowing through the anti-Helmholtz coils is actively stabilised by feedback loop provided by a current sensor (Honeywell CSNP661), a custom designed MOSFET and a proportional-integral-derivative (PID) controller (Stanford Research Systems SIM960). Three pairs of compensation coils are installed to balance out external DC magnetic fields and are realised with three mutually perpendicular square shaped coils 40 cm wide that surround the science chamber region. This setup has been especially built to maintain low background pressure in the second MOT region and therefore improve the dipole trap lifetime and have the conditions to obtain a BEC with an adequate number of atoms. Figure 3.1 is a schematic of the apparatus that we are currently using.

3.2 Laser cooling system

In order to continuously laser-cool and trap atoms in a MOT, a closed atomic transition is required. Consequently, the ^{87}Rb $D2$ line ($S_{1/2} \rightarrow P_{3/2}$) hyperfine transition $F = 2 \rightarrow F' = 3$ is used. Figure 3.2 highlights the relevant hyperfine structure and optical transitions for the species used in this experiment. The successful laser cooling of atoms requires the absolute laser frequencies to be controlled to < 1 MHz, about 6 times smaller than the natural linewidth of the cooling and repumping transitions. These transitions occur at 385 THz for ^{87}Rb and so each laser frequency must be stable to within one part in $\approx 10^8$. Such stability requires active frequency stabilisation or locking of the laser using an error signal to act as a frequency discriminant. Light for laser cooling is generated by a commercial Master Oscillator Power Amplifier (MOPA) manufactured by MOGLABS and able to provide a power up to 3W. The MOPA is composed of a tapered amplifier chip injected by an external cavity diode laser. The external cavity laser consists of a very narrowband, low loss interference filter for the wavelength selection, and an output coupler to generate the feedback. The tapered amplifier is an amplifying solid-state medium coupled to a semiconductor waveguide. This configuration provides a very high power laser

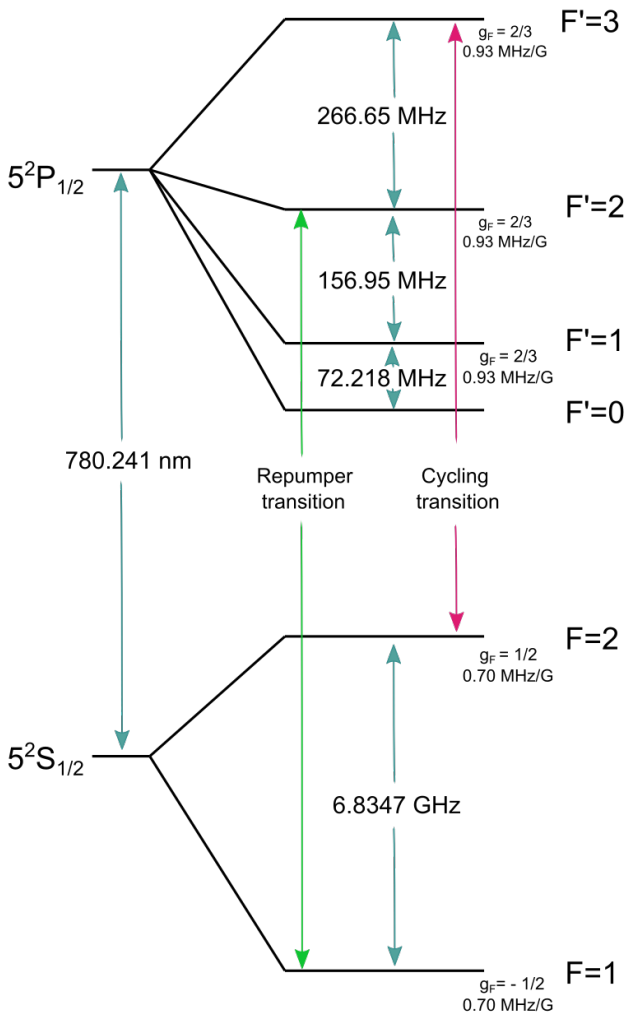

Figure 3.2: ^{87}Rb D_2 transition hyperfine structure. The relative hyperfine shifts are shown to scale within each hyperfine manifold (but visual spacings should not be compared between manifolds or to the optical splitting). The cooling and the repumper transitions are highlighted in the image. The approximate Landé g_F factors for each level are also given, with the corresponding Zeeman splittings between adjacent magnetic sublevels.

beam with a very narrowband frequency, combining the frequency stability given by the External Cavity Diode Laser (ECDL) and the high power output given by the amplifier. A fraction of the light emitted by the ECDL is used to implement the frequency stabilisation system, that exploits the modulation of both the voltage of a piezoelectric actuator in the external cavity, and the laser current. The control on the detuning of the master laser frequency is obtained via a double-pass Acousto-

Optic Modulator (AOM) system: the fraction of the diode laser beam selected for the frequency stabilisation performs double pass into an AOM before undergoing the stabilisation process. By varying the frequency of the RF input of this AOM it is possible to detune the ECDL frequency before the power is amplified by the chip. A detuning of $-4\Gamma < \Delta < +4\Gamma$ from the cooling transition can be obtained with this system. Here, Γ, is the Natural Line Width for ^{87}Rb D2 transitions and it is equal to $2\pi \cdot 6.066$ MHz [90]. The MOPA output is fibre-coupled and the power is then delivered in proximity to the experimental chambers, where the light is also used for the absorption imaging and the optical pumping beam. The output of the fibre is sent to an AOM, that controls the beam intensity, and then split into the first and second MOT beams. When delivered in the cell area the MOT beams have a diameter of 23 mm and an average intensity of 3.18 mW/cm^2. For both the first and second MOT beams, mechanical shutters (Vincent Associates- Uniblitz LSR682T0) were implemented to guarantee an efficient light closure and prevent stray or unwanted light from reaching the experimental area. A commercial Radiant Dyes Laser Accessories GmbH ECDL laser provides 50 mW of light for the repumping. The frequency stabilisation of the repumper laser is based on a frequency modulation lock, realised by a commercial system integrated in the laser controller. This mechanism relies on Doppler-free saturated absorption spectroscopy and it is realised by modulating both the piezo voltage, controlling the laser cavity length, and the laser current.

3.3 Optical dipole trap laser

In this experiment, attractive optical potentials are obtained from two beams derived from a single Yb fibre laser (IPG ELR-20-LP-SF) capable of emitting 20 W at 1070 nm. Figure 3.3 shows how the optical trap is implemented in the experiment. Light from the IPG laser passes through an optical isolator (Thorlabs IO-5-1064-VHP) to avoid back-reflection in the optical fibre and then, after the beam waist is suitably reduced by a telescope, through an AOM (Isomet M1080-T80L), which is driven by two RF generators, a Rohde & Schwarz SMF100A and a Marconi Instruments

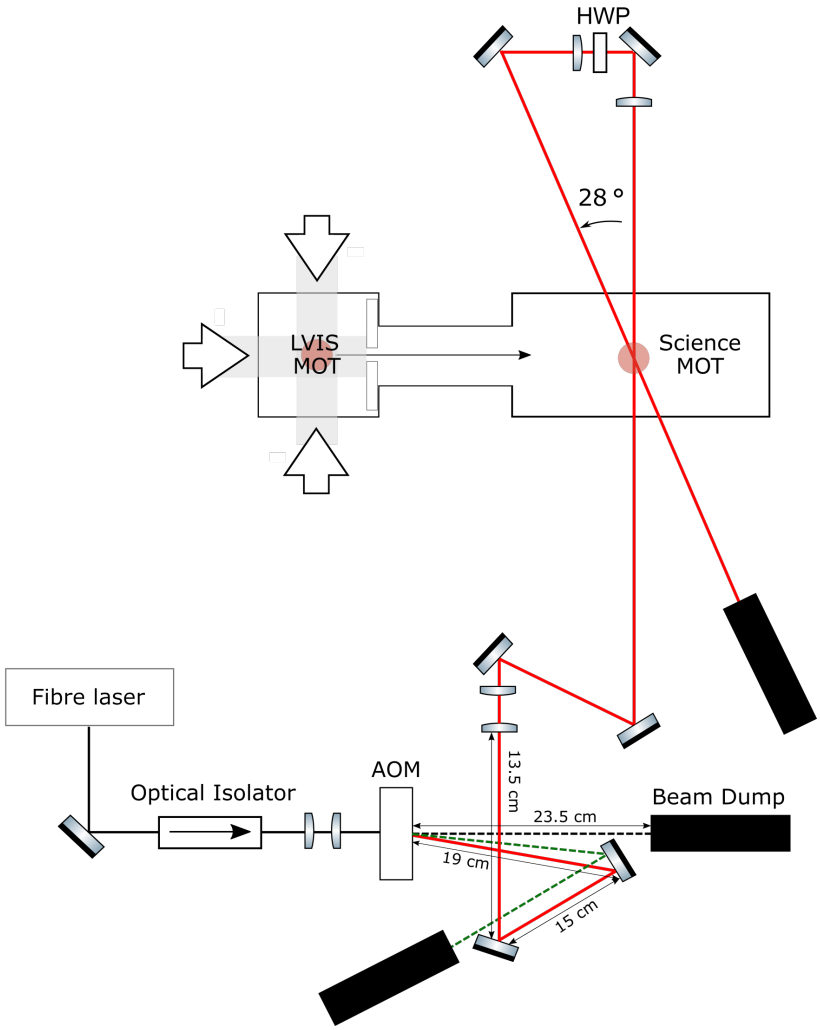

Figure 3.3: Crossed dipole trap setup: the optical path of the dipole trap laser beam (solid red line) is shown in the figure. The dashed black line represents the zero order diffracted by the AOM, while the dashed green line is the first order of the dummy frequency: these beams are cut via beam dump.

Signal Generator 2024. The fibre laser is operated at a constant output power, thus avoiding transients in current, which would cause delays, and the AOM is therefore used as a fast switch, as well as a controller for intensity and pointing stabilisation (see of section 3.4 for details). All the spurious diffraction orders produced by

the AOM are eliminated by using a suitable optical alignment and dedicated beam dumps (see Figure 3.3). In this way, stray light, which could potentially damage the trapping efficiency, is eliminated. For this reason, the optical path between the AOM and the lenses is rather long, roughly of the order of 0.6 m. The dipole trap beam (red solid line in Fig.3.3) is then focused with two lenses in the centre of the cell (2nd MOT position) where reaches a diameter of 80 μm. After passing through the chamber, the beam is reflected via two mirrors and focused to a waist of 110 μm in the center of the chamber, where it is overlapped to the first beam. The angle between the first and the second beam is 28 degrees. The restricted optical access to the cell dictated the choice upon the crossing angle.

Interference between the beams was noticed when the polarisations of the two dipole beams were parallel, producing a less efficient loading. A HWP (Half-Wave Plate) was placed after the cell to adjust the polarisation of the second beam, and its orientation was then optimised via dedicated tests.

3.4 Dipole trap intensity stabilisation

An essential condition to achieve a BEC via optical evaporation is a sufficiently long lifetime of the atoms in the dipole trap. To satisfy this condition, low atomic heating is required. The main heating processes in an optical trap are recoil heating, intensity and pointing instabilities, dipole force inhomogeneities and collisions with background gas [100, 101, 102]. Two of these factors are minimised by wisely choosing the experimental apparatus. Firstly, dipole force inhomogeneities are minimised by selecting a dipole trap laser able to deliver a transverse single mode emission. In other words, the dipole trap beam is a TEM_{00} mode, thus providing a wavefront with a Gaussian intensity distribution in the plane orthogonal to the propagation direction, resulting in a symmetric intensity gradient in the radial direction. Secondly, the collisions with the background particles are suppressed by implementing a pumping system able to maintain a residual background pressure of 10^{-10} mbar in the trap position. The other heating mechanisms, such as instabilities in the laser intensity and pointing direction, can be subsequently minimised

via an active stabilisation system. Variations in the laser beam intensity modify the potential energy of the trap while pointing oscillations change the trap position due to movement of the trapping potential. Both these effects result in a less efficient trapping and optical evaporation. These mechanisms might occur due to temperature drifts, thermal effects, or due to noise in the dipole trap laser output. The critical frequencies of noise, that actually affect the trap efficiency, are in the range of the trap frequencies. Noise at frequencies much higher or much lower than the trapping frequencies does not contribute to the atomic heating: the high-frequency fluctuation won't affect the atoms because they only see the time-averaged potential, whereas the atoms can follow the changing potential adiabatically if the time scale is slow compared with the trapping frequency. Thus the challenge is to suppress the intensity fluctuations in the range of the trapping frequencies and to guarantee a good pointing stability, especially when the dipole trap intensity is decreased during the evaporation process.

3.4.1 Power and Beam pointing stabilisation

To limit intensity fluctuations in the dipole trap beam, a laser intensity stabilisation system has been implemented with the aim of working both at very high and very low intensity values. As previously mentioned, the IPG fibre laser is operated at constant output power and therefore the AOM acts as an intensity controller for the dipole trap beam: by varying the intensity of the RF signal that drives the AOM it is possible to vary the power in the 1^{st} diffracted order from the AOM, which is the dipole trap beam. The intensity stabilisation implemented exploits an additional modulation on the RF signal sent to the AOM, that through a feedback loop provided by a PID controller, maintain the power in the dipole trap constant.

The intensity of the dipole trap beams is set via a LabVIEW software that modulates the output of the RF function generator via a PID controller (Stanford Research Systems SIM960). The intensity of the laser beam is monitored with a photodetector: a partially reflective mirror (reflectance $\approx 99\%$) is introduced as a first mirror after the experimental chamber and the small fraction of light (1%) transmitted through this mirror is focussed onto a photodiode (Thorlabs DET36A/M) used to measure

the intensity of the beam. The photodiode signal is sent to an AD8304 logarithmic amplifier (see the schematic in Appendix A) and subsequently to a Stanford Research Systems SIM910 JFET linear amplifier. The combination given by a logarithmic amplifier, that guarantees greater sensitivity at low laser power, and a linear amplifier, maximises the dynamic range of the feedback loop assuring a good intensity stabilisation upon all the intensity range.

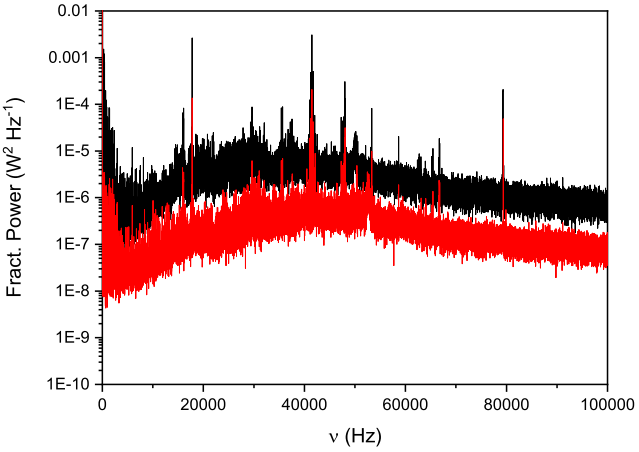

(a)

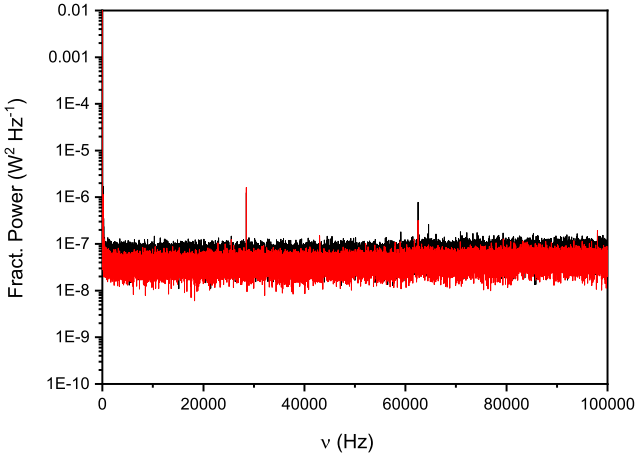

(b)

Figure 3.4: Power spectral density of the dipole trap beam intensity when the intensity is stabilised (red line) and when the intensity is not stabilised (black line), respectively in (a) low power (24 mW in the region of the trap) and (b) high power regime (2.4 W in the region of the trap). The temporal duration of each intensity profile measurements is 4s with a sampling time of 3.2×10^{-6} s.

The stabilisation is performed only on the main beam: the second beam is generated by reflection from the first one, so once the stabilisation is achieved, it will act on both branches of the dipole trap. The effect of the intensity stabilisation is shown in Figure 3.4, where the comparison between the stabilised and un-stabilised intensity of the dipole trap laser is represented for two values of beam power. In detail, Figure 3.4 shows the Fast Fourier transform of the intensity profile recorded for a fixed temporal domain. For each measurement, the intensity temporal profile of the laser has been recorded with the fibre laser constantly operating at 20A and by changing the trap intensity via modulating the amplitude of the signal delivered to the AOM. The setpoints chosen for these measurements give a dipole trap power of 2.4 W and 24 mW (in the first beam) and allow to compare how the stabilisation affects the intensity both in high power and low power regime, respectively.

Figure 3.4 shows how the stabilisation system is generally efficient in both cases but it is more effective in the low-intensity range, (where the noise reduction is 90%) than in the high power regime (the noise reduction is 50%).
The stabilisation mechanism showed in this section is not enough to ensure an efficient optical trapping. The variation of RF power supplied to the AOM during the intensity ramps causes temperature variations in the crystal of the modulator, which result in instabilities (both in beam pointing and power). Therefore we decided to upgrade our dipole trap stabilisation system via two-frequencies drive technique (see Section.3.4.1.1).

3.4.1.1 Double frequency driving of the AOM

The position stability of the dipole trap laser is a critical parameter in our experiment. In crossed optical dipole traps, where two beams have to be overlapped on a 10 μm scale, a small change of the beam position can have a dramatic effect on the trap characteristics (frequency and depth), thus causing atom loss. Of particular importance is the pointing stability during the optical evaporation, which is achieved by ramping down the laser intensity. Thermal effects in the AOM crystal has been observed, when the power of the RF is rapidly varied, resulting in a displacement of the diffracted beams. One way to circumvent the displacement of the diffracted

beams is to use a single-mode optical fibre after the AOM. A second option, which is the one we have implemented, consists in changing the frequency of the RF to compensate for the beam movement. To improve the beam pointing stability during dipole beam intensity ramps a second RF frequency is supplied to the Isomet M1080-T80L AOM. As the power of the first main RF frequency is reduced, the

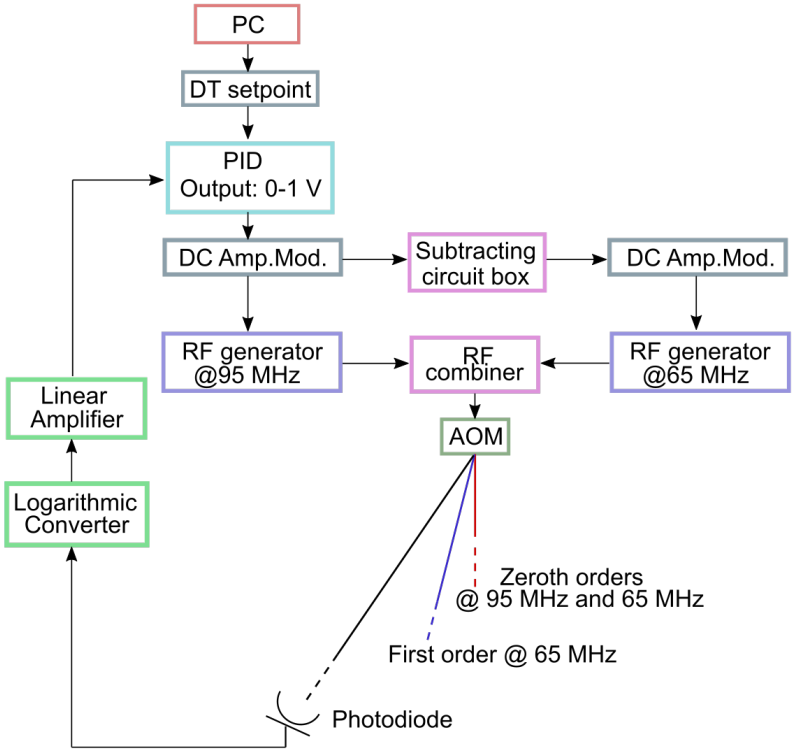

Figure 3.5: Schematic of the stabilisation system used for the crossed dipole trap configuration. The diagram shows both the power stabilisation performed via logarithmic photodiode and the beam pointing stabilisation performed via double frequencies drive of the AOM. The used frequencies are 95 MHz, for the main RF, and 65 MHz, for the dummy one.

power of a second frequency is increased to keep the total power delivered to the AOM crystal constant. The trick is to avoid ”switching on” effects by driving the AOM with a dummy frequency rather than turning it off [103] when the dipole trap is not required, thus keeping the power supplied to the AOM constant and arranging the beam optical path in such a way that the beam is discarded in this situation.

The schematic of the stabilisation system is shown in Figure 3.5. In order to ensure a constant RF power to the AOM, a circuit was realised to vary the amplitude of

the dummy signal depending on the power of the main one. The power of the main frequency is therefore set via the LabVIEW interface, (i.e.that corresponds to set the intensity of the dipole beams), whereas the power of the dummy one is automatically given by the subtraction circuit in order to deliver a constant power to the AOM. The two signals are then combined by a RF summing circuit (Mini-Circuits ZMSC-2-1+ power splitter/summer) as shown in Figure 3.5. The used frequencies

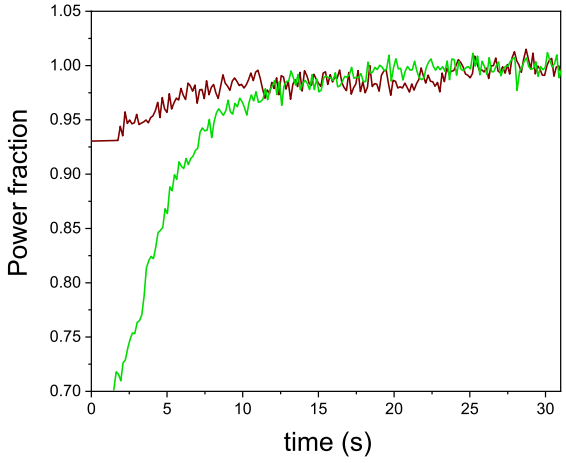

Figure 3.6: Beam power stability measurements: the power of the beam was recorded for a period of 31 s when the double frequency drive is on (red line) and when the double frequency drive is off (green line). The starting time of the acquisition corresponds to the switching on of the dipole trap beam. The measurement was performed with a beam profiler and the power is normalised to the maximum value of the beam.

are 95 MHz, for the main RF, and 65 MHz, for the dummy one. These frequencies have been chosen considering the bandwidth of the AOM in use (ISOMET M1080-T80L). We have considered the AOM efficiency peak and then we have chosen the two frequencies that allowed us to have the biggest angular separation between the same order, in the limits of the bandwidth. The key point in this choice is indeed to have enough power in the beam with 95 MHz and at the same time being able to discard the beam at the dummy frequency (65 MHz) with a proper alignment and positioning of the beam dumps. We have tested the effectiveness of our two frequencies drive system with a series of measurements, shown in Figure 3.7 and 3.6. The beam centroid coordinates and power were recorded using a CinCam CCD

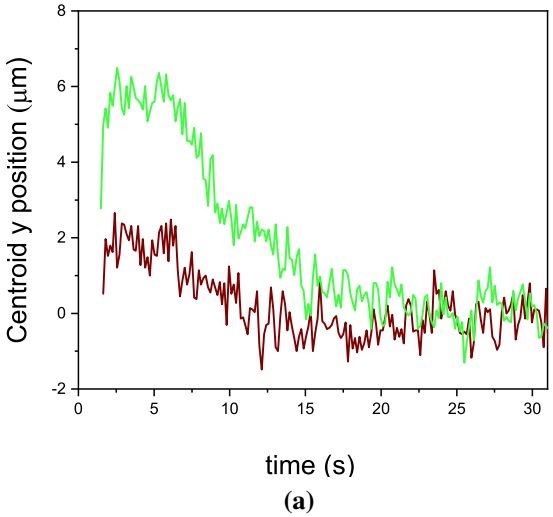

(a)

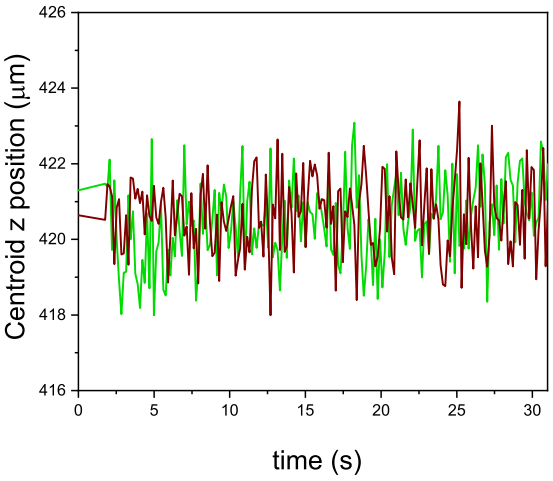

(b)

Figure 3.7: Beam pointing stability measurements: a) The position of the beam centroid was recorded on the horizontal plane (parallel AOM's plane) for a period of 31 s when the double frequency drive is on (red line) and when the double frequency drive is off (green line). The starting time of the acquisition corresponds to the switching on of the dipole trap beam. The analogous measure was carried out on the vertical plane (orthogonal AOM's plane) and it's shown in b). The measurements were performed with a beam profiler and represent the beam displacement in the region of the atoms.

beam profiler (CINOGY TECHNOLOGIES) with an acquisition time of 30 seconds. Previous the double frequency implementation, the AOM was driven by an RF signal generator at its central frequency (80 MHz). The efficiency of the AOM and therefore the beam power (referred to the optical dipole trap beam in the cell

position) with the two frequency system is 2.2% lower than in a single frequency setup. This is probably due to the fact that the maximum AOM efficiency is reached for RF=80 MHz and also because the dummy RF is not totally suppressed. Without the two-frequency drive, the power of the laser goes from 70% to 100% of its full power working point in a 10 s transient. With the implementation of this technique, the transient in power lasts just over 7 s and it is drastically reduced in amplitude: the power of the laser goes from 93% to 100% of its full working power. The beam pointing instability (in the trap position) is reduced to a third of the value obtained without the dummy frequency on the horizontal direction (parallel AOM's plane). The effect is so dramatic because the optical path between the AOM and the trap position is 91 cm long. Accordingly, a small shift at the AOM position led to a big displacement in the DT position. The displacement in the vertical position doesn't change with the two-frequency setup. Figure 3.7 b) shows that along the z-axis there is no transient in the beam position. Therefore with regard to the vertical direction, the two frequencies driving technique does not introduce a real improvement to the beam pointing stability.

3.5 Magnetic field offset

Among the most severe causes of losses in a quadrupole trap configuration, there are Majorana spin-flip collisions (discussed in section 2.1.1). As these Majorana transitions occur at the centre of the quadrupole potential the coldest atoms are lost. As a consequence, both heating and losses are observed, resulting also in a reduction of the lifetime of the trapped gas. Majorana losses can be slightly mitigated by adiabatically expanding the trap with the consequent decrease of loss rate, but at the expense of a lower elastic collision rate. We have therefore decided to adopt a different solution by introducing a magnetic offset during the optical evaporation. The relative position of the dipole trap beam and the magnetic trap centre is the main parameter that must be taken into account in the alignment of the dipole trap. In fact, in the context of Majorana spin-flips, the overlapping of the magnetic gradient minimum with the centre of the optical potential will lead to an enhancement of the

spin-flips and hence to a reduced efficiency of the forced evaporation. The relative position of the dipole trap and the magnetic field zero was optimised via alignment of the laser trap beams. In detail, a displacement of one waist was imposed in the vertical direction, so that the distance between the centre of the optical and the magnetic potentials is $\approx$ 50 μm. Whereas, during the optical evaporative cooling, the displacement of the quadrupole potential and its minimum was controlled with a pair of coils that provide a uniform DC magnetic field in the trapped atoms region. This additional pair of coils are mounted on top of the quadrupole coils and produce a DC magnetic field along the z-axis. The magnetic offset is switched on via a LabVIEW interface, that activates a switch that let the current flows into the coils.

3.6 Experimental control

During each experimental routine a series of precisely timed processes must be performed in sequence. In order to ensure both the correct execution of the experiment and an adequate data acquisition, a stable and reliable control system must be implemented. This control is realised using a bespoke LabVIEW software. A combination of analog and digital output channels, whose interface is shown in Figure 3.8, provide complete control over the experimental hardware (i.e. changing the magnetic field gradient or controlling the laser light). A National Instruments CA-1000 data acquisition board through a PCMCIA connector is specifically used for this purpose, where TTL signals are usually used as a trigger for electronic instrumentation, as well as for the high-demanding controls of the setup. The low-demanding diagnostic of the experiment is performed by multiple LabVIEW interfaces, that read and analyse signals from a National Instruments USB 6009 data acquisition board. Direct connections to cameras allow imaging diagnostics.

3.7 Diagnostics

We employ two commonly used imaging diagnostic techniques to monitor our trapped atomic cloud. Fluorescence from the atoms in the MOT beams is observed both in the science and in the loading chambers, allowing a real-time assessment of the MOT status and loading rate. In the science chamber, absorption imaging is

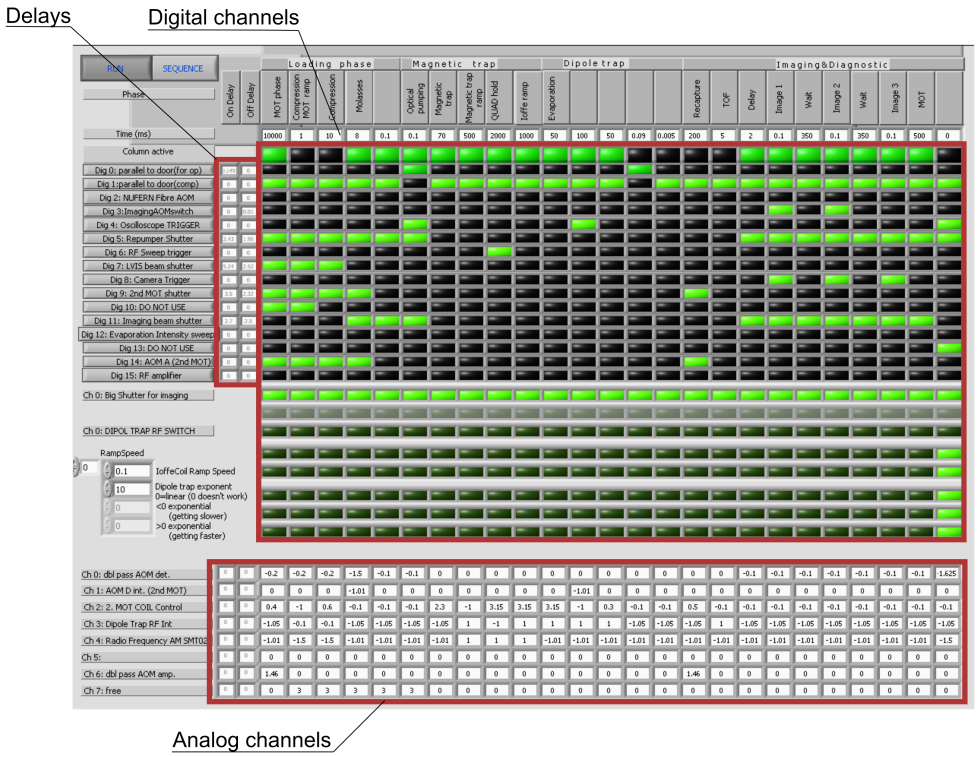

Figure 3.8: Labview software interface implemented to control and run the experimental routine. Digital and analog channels are highlighted, along with the delays that can be inserted on each channel in order to synchronise the computer and the instrumentation. Digital channels have two possible values (0-5 V) while Analog channels output ranges between 0-10 V. Each column represents a different phase of the sequence.

used to measure both the optical depth and the cloud size after a short time-of-flight allowing the characterisation of the cloud, via atom number and temperature of the sample.

3.7.1 Fluorescence detection

In the science chamber, fluorescence light emitted by atoms in the MOT is monitored using a Manta camera (ALLIED Vision Technologies) whereas, in the loading chamber, the camera is a Vantage CCD. Fluorescence detection can be used to optimise many parameters associated with the laser cooling stage of the experiment, as for example the atoms loading and transfer from the first to the second cell. A LabVIEW interfaces was created to monitor the MOT loading in the science chamber and measure the atomic flux from the LVIS. Using recapture measurements [104],

whereby MOT beams are pulsed-on again to observe the atomic cloud at any stage of the experimental routine, it is possible to measure the fraction of atoms transferred from the MOT into the magnetic trap or into the optical trap. However, after the dipole trap loading process, we use absorption imaging as our diagnostic.

3.7.2 Absorption imaging

We employ Time-Of-Flight (TOF) detection to measure the the velocity distribution of cold atoms when they are released from the trap and we adopt absorption imaging to observe their spatial distribution. A probe beam with total power of 100 μW is brought to resonance with respect to $|5^2S_{1/2}, F = 2\rangle \rightarrow |5^2P_{3/2}, F = 3\rangle$ transition of ^{87}Rb atoms using an AOM. The beam is then delivered in proximity of the science chamber via a single mode polarisation maintaining optical fibre and then expanded to a waist size of 18 mm using a spherical lens. Through a beam splitter the probe beam is overlapped with the vertical MOT beams (along z-direction) and aligned through the centre of the atom cloud, as schematically shown in Figure 3.9. As the

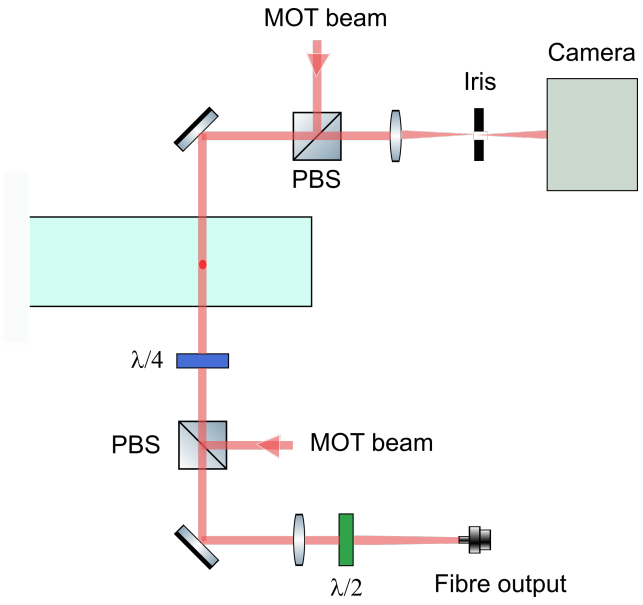

Figure 3.9: Absorption imaging optical layout: atoms are illuminated with the probe light in the vertical plane. The probe light is then passing through an iris and then focussed down onto a CCD camera using a pair of lenses.

light interacts with the atoms, the cloud absorbs and scatters photons. By imaging the remaining light on a CCD camera it is then possible to extract the column density

of the cloud along with its spatial profile. The resulting two-dimensional image corresponds to the three-dimensional cloud density integrated along the direction of the imaging beam. The centre of the atom cloud is imaged onto a CCD camera (PCO-PixelFly). Before the camera, the imaging beam is focused and an iris is positioned in the focus position to remove all the stray light from the repumper and cooling beams that could reach the CCD sensor. The intensity of the absorption probe beam is kept much below the saturation intensity so that the probe beam absorption is proportional to the atom number density in the cloud and independent of the probe beam intensity. The optical depth OD, defined as

$$I = I_0 \exp(-OD(x,y)) \tag{3.1}$$

is a measurement of the change in intensity I of the outgoing imaging beam (with initial intensity I_0) as it passes through the cloud and can be written in terms of the atom column density, $n(x,y)$, and the absorption cross-section, σ, as

$$I = I_0 \exp(-n(x,y)\sigma), \tag{3.2}$$

where the absorption cross-section is given by

$$\sigma = \frac{\sigma_0}{1 + 4\left(\frac{\Delta}{\Gamma}\right)^2 + \frac{I_0}{I_{sat}}} \tag{3.3}$$

and, σ_0, is the on-resonance cross-section given by

$$\sigma_0 = \frac{\hbar\omega\Gamma}{2I_{sat}}. \tag{3.4}$$

Taking an image of an atomic cloud in the experiment is a three-step process: first, an absorption image of the atom cloud is taken ("object image", I_{obj}). This is followed by a "reference" (I_{ref}) image recorded by applying the same imaging laser light, as for the object image, but after the cloud left the field of view. And then, a

dark frame (I_{bg}) is recorded for background subtraction, when an image is acquired without the imaging beam. The optical density at coordinate (x,y) can be obtained via normalisation

$$OD(x,y) = -\ln T(x,y) \tag{3.5}$$

with

$$T(x,y) = \frac{I_{obj}(x,y) - I_{bg}(x,y)}{I_{ref}(x,y) - I_{bg}(x,y)}, \tag{3.6}$$

where $T(x,y)$ is the normalised transmission through the cloud at a certain pixel position. Most physical properties, such as atom number, temperature, cloud shape and size, are obtained by analysis of the optical density OD (x,y). The full calculations to determine the cloud parameters can be found in [105, 106]. In this thesis the main results are presented. In Equation 3.3, Δ is the detuning of the laser field from the atomic resonance. Γ is the natural decay rate of the excited state and, I_{sat} is the saturation intensity. Considering that $OD(x,y) = n(x,y)\sigma$, it is possible to estimate the atom number via

$$N = \int_{-\infty}^{\infty}\int_{-\infty}^{\infty} n(x,y)dxdy = \frac{1}{\sigma}\int_{-\infty}^{\infty}\int_{-\infty}^{\infty} ODdxdy \tag{3.7}$$

to get the total atom number.

We assume a non-interacting cloud that obeys Boltzmann's statistics. Supposing we have N particles in the cloud, then, the mean number of particles in the E_i^{th} energy state at temperature T is given by

$$n_i = \frac{N}{Z} exp\left(-\frac{E_i}{k_B T}\right) dE. \tag{3.8}$$

We assume that these particles have motions that can fit the classical picture. Thus, we can express the kinetic energy of such particle as

$$E_k = \frac{1}{2}mv^2. \tag{3.9}$$

In the TOF experiments, we cannot directly measure the velocities of each individual atoms in the cloud. However, we can measure the overall expansion of the cloud in terms of its size in the x and y directions. If we assume that the cloud has an initial size of zero (treating it as a mathematical point), and its centre-of-mass has no initial velocity, we can apply simple kinematics equation that relates the speed of the particle with the distance moved. So we express the number distribution in terms of differential velocity instead of energy by manipulating 3.9 and considering $v = x/t$:

$$n_i = \frac{N}{Z} exp\left(-\frac{mx^2}{2k_B T t^2}\right) dt \tag{3.10}$$

The equation 3.10 has the form of a Gaussian distribution. We can therefore obtain the size of the cloud S at a given time t and temperature T

$$S = \sqrt{\frac{k_B T}{m}} t. \tag{3.11}$$

So in the TOF experiment, we can let the cloud freely expand and take a picture of it at different times, t, and measure the corresponding cloud size. If the cloud has initial size, S_0, then the time evolution of the cloud size is just the sum of the squares

$$S(t) = \sqrt{\frac{k_B T}{m} t^2 + S_0^2}. \tag{3.12}$$

Then by estimating the derivative of the cloud size with respect to time in a given direction, we obtain the atomic velocity. This can then be rearranged algebraically to obtain the temperature of the cloud.

Chapter 4

BEC production and characterisation

This section is dedicated to the description and detailed characterisation of the various phases of the experimental sequence implemented to achieve a BEC: a composite scheme of pre-cooling, laser cooling, magnetic trapping and optical trapping is used in order to achieve the quantum degeneracy. Each stage has been optimised to reach the maximum PSD possible at the end of the routine. The most relevant experimental phases are described, with focus on how the optimal parameters have been selected.

4.1 Experimental sequence

The experimental routine performed in this experiment is structured as follows:

- Thermal ($\approx 35\ ^{\circ}C$) ^{87}Rb vapour is released in the loading chamber and then captured and pre-cooled in a MOT.

- A second MOT is created (containing $\sim 10^8$ atoms) in the science chamber by direct loading from the LVIS, with cooling beams intensities of 3.18 mW/cm^2 and a magnetic field gradient of 24 G/cm. After the MOT loading, a compression phase that lasts 12 ms increases the spatial density of the atoms which are subsequently further cooled by sub-Doppler mechanism.

- After these stages, the atoms are prepared for magnetic trapping. For this purpose, optical pumping is performed to pump all the atoms into the $|F = 2,\ m_F = +2\rangle$ ground-state for 0.2 ms. After the optical pumping, the magnetic

field gradient is increased to 225 G/cm.

- After 150 ms, the RF evaporation in the magnetic trap starts. The RF evaporation sequence is made by two different ramps plus a final holding time of 1 s, where the RF is kept constant. The dipole trap beams are switched-on during the RF evaporation.

- To complete the loading of the dipole trap, the quadrupole gradient is ramped down from 225 G/cm to 30 G/cm in 3 s. A 110 ms holding step follows the ramp and allows any atoms not transferred into the dipole trap to fall away.

- At this point, the optical evaporation takes place: an exponential ramp is used to decrease the power of the dipole trap beams. In our case the dipole ramp occurs over 6 s, taking the beam power from 5 W to 40 mW for the first beam and from 3.5 W to 28 mW for the second one.

- After this stage, the atoms experience a 110 ms of holding time. During this 110 ms the dipole trap is kept on, at its minimum power together with the magnetic field gradient, which is kept at the value that let the atoms levitate against gravity. In addition to the quadrupole magnetic field, a magnetic field offset is implemented during both the evaporation and the final holding time, to increase the evaporation efficiency. In this trap, quantum degeneracy is observed with 7.5×10^4 atoms. With further evaporation, pure condensates of around 5×10^4 atoms can be created.

Fig.4.1 shows a schematic of the steps leading to the ^{87}Rb BEC, where the all the technical details of each phase are summarised.

4.2 Cooling in the MOT chamber

The very first step towards a BEC is obtained via a Magneto-Optical Trap (MOT), which is implemented by using 3D laser cooling and a magnetic field gradient to confine the cooled atoms. Details of laser cooling are not reported in this work but the reader can find a comprehensive explanation in [4, 107]. Laser cooling requires

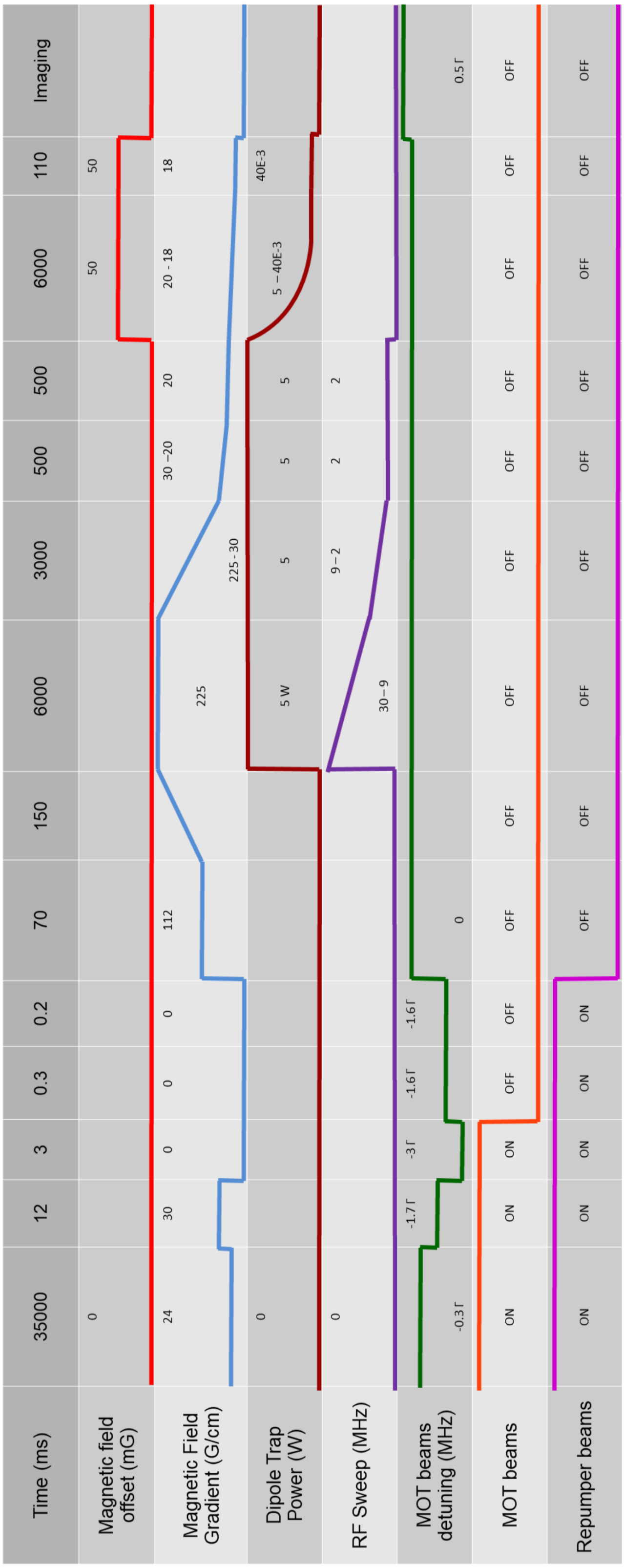

Figure 4.1: Experimental routine performed to achieve Bose-Einstein condensate in a hybrid trap.

the use of three pairs of mutually orthogonal and counterpropagating laser beams which must be red-detuned with respect to the cooling transition in order to create a viscous force in the region where they intersect. In our case, the MOT in the science chamber exploits a standard six beam configuration, where the atoms are accumulated in the overlapping region as a consequence of the loading from the LVIS beam. For 35 s the cooling and repumper laser beams are switched on, along with a low magnetic field gradient (24 G/cm) resulting in a MOT of 10^8 atoms with a temperature of 408 μK. The optimal cooling beams detuning and intensity, along with the magnetic field gradient value were experimentally optimised by maximising the loading rate of the MOT, which was $R = (19.5 \pm 0.3) \times 10^6$ s^{-1} at the end of the optimisation process. The corresponding MOT beam detuning was $\delta = -0.96\Gamma$ while an average MOT beam intensity of 3.18 mW/cm^2 was found to be ideal.

4.3 Compressed MOT

Once sufficient atoms have accumulated in the MOT, a 12 ms compressed MOT (CMOT) stage is performed. The CMOT stage is implemented by varying the detuning of the cooling light and the magnetic field gradient. Firstly proposed in 1994 [108], this technique allows to increase the density of the atomic sample by separating loading and compression phases. Atomic spatial density in the MOT depends on the number of trapped atoms in a volume which is proportional to the magnetic field gradient. The spatial density of a MOT cannot increase indefinitely because of limiting factors, such as the thermal motion of atoms, and mechanisms arising from the cooling process, like the re-emission of photons within the cloud (i.e. by atoms that undergo spontaneous emission) and the attenuation of the cooling laser through a dense atomic cloud. In detail, the limitation imposed by the re-emission of photons within the cloud, calculated in [108], is proportional to the magnetic field gradient and to the cross-section for a laser beam photon. Therefore a way to overcome limitations upon the spatial density is to increase the magnetic field gradient and the detuning of the laser cooling beams once the MOT is loaded. In this way, the spatial density is enhanced and the number of trapped atoms is not

compromised. The optimised parameters for the CMOT-phase in our experimental

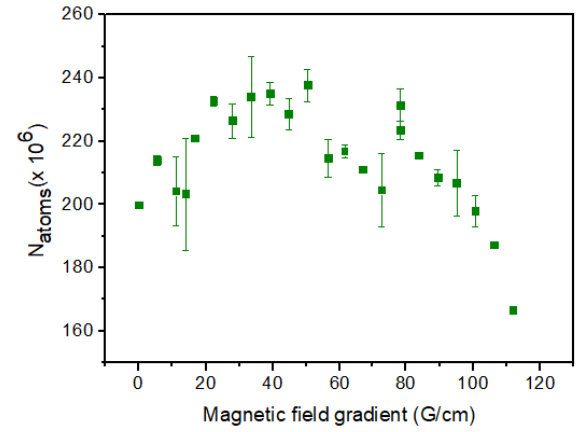

(a)

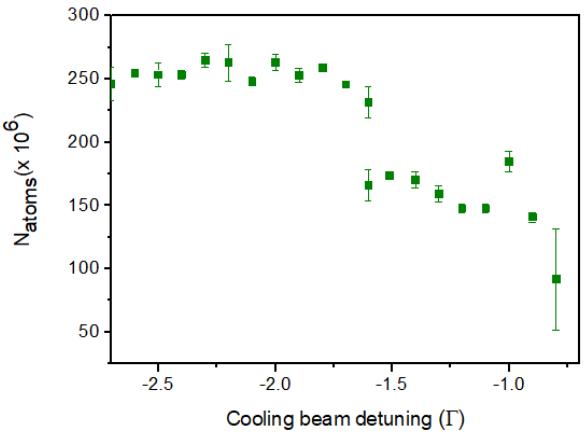

(b)

Figure 4.2: Magnetic field gradient and laser detuning optimisation during the CMOT-phase. The number of atoms trapped in the CMOT was measured when: a) The magnetic field gradient was varied with a constant laser detuning of the cooling beams (δ =-0.3 Γ). b) The detuning of the cooling beams was varied with a constant magnetic field gradient (30 G/cm). The number of atoms was measured after a 12 ms of CMOT-phase and the volume of the trap was assumed to be constant (i.e. higher the number of trapped atoms, higher the atomic spatial density in the CMOT).

sequence were chosen by measuring the number of atoms trapped in the CMOT when varying both the magnetic field gradient and the laser detuning, assuming the trapping volume constant. In particular, during the CMOT phase, the magnetic field gradient is 30 G/cm and the detuning of the cooling laser is -1.7Γ giving a final

atomic density of 1×10^{11} cm^{-3}, a factor 2.5 bigger than in the MOT phase. Figures 4.2 shows how these parameters were obtained. Firstly, the number of atoms was measured by varying the magnetic field gradient while keeping the laser detuning constant ($\delta = -0.3\Gamma$). Secondly, once the optimal value of the magnetic field gradient was observed, the number of atoms was measured by varying the laser detuning for the optimised value of the magnetic field.

4.4 Sub-Doppler cooling

After the CMOT-phase, the magnetic field gradient is switched off, leaving the atoms experiencing only the scattering force of the MOT beams. In this configuration, a cooling process arises (called sub-Doppler cooling) due to the interaction between the multilevel atomic structure and the light polarisation gradient, which originates from the interference between counterpropagating beams [4]. Sub-Doppler cooling is characterised by a large friction coefficient that is dependent on the laser intensity and on the laser detuning, through which ultra-low temperatures can be obtained (of the order of few μK) with a characteristic limit related to the recoil momentum, which is T_r =361.96 nK for ^{87}Rb. In our experimental setup the variation of the laser detuning during the sub-Doppler cooling phase has proven to be beneficial with respect to the final achieved temperature. To optimise the efficiency of this phase, a systematic measurement of the atoms captured in the magnetic traps was realised by varying the detuning of the MOT beams during the sub-Doppler cooling, as shown in Figure 4.3. The maximum number of trapped atoms was observed for a detuning of -3.5Γ. After 3 ms of sub-Doppler cooling, the atomic cloud is characterised by a temperature of T = (40$\pm$1)μK and a spatial density of 4×10^{10} atoms/cm^3. The low temperatures achievable with the sub-Doppler cooling technique allow, on one side an efficient magnetic trap loading by ensuring the adiabaticity of the process, on the other side the possibility to directly load the atoms into an optical trap. It is important to underline that during this phase, where the magnetic quadrupole is switched off, the atoms are even more sensitive to external magnetic fields. The optimisation of this phase is therefore also guaranteed by the

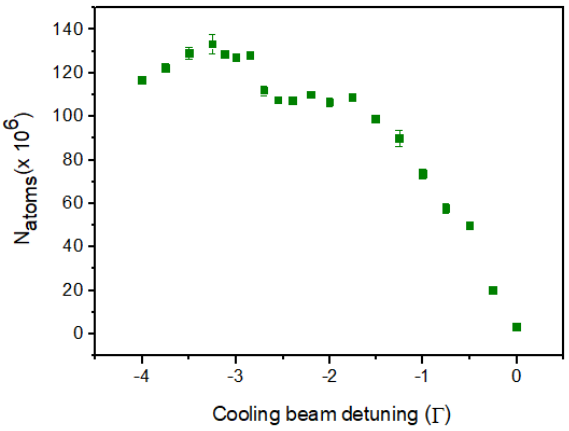

Figure 4.3: Sub-Doppler cooling optimisation: The number of atoms in the magnetic trap was measured for different values of detuning of cooling beams during the 3 ms of sub-Doppler cooling phase.

optimum setting of the compensation coils.

4.5 Optical pumping

For an efficient magnetic trapping, the atomic sample must be optically pumped into the low-field seeking $|F = 2; m_F = +2\rangle$ sub-level of the $5^2S_{1/2}$ ground state. In order to do so, a DC magnetic field (bias field) was applied, to lift the degeneracy of the Zeeman sub-levels, and a $\sigma+$ circularly polarised laser beam was used to drive optical transitions between $|F = 2\rangle$ and $|F' = 3\rangle$ states and accumulate the atoms in the desired sub-level (see section 5.1.1 for a more detailed description). In our setup, the beam used for optically pumping the atoms is the same used for the absorption imaging diagnostic. The beam propagates along the z-direction (-$\hat{z}$ in Figure 3.1) and the DC magnetic field is applied along the same direction. To generate the DC field a pair of dedicated Helmholtz coils was installed. It may seem counterintuitive but the DC field was actually generated when the Helmholtz coils were switched off due to limitations regarding the fast switching of the coils. An immediate switch-on of the DC field was not doable during the OP phase because its short duration (0.2 ms). To overcome this limitation an overcompensation of the background DC magnetic field along the $\hat{z}$-axis was achieved with the compensations coils, and then balanced out with the Helmholtz coils (during all the other phases). When optical

pumping is required the Helmholtz coils are switched off, and a uniform magnetic field along -$\hat{z}$ is generated.

The total duration of the optical pumping phase is 0.5 ms, during which the cooling and the repumper beams are off, along with the quadrupole field. In the first 0.3 ms the Helmholtz coils are switched off and the detuning of the beam is shifted to -1.8Γ, then for 0.2 ms the optical pumping beam is shone on the atoms while the Helmholtz coils are still off. After this phase, the Helmholtz coils are switched back on, to compensate the background field. The switching of the pump beam is governed by an AOM while for the coils a dedicated SSR switch (Crydom - DM0063) opens or closes the current flow depending on the level of the TTL signal delivered to it. Both the AOM and the switch are controlled via LabVIEW interface.

4.6 Loading the hybrid trap

4.6.1 Magnetic trapping

In our setup, the magnetic trap is realised with the same anti-Helmholtz coils that provide the MOT quadrupole field. These coils (described in section 3.1) create 3D confinement by producing a magnetic field which is position dependent. The value of the linear gradient along the $\hat{x}$ and $\hat{y}$ directions depends on the amount of current flowing through the coils and is set via LabVIEW interface.

After the atoms are optically pumped, the quadrupole trap is switched back on to produce a constant magnetic gradient of 112 G/cm for 70 ms, in order to spatially confine the atoms. The magnetic gradient is subsequently increased, via a linear ramp 150 ms long, to a maximum value of 225 G/cm to increase the atomic density and thus enhance the collisional rate for a more efficient evaporation. The magnetic gradient field is kept at its maximum value for 6 s, during which the optical trap is switched on and the first phase of forced evaporation is performed.

The magnetic potentials and the corresponding trapping frequencies used in our setup are represented in Figure 4.4, as a function of different values of the radial coordinate r= $\sqrt{x^2+y^2}$.

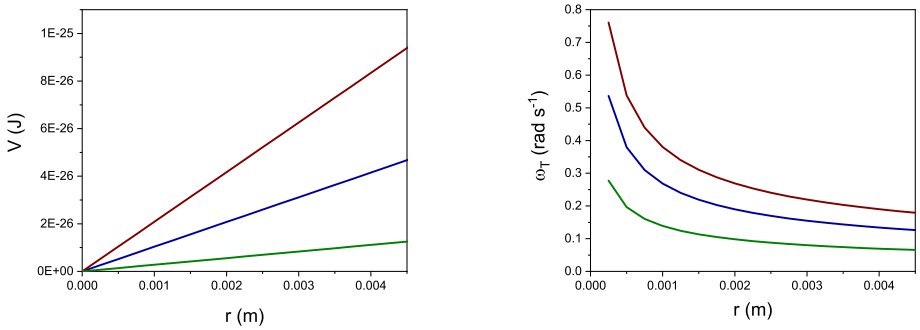

Figure 4.4: Model of the magnetic trap: a) Magnetic trap potential and b) Magnetic trap frequencies along the radial coordinate, where r represents the amplitude of the atomic orbit and r = 0 indicates the point in the middle of the two coils. Both the values have been computed for different values of the magnetic field gradient (green solid line : 18 G/cm, blue solid line : 112 G/cm, red solid line : 225 G/cm), which are the values used in our setup, in the specific configuration used to trap atoms.

4.6.2 Evaporative cooling in the magnetic trap

In the magnetic trap, evaporation is performed using a radio-frequency (RF) to selectively remove the hottest atoms. The most energetic atoms of the distribution tend to populate a larger area of the magnetic trap because of a larger thermal displacement, therefore by applying an RF resonant with only the most energetic Zeeman sub-levels these hot atoms can be removed.

The RF evaporation in our sequence is obtained by performing two subsequent linear ramps plus a final holding time of 1 s, where a RF of 2 MHz is kept constant. The first RF ramp goes from 30 MHz to 9 MHz in 6 s, with a constant magnetic field gradient of 225 G/cm, while the second one goes from 9 MHz to 2 MHz in 3 s, during which the magnetic field gradient is ramped down from 225 G/cm to 30 G/cm to complete the loading of the dipole trap. A 500 ms holding step follows the ramp, during which the magnetic field gradient is kept at 20 G/cm, and any atoms not transferred into the dipole trap are allowed to leave the trapping volume.

In order to realise an efficient routine, it was essential to identify the starting frequency of the RF sweep (i.e. when the RF signal begins to remove atoms from the distribution). This frequency was identified by applying a constant RF signal and

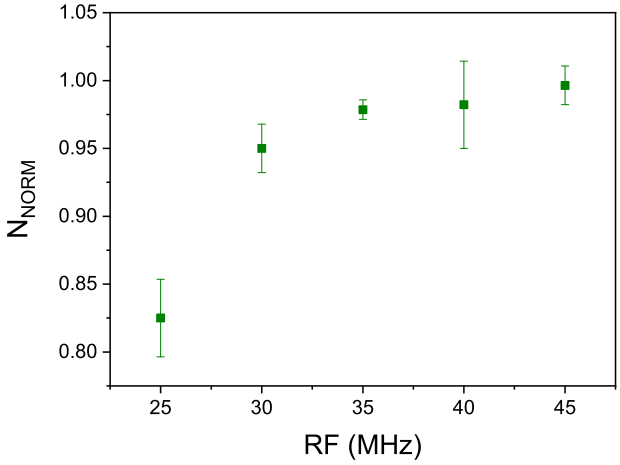

Figure 4.5: Optimisation of the starting frequency of the forced evaporation: the number of atoms is measured as a function of the starting RF value. The number of measured atoms was normalised with respect the number of atoms measured without evaporation. 30 MHz appears to be the frequency at which a sensible loss of population can be observed.

measuring the number of atoms trapped after a certain amount of time (6 s in our case). For our experimental routine, the total number of atoms trapped in the magnetic trap was visibly reduced when a frequency $\leq$30 MHz was applied, as shown in Figure 4.5. Hence imposing 30 MHz as the starting frequency for the first ramp. Each parameter of our RF sequence routine (start/end and duration of the ramps) was optimised by measuring the PSD of the atomic sample at the end of evaporative cooling by varying one single parameter and keeping all the other constant. An example of the optimisation process is reported in Figure 4.6: the PSD and the temperature of the atoms at the end of the evaporative cooling in the magnetic trap were measured while the duration of the first ramp and the second ramp were varied, respectively.

The truncation parameter η can be calculated by comparing the energy of the atoms in the trap $E_{atom} = m_F g_F \mu_B B = k_B T$ with the cutting energy $E_{cut} = m_F \hbar \omega_{RF} = k_B T_{cut}$ [109]. The ratio between the cutting temperature T_{cut} and the atomic temperature T (calculated via TOF technique) gives

$$\eta = \frac{T_{cut}}{T}. \tag{4.1}$$

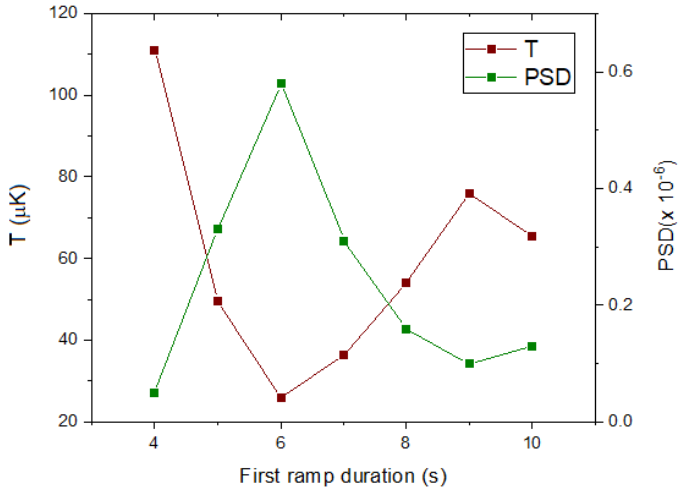

(a)

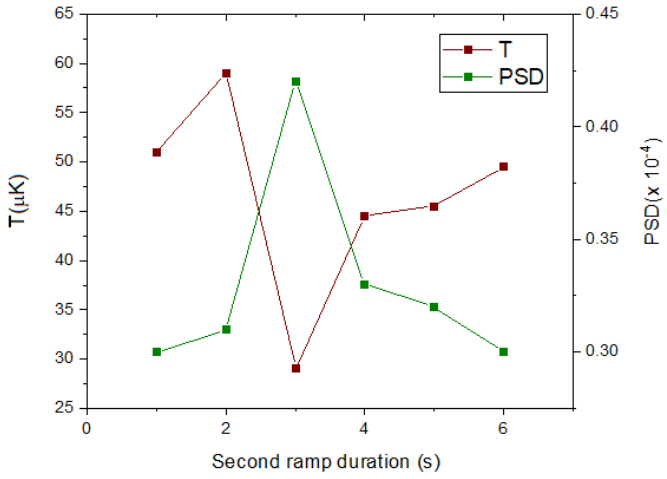

(b)

Figure 4.6: Optimisation of the RF ramps duration: a) The duration of the first ramp is optimised as a function of both the temperature and the PSD b) The duration of the second ramp is optimised as a function of both the temperature and the PSD. The temperature (dark red line) and the phase space density (green line) of the atomic cloud were measured at the end of the overall evaporation process. The optimisation of the two durations was done separately, by varying one parameter per measurement. The start/end of the sweeps were kept constant during this optimisation: the first ramp sweeps RF from 30 MHz to 9 MHz, while the second ramp sweeps radio-frequency from 9 MHz to 2 MHz. The temperature is an average between the temperatures calculated along the $\widehat{x}$-axis and $\widehat{y}$-axis.

At the end of the overall RF evaporation stage, the atomic sample contains 3×10^6 atoms at a T = 16 μK and a PSD = 1.2 $\times 10^{-5}$, with a corresponding $\eta = 12$.
In our experiment, the RF is delivered to the atoms by a coil fixed on the anti-Helmholtz coils base and the RF signal is generated by a Rhode & Schwartz SMT-02 signal generator, controlled via LabVIEW interfaces.

4.6.3 Optical trapping

In our setup, the optical crossed dipole trap is switched on when the magnetic field gradient reaches its maximum value, which corresponds to the starting time of the first RF ramp. The increment in spatial confinement given by a higher magnetic gradient enhances the loading of the optical trap, that lasts 10 s in total. To complete the loading phase, the quadrupole gradient is relaxed from 225 G/cm to 20 G/cm, at the end of the RF evaporation. The powers of the dipole trap beams during the loading phase are: 5 W for the first beam and 3.5 W for the second one, with a beam waist in the overlapping region of 80 μm and 110 μm, respectively. These correspond to maximum intensity in the trapping region of 1.99×10^5 W/cm^2 and 7.37×10^4 W/cm^2. The power loss in the second beam is due to the light scattered by the cell and by the optics necessary to retro-reflect the beam. This leads to an asymmetry of the trap frequencies, but it does not prevent an efficient evaporation.
Evaporation in the magnetic trap, along with an optimal alignment of the dipole trap beams with respect the quadrupole field zero, lead to an optical trapping of 5×10^6 atoms with PSD=10^{-5}. A typical absorption image of our dipole trap is shown in Figure 4.7. The absorption picture was taken during the alignment process and shows how the dipole trap looks after 30 ms of TOF, during which the dipole trap laser is kept at full power while the magnetic field gradient is switched off. In this way it is possible to observe only the atoms trapped in the optical trap and therefore evaluate the alignment. In addition, when the atoms freely expand along the dipole beams for 30 ms we can observe if the expansion is homogeneous or any interference between the beams is affecting the behaviour of the atoms.

Figure 4.7: An image, obtained via absorption imaging, of the dipole trap. The picture was taken after 30 ms of TOF, with the dipole trap laser on, at full power, and the magnetic field gradient completely switched off.

4.6.3.1 Dipole trap radial frequency measurement

Considering the fundamental role that the optical trap plays in our experiment, it is important to have full control of it. Therefore after having calculated the trap frequency with equation 2.12, we measured it, in order to accurately estimate the trap potential. The technique adopted for this measurement is the parametric excitation, where the trap frequency can be identified by modulating the dipole trap beams intensity. The modulation of the dipole beam intensity during the loading phase causes losses in the trapped atomic population due to parametric heating, when the frequency of the modulation matches the trap frequency. As a result, the trap frequencies can be identified as the modulation frequencies for which the number of atoms is minimum, as shown in Figure 4.8.

The modulation of the laser intensity is achieved by adding an oscillating amplitude modulation to the intensity stabilisation signal that controls the RF power sent to the AOM (see Figure 3.5). The sinusoidal output of a Keysight 33210A sig-

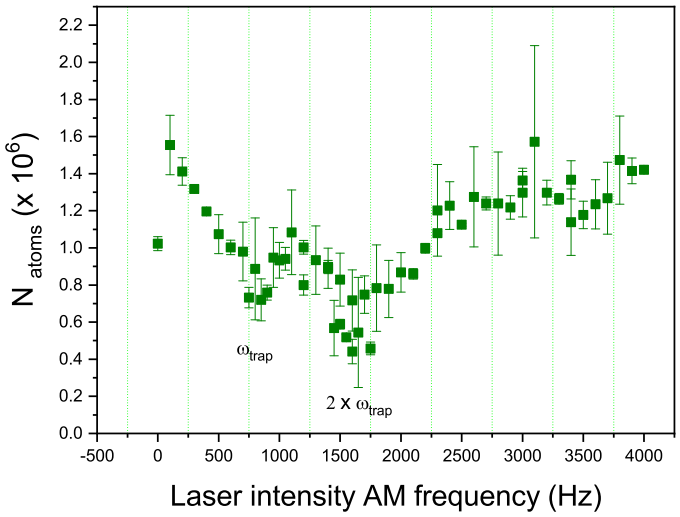

Figure 4.8: Measurement of the dipole trap radial frequency: the number of atoms in the optical trap is measured as a function of the laser intensity modulation frequency. The measured frequency was obtained by fitting the curve with a Lorentzian function in proximity to the minimum and it is in agreement with the predicted value of 870 Hz. Error bars in the measurements of the number of atoms represent the standard deviation of the averaged values plotted in the graph.

nal generator is summed to the output of the PID controller responsible for the intensity stabilisation (see Figure 3.5). The frequency of the function generator output is then systematically varied and the atomic population in the optical trap is measured for each value of the frequency. The intensity of the dipole beam is modulated for 50 ms, immediately after the dipole trap is loaded, with an amplitude corresponding to half of the laser intensity. In order to do so, the measurement was executed with a laser power 55% smaller than the maximum allowed by our setup, in order to have a sufficient power range to be modulated. Figure 3.5 shows the number of atoms as a function of the modulation frequency and allows to clearly identify the trap frequency ω_{trap} and its multiple $2 \times \omega_{trap}$. The possibility to observe both the radial trap frequency and its multiple is given by the two different modulations the beam is experiencing: the intensity modulation and, as a consequence, the beam-pointing modulation. These two modulations generate transitions of different nature, which depopulate the trap when the modulation frequency matches the trap frequency. In

this conditions, by using a power of 2.8 W, the frequency trap measured is consistent with the calculated value of 870 Hz.

4.6.3.2 Dipole trap lifetime

Another important parameter that characterises the dipole trap is its lifetime. An ultra-stable trap is fundamental in our process in order to minimise the atomic loss and the heating of the trapped particles. The number of atoms loaded in the optical trap was measured by keeping the dipole trap laser at full power and repeating the measurement for different duration of holding time, resulting in the optical density measurement shown in Figure 4.9. The curve was then fitted with an exponential de-

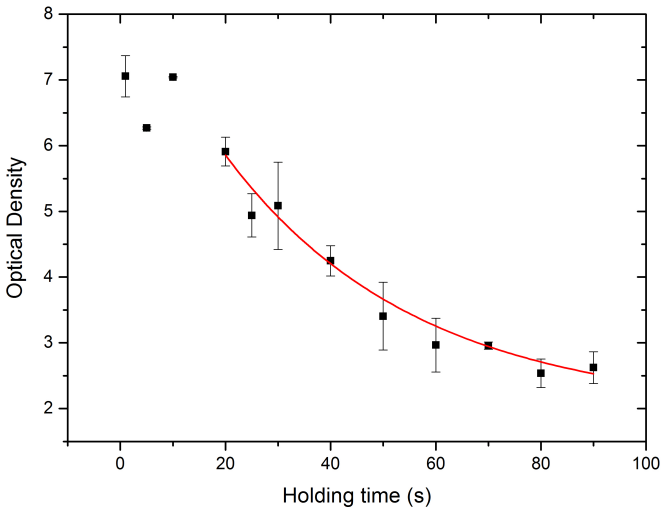

Figure 4.9: Dipole trap lifetime measurement: the optical density given by the atoms loaded in the optical trap is measured by keeping the dipole trap laser at full power and repeating the measurement for different duration of holding time. The curve is fitted (red solid line) with an exponential decay that gives a lifetime of 37 s. The first three points are not included in the fit because the number of atoms does not decrease in the first 10 s of loading.

cay, giving a lifetime of 37 s, that supports the efficiency of the stabilisation system implemented on the dipole trap (see Section 3.4). This measurement also confirms the presence of an excellent UHV in the system, which minimises collisions with particles in the background otherwise detrimental to the trap. From Figure 4.9 is possible to observe how the optical density, and therefore the number of atoms, re-

mains unaltered during the first 10 s of loading, indicating that loss mechanisms are negligible in the first 10 s of trapping. It is ideal indeed to load the dipole trap for an amount of time that doesn't exceed this threshold.

4.6.3.3 Dipole trap beams polarisation optimisation

A Half-Wave Plate (HWP) was positioned along the path of the second dipole trap beam (as shown in Figure 3.3) to vary the relative angle between the polarisations of the two dipole beams, in order to suppress interference phenomena occurring when the two polarisations are parallel. The spatial intensity inhomogeneities resulting from the interference are detrimental to the dipole trap loading. To find the optimal

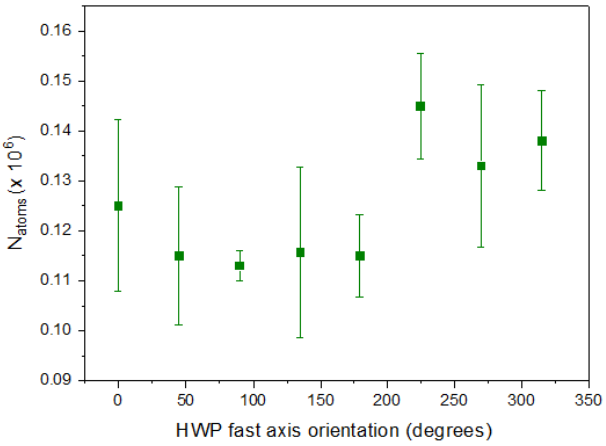

Figure 4.10: Optimisation of the dipole trap beams relative polarisation: the number of atoms trapped in the crossed dipole trap is measured as a function of different orientations of the HWP, that adjust the polarisation of the second dipole trap beam.

alignment of the fast-axis of the HWP, the number of atoms trapped in the crossed dipole trap was measured as a function of different orientations of the plate. The optimisation process is presented in Figure 4.10 and shows that, for a relative angle of 225 of the HWP fast axis, the number of atoms trapped in the optical trap is maximised.

4.6.4 Hybrid trap potential

When the optical crossed dipole trap is switched on and overlaps the magnetic field

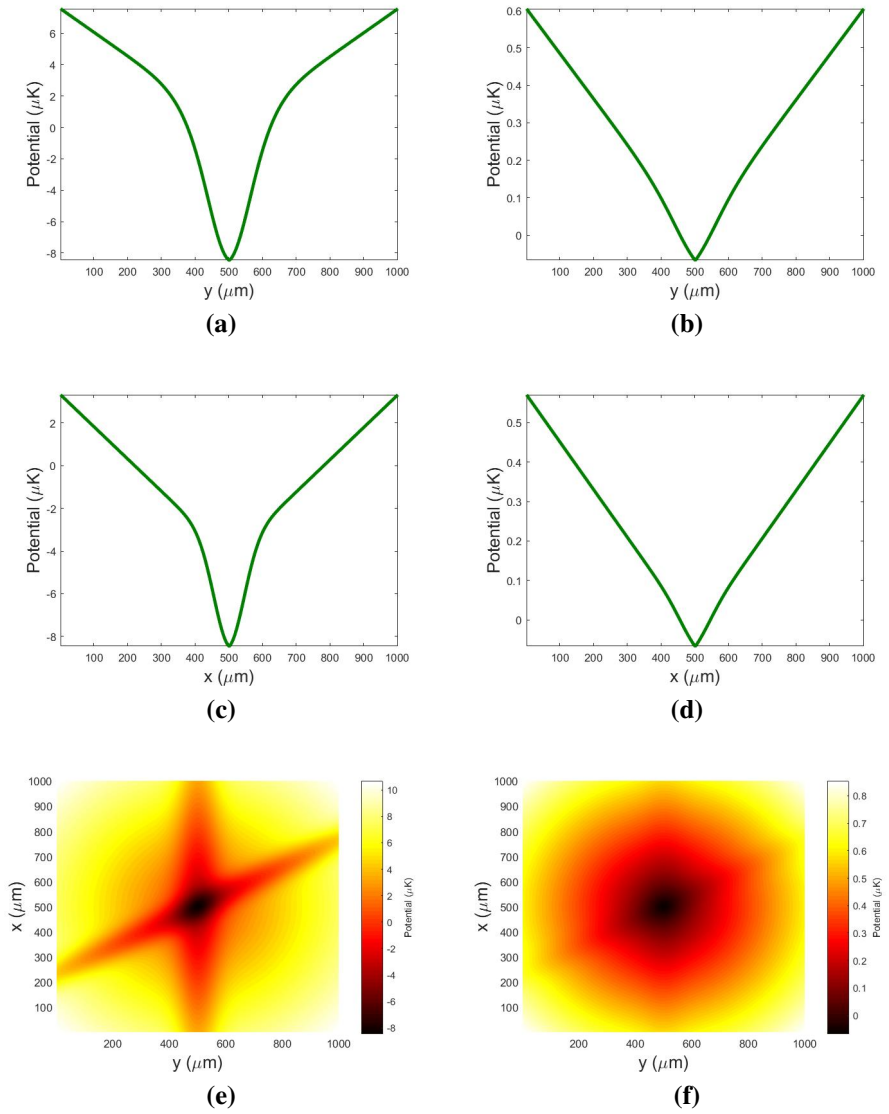

Figure 4.11: Hybrid trap potentials, given by a crossed dipole trap overlapped to a quadrupole trap, calculated at two different stages of our experimental routine. Figures on the left (a,c,e) show the potential when the optical trap intensities and the magnetic field gradient are maximum, 5W and 3.5W in the dipoles beams and 225 G/cm as magnetic gradient. Figures on the right (b,d,f) represent the potential when the optical trap intensities and the magnetic field gradient are minimum, 40mW and 28mW in the dipoles beams and 18 G/cm as magnetic gradient. Figures a) and b) represent the cross-section along $\widehat{y}$ axis, figures c) and d) are the cross-section along $\widehat{x}$ axis, while figures e) and f) compute the potentials in the x-y plane, in the two different stages.

gradient, the trapped atoms experience a hybrid potential, given by the equation 2.15. The actual potential felt by the atoms can be calculated by considering the parameter of our setup. Figure 4.11 shows the hybrid trap potentials at two different

stages of our experimental routine: when the dipole trap is loaded and when the dipole trap intensity and the magnetic gradient are both decreased. The mean trap frequency in the optical trap is 870 Hz during the loading phase and 90 Hz at the end of the optical evaporation, when the power is decreased. The potentials in Figure 4.11 are calculated by considering an angle between the two beams of 28 degrees.

4.7 Evaporation in the optical trap

In our experiment, evaporative cooling in the optical trap is performed by lowering the intensity of the trapping beams. This process reduces the trap depth, allowing the hottest atoms to escape. The average optical trap potential, initially $U_i = 40\ \mu$K, is decreased to U_{fin}= 200 nK in 6 s, as a result of a reduction in power from 5W to 40 mW for the first beam and from 3.5W to 28 mW for the second beam. To reach quantum degeneracy, the power is lowered via an exponential ramp, followed by 110 ms where the beams intensities are kept at a minimum power, to allow the re-thermalisation of the cloud. While the intensity of the optical trap is decreased, the magnetic gradient field is also linearly decreased from 20 G/cm to 18 G/cm. Even at very low gradients, the levitation provided by the gradient is still important in maximising the trap depth and providing a weak confinement along the arms of the laser beams.

The duration and the shape of the optical trap exponential ramp were optimised by evaluating its effect on the efficiency of the evaporation (i.e. by maximising the PSD reached at the end of the process). The exponential ramp controlled with LabVIEW interface is given by

$$V_{ext} = A_0 + A_1 e^{-R(t+t_0)} \tag{4.2}$$

and is then used to adjust the laser intensity via modulation of the RF-power used to drive the AOM. Specifically, V_{ext} is the setpoint generated by the software and sent to the PID to control the intensity of the beams, A_1 determines the steepness of the ramp while t is the duration. A_0 and t_0 are parameters automatically adjusted by the fit procedure to optimise the ramp shape, for a specific duration t and a certain initial and final power. As discussed in section 3.4 the laser intensity stabilisation

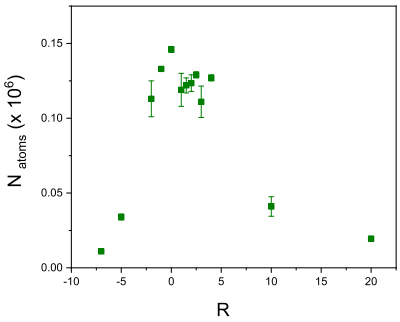

Figure 4.12: Dipole trap ramp optimisation process: Number of atoms after the optical evaporation as a function of the speed of the exponential ramp. Specifically, the speed of the ramp is adjusted via LabVIEW by changing the parameter R in Equation 4.2. On the x-axes are values of R tested during the optimisation. The duration of the ramp is 6s and bring the the beams from a maximum value of 5W and 3.5W to 40 mW and 28 mW, respectively.

circuit is composed by a chain of a logarithmic and a linear amplifier, therefore the actual dipole intensity response does not follow the exponential curve given by Equation 4.2. The optimisation of the exponential ramp was realised by varying the parameter R in Equation 4.2, as shown in Figure 4.12. The value of R chosen after the optimisation is 2, which corresponds to the dipole trap intensity ramp shown in Fig. 4.13. The shape of the ramp that maximises the number of atoms and the

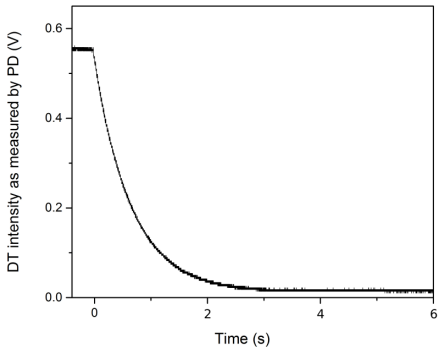

Figure 4.13: Dipole trap power ramp executed during the optical evaporation stage. The power profile was recorded via a photodiode (independent from the calibration process) by measuring the power of a fraction of the second beam. The power in the first beam is decreased from the maximum power of 5 W to 40 mW in 6 s.

optical density was as expected: steeper at the beginning of the evaporation, when

the trap frequency is higher and slower at the end, when the trap frequency is low and the thermalisation of the sample requires more time. After this stage the atoms experience 110 ms of holding time. During this 110 ms the optical trap is still on (at its minimum average power of 35 mW) as well as the magnetic field gradient, which is kept at the value that let the atoms levitate against gravity (18 G/cm). This final phase has proven to be fundamental to allow the thermalisation of the sample and the removal of the remaining background thermal atoms, thus not affecting the density measurements of the trapped atomic cloud. In addition to the quadrupole magnetic field, we use a magnetic field offset during both the evaporation and the final holding time to increase the evaporation efficiency. The temperature of the atoms cloud goes from 16 μK to 15 nK with the optical evaporation and a change of five orders of magnitude in PSD is obtained, resulting in PSD$\simeq$1 at the end of the ramp. The total number of atoms at the end of the optical evaporation process is 5×10^4.

4.7.1 Optimisation of the magnetic field offset

A DC magnetic field along the z-axis was applied during the optical evaporation phase to adjust the relative position of the centre of the quadrupole trap with respect to the dipole trap beams, as described in Section 3.5. By varying the relative dis-

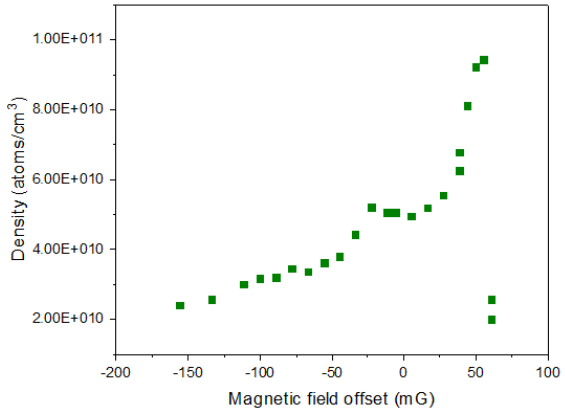

Figure 4.14: Optimisation of the DC magnetic field offset: the spatial density of the atomic cloud after the optical evaporation is measured as a function of the amplitude of the DC-field created along the z-axis during the optical evaporation.

placement between the traps, the spatial density of the sample can be increased by overlapping the denser regions of the two. A DC-field of 50 mG was found to maximise the density of the atomic sample obtained at the end of the optical evaporation, as shown in Figure 4.14.

4.8 BEC in a hybrid trap

Forced optical evaporation leads to an increase in PSD, given by a lower temperature of the atoms and a larger spatial density of the sample at the end of the process. Condensation is achieved at an average final dipole trap power of 35 mW after an optical evaporation of 6 s and a holding time of 110 ms, with a total number of atoms of about 10^5. The bimodal distribution (i.e. the transition from a Gaussian

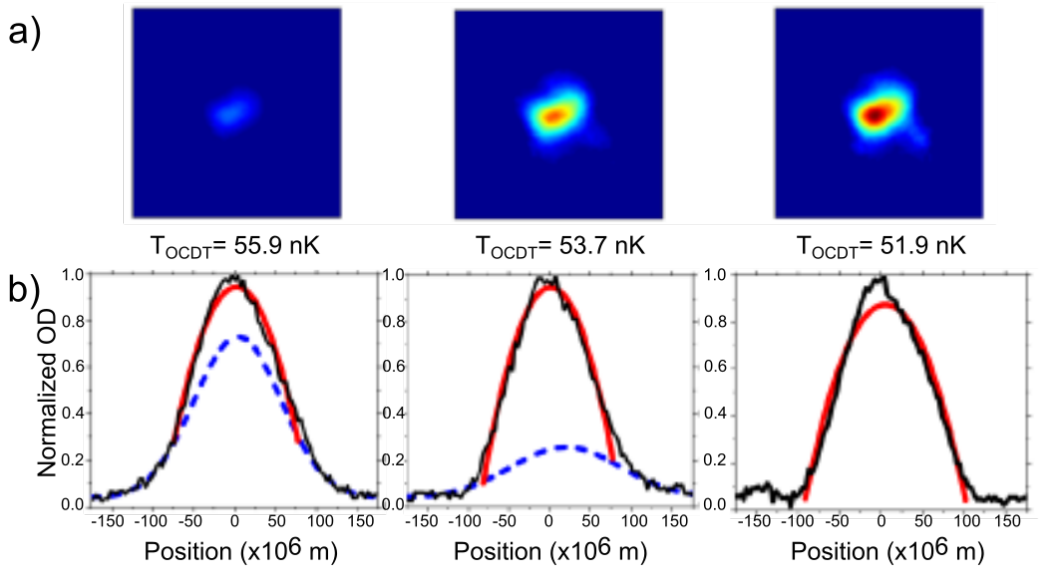

Figure 4.15: (a) Absorption images of the ^{87}Rb atomic sample at the end of the experimental routine, where different final values of optical trap depth were tested. The images were acquired after 20 ms of free expansion and they are represented in false colour scale. The final values of optical trap depth corresponding to the images are reported. The temperature of the pure BEC is T = 10 nK and is achieved after the sample re-thermalisation. (b) The corresponding density profiles of the absorption images are reported below each figure. A Gaussian fit (dashed blue line) and a parabolic fit (solid red line) represent the thermal and the condensate components of the atomic cloud, respectively. Image processing by Dr Marmugi [5]. Copyright (2016) by the American Institute of Physics.

distribution to an inverted parabola) arises when the trap potential is 60 nK and it's the fingerprint of the phase transition from a thermal distribution to a BEC. A pure condensate is obtained by further lowering the temperature of the atoms via re-thermalisation of the sample, resulting in 5×10^4 atoms with a temperature T≈10 nK and a PSD >1.

Figure 4.15 shows absorption images of the atomic sample after the forced optical evaporation process for different final trap depth values, along with their optical density profiles calculated in correspondence of the peak density. The absorption images are shown in a false colour scale and are normalised[1] to highlight the increasing condensed fraction. The parabolic distribution that reflects the harmonic potential and characterises the condensation phase is highlighted in Figure 4.15 (b) by a quadratic fit, while the thermal component is fitted by a Gaussian curve. It is

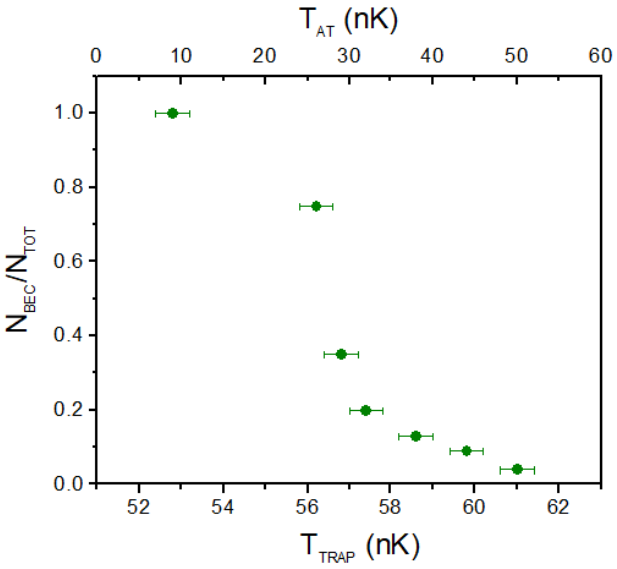

Figure 4.16: Fraction of condensed atoms in the atomic ensemble N_{BEC}/N_{TOT}, as a function of the optical trap final depth $T_{\mathrm{TRAP}} = U_{\mathrm{TRAP}}/k_B$. The corresponding temperature of the atoms T_{AT} is shown in the upper horizontal axis.

clear how the thermal component tends to disappear while the optical trap depth is lowered, resulting in an increase of the condensate fraction. In fact the BEC fraction N_{BEC}/N_{TOT}, which is the ratio between the number of condensed atoms and the total number of atoms in the cloud, increases while the dipole trap potential is

[1] The normalisation process is realised by imposing the maximum of the colour scale as the peak of the quadratic fit and the minimum of the colour scale as the maximum of the Gaussian fit.

lowered, as shown in Figure 4.16. The fraction of condensed atoms in the atomic cloud N_{BEC}/N_{TOT}, represented in Figure 4.16, is given by the ratio of the integral enclosed by the quadratic fit and the integral enclosed by the entire curve, given by the sum of the quadratic curve area and of the Gaussian curve area. Finally, Figure

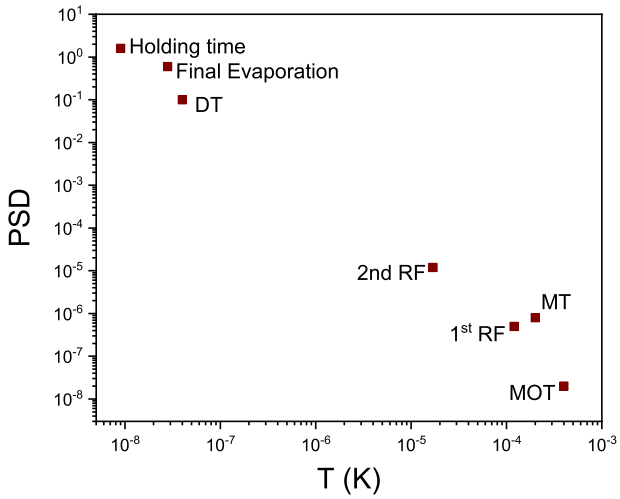

(a)

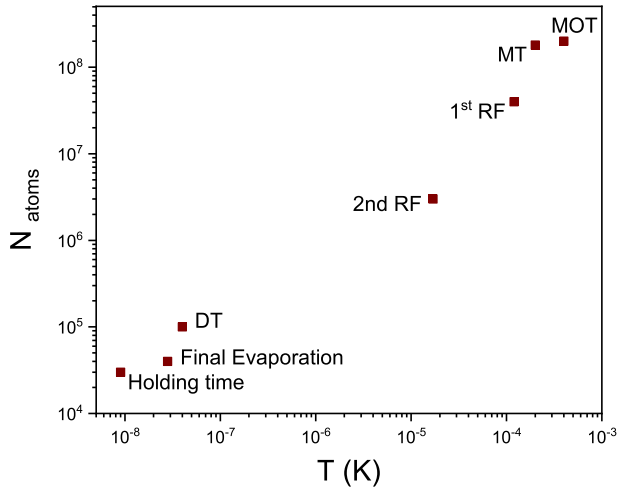

(b)

Figure 4.17: Values of PSD and number of trapped atoms shown as a function of the temperature in different stages of the experimental routine. The highest temperature corresponds to the MOT phase, the lowest one corresponds to the end of the optical evaporation, where the BEC is observed.

4.17 shows how the phase-space density of an atomic cloud is increased by eight

orders of magnitude after the magneto-optical trapping phase in order to produce a Bose-Einstein condensate, along with the drastic reduction in the number of trapped atoms that comes from this process. From a typical value of PSD in the MOT of 10^{-8} (number of atoms $\approx$ 300 million with a temperature T$\approx$ $400\mu K$), values of PSD $>$1 are achieved after the optical evaporation, where the atomic temperature is T$\approx$10 nK and the atoms in the BEC are 5×10^4. In each step that leads to the condensation, the spatial density is increased and the temperature of the sample decreased. This implies an increase in PSD, which is represented in Figure 4.17, when the entire sequence in Figure 4.1 is performed. By further lowering the optical potential at the end of the evaporation phase, higher values of PSD can be observed (PSD$>$5) but the high optical density of the cloud in these conditions reduces the accuracy of the diagnostic system and makes the measurements unreliable. Furthermore, a decrease of the final setpoint leads to a further reduction in the number of condensed atoms. Therefore these measurements might not be trustworthy and are not presented here.

The experimental sequence described in this chapter reliably produces a pure condensate of 5×10^4 ^{87}Rb atoms with final average temperature T$\cong$10 nK, every 50 s.

Chapter 5

Atomic magnetometry

In this chapter, the theory underpinning an Optical Atomic Magnetometer (OAM) is introduced, along with the description of the experimental setup built to obtain an RF-OAM with cold ^{87}Rb atoms. Firstly, a general overview of the principles of an OAM is provided: the method for polarising alkali atoms and detecting their spin orientation is discussed and the response of an atomic sample interacting with magnetic fields is reported. Secondly, the main differences between a cold atoms magnetometer and an OAM with particles at room temperature are considered, along with the main factors that limit the sensitivity of these devices. Finally, a detailed description of the RF-OAM experimental apparatus is presented along with the methodology developed for obtaining measurements and the preliminary results collected. This work was realised collectively with Dr Luca Marmugi, Krishna Jadeja, Yuval Cohen, and with assistance from Cameron Deans.

5.1 An Introduction to Optical Atomic Magnetometry

The fundamental idea of OAMs is to measure the response of an atomic vapour exposed to an external magnetic field. The response of the atomic angular momentum, as determined by the orientation of the unpaired electron's spin in alkali atoms, to magnetic fields and the light-matter interaction are the mechanisms exploited for operating an OAM. A schematic of a basic RF-OAM is presented in Figure 5.1. Firstly the atoms are exposed to a DC magnetic field $\mathbf{B_0}$ (bias field) and

optically pumped, therefore oriented in the atomic ground state, by using resonant polarised laser light. When the atomic spins are aligned, if a secondary magnetic field **B** is added, the atoms will undergo a Larmor spin precession with an angular frequency ω known as the Larmor frequency, which is proportional to the total field $\mathbf{B_{tot}} = \mathbf{B_0} + \mathbf{B}$ strength

$$\omega = \gamma |\mathbf{B_{tot}}|, \tag{5.1}$$

where γ is the gyromagnetic ratio. γ is a fundamental constant proportional to the particle charge and rest mass, therefore a measurement of the Larmor frequency gives a direct estimation of the magnetic field amplitude. The atomic spin precession modifies the absorptive and dispersive properties of the atoms which, through interaction with a light source, can be studied to extract information about the Larmor frequency.

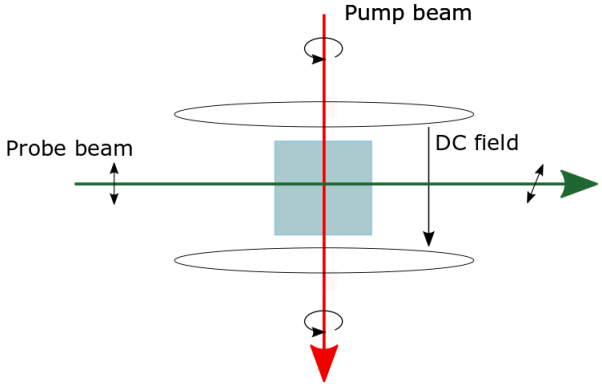

Figure 5.1: Scheme of a basic RF-OAM. The atoms are optically pumped along the direction of the DC magnetic field with the circularly polarised pump laser beam (red solid line) that propagates parallel to the field. The probe beam (green solid line), which is linearly polarised, monitors the atomic response to the magnetic field by detecting the atomic precession about the DC magnetic field. A characterisation of the magnetic field is obtained by analysing the atomic precession.

Alkali atoms are particularly sensitive to magnetic fields because of the strong interaction between the dipole magnetic moment of the unpaired electron and external magnetic fields. This feature makes these atoms an ideal medium for atomic magnetometry, where this property is exploited. The overall energy of the atom can be estimated by only considering the single electron and the nucleus, disregarding

the paired electrons in the inner energy shells. The same reasoning applies to the atomic spin, which is given by the vectorial sum of the nuclear spin and the unpaired electron spin, and allows us to easily represent the interaction between the magnetic dipole moment and external magnetic fields.

5.1.1 Optical Pumping

In order to obtain an efficient OAM, the atomic sample needs to be suitably prepared, this means the atoms need to be in the same state with their spin coherently oriented. The technique used to arrange the atomic ensemble in a spin-polarised state is optical pumping [63], which controls the population in the atomic levels via the exchange of angular momentum from resonant light. For the types of magnetometer presented in this manuscript, the degree of polarisation of the atomic sample is a fundamental parameter because it strongly affects the quality of the signal detected.

The optical pumping technique adopted in this work uses circularly polarised light, that propagates along the direction of a DC magnetic field, to accumulate all the atoms in one of the Zeeman sub-levels of the ground state by depopulating all the other states. There are two elements necessary for having an efficient optical pumping: a DC magnetic field, that dictates the quantisation axis for the atomic system and lifts the degeneracy of the magnetic states, and a polarised pump beam, resonant with the optical transition we want to exploit.

In this work, the pump laser beam of circularly polarised ($\sigma+$) light is resonant to the $|F=2;m_F\rangle \longrightarrow |F'=3;m_F\rangle$ hyperfine transition of the ^{87}Rb D2 line, as schematically represented in Figure 5.2, where the magnetic sub-levels of the hyperfine transitions are indicated. All the photons in the pump beam have the same spin projection along the direction of the beam's propagation equal to +1, in units of $\hbar$, if the light is $\sigma+$ polarised. The total angular momentum of the system 'atom + photons' must be conserved during light/atom interactions, therefore the optical transitions the atoms are allowed to undergo are characterised by $\Delta m_F = +1$. A transition, between the ground state sub-level $|F=2;m_F\rangle$ to the corresponding excited state sub-level $|F'=3;m'_F+1\rangle$, occurs when a photon is absorbed due to

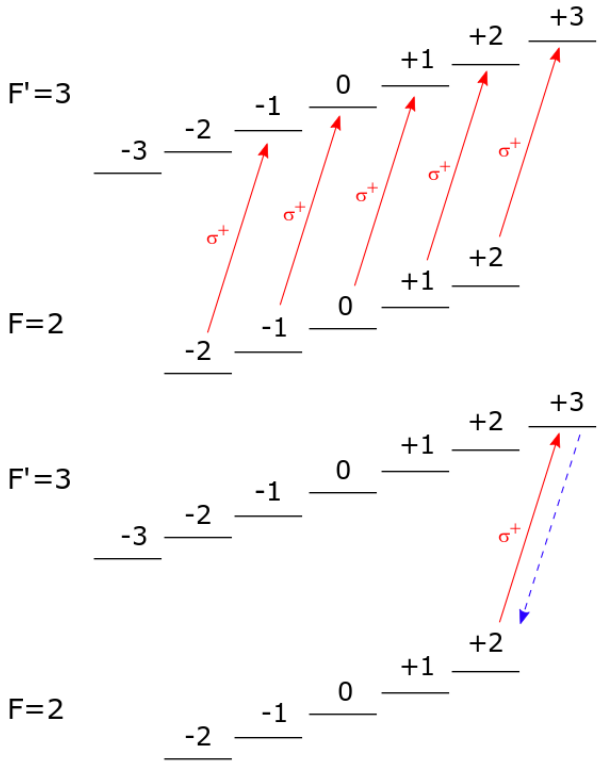

Figure 5.2: Optical pumping of the total atomic spin for optical hyperfine transitions of ^{87}Rb. a) The mechanism of optical pumping with $\sigma+$ polarised light is represented for the D2 line of ^{87}Rb, with focus on the $|F=2\rangle \longrightarrow |F'=3\rangle$ transition, which is the transition exploited in our experiment. The angular momentum carried by the photons is transmitted to the atoms during the absorption process, resulting in a transition with $\Delta m_F = +1$ (red arrows). The atoms can spontaneously decay in any possible state allowed by the transitions rules ($\Delta F = 0, \pm 1, \Delta m_F = 0, \pm 1$) with known probabilities. For this specific case the atoms in $|F'=3\rangle$ can only decay in states with $\Delta F = -1, \Delta m_F = 0, \pm 1$. The spontaneous emissions are not represented for clarity. b) Optical pumping with $\sigma+$ light causes a migration of the atoms towards the state $|F=2; m_F = +2\rangle$, where they will be forced to stay because of the cycling transition $|F=2; m_F = +2\rangle \longrightarrow |F'=3; m_F = +3\rangle$. The blue dashed line represents the spontaneous emission from the excited level $|F'=2; m_F = +3\rangle$.

transfer of angular momentum to the atom. Afterwards, the atom decays, with probabilities given by the branching ratios, into one of the allowed ground state levels for spontaneous emission of a polarised photon. After repeated absorption and emission cycles, the atomic population will be transferred to the state with the largest projection of angular momentum along the quantisation axis, which in our case is $|F=2; m_F = 2\rangle$. An atom in the $|F=2; m_F = 2\rangle$ state will remain in that level

as a consequence of the closed cycling transition with the $|F' = 3; m'_F = 3\rangle$ level. Through this process a macroscopic magnetisation of the atomic vapour is obtained, making it sensitive to external magnetic fields.

5.1.2 Detection: Measuring spin polarisation

In order to detect a magnetic field, it is necessary to observe the atomic spin precession that is generated by the field itself. The magnetometry technique adopted in this thesis uses the optical rotation of a linearly polarised probe beam for analysing the spin polarisation and detecting the Larmor precession.

The linearly polarised light of the probe beam can be decomposed into two circularly polarised components of opposite helicity, $\sigma+$ and $\sigma-$. If the probe beam is travelling through a circularly birefringent material, the difference in the index of refraction for the two states of circularly polarised light, leads to a rotation of the plane of polarisation of the probe beam by an angle θ. This effect is known as Faraday rotation or as circular dichroism. By analysing the rotation in polarisation of the probe beam after travelling through the atomic sample, it is possible to evaluate the absorptive and dispersive properties of the medium which depend on the projection of the atomic spin along the probe direction. For alkali atoms, the electron spin and the nuclear spin are coupled, and so it is the resultant total atomic spin. As a consequence, the information on the orientation of the electron spin that we can extract from the rotation in polarisation of the probe beam results in information on the total atomic spin orientation.

Recalling the semi-classical analysis seen in [110], we briefly show how the plane of polarisation is rotated in materials that are circularly birefringent. We consider the electric field vector for linearly polarised light in the y-direction which is travelling along the x-direction. At $x = 0$ the vector can be written as

$$\mathbf{E}(0) = \frac{E_0}{2} e^{i\omega t} \mathbf{y} + c.c., \tag{5.2}$$

where $c.c.$ indicates the complex conjugate. It is convenient to rewrite the electric field vector in a circular basis, where we can represent it as the vectorial sum of two

circularly polarised light with opposite helicity

$$\mathbf{E}(0) = \frac{E_0}{4} e^{i\omega t}(\mathbf{y} + i\mathbf{z}) + \frac{E_0}{4} e^{i\omega t}(\mathbf{y} - i\mathbf{z}) + c.c.. \tag{5.3}$$

After travelling a distance l in a circularly birefringent medium, where the index of refraction for positive and negative helicity light are different, n_+ and n_- respectively, the electric field vector has the form

$$\mathbf{E}(l) = \frac{E_0}{4} e^{i\omega n_+(\nu) l/c}(\mathbf{y} + i\mathbf{z}) + \frac{E_0}{4} e^{i\omega n_-(\nu) l/c}(\mathbf{y} - i\mathbf{z}) + c.c., \tag{5.4}$$

that can be written as

$$\mathbf{E}(l) = \frac{E_0}{4} e^{i\omega \bar{n}(\nu) l/c} e^{i\omega \Delta n(\nu) l/c}(\mathbf{y} + i\mathbf{z}) + \frac{E_0}{4} e^{i\omega \bar{n}(\nu) l/c} e^{-i\omega \Delta n(\nu) l/c}(\mathbf{y} - i\mathbf{z}) + c.c., \tag{5.5}$$

if we define $\bar{n}$ and Δn respectively in the following way $\bar{n}(\nu) = (n_+(\nu) + n_-(\nu))/2$ and $\Delta n(\nu) = (n_+(\nu) - n_-(\nu))/2$. Defining the rotation angle as

$$\theta = \frac{\pi \nu l}{c} Re\left(\frac{n_+(\nu) - n_-(\nu)}{2}\right) \tag{5.6}$$

and by ignoring the phase factor $e^{i\omega \bar{n}(\nu) l/c}$ which is common for both factors of (5.5) we can write (5.5) as

$$\mathbf{E}(l) = E_0(cos\theta \mathbf{y} - sin\theta \mathbf{z}), \tag{5.7}$$

which shows that the polarisation plane of the linearly polarised light has been rotated by an angle θ, that is nonzero if $n_+(\nu) \neq n_-(\nu)$.

The absorptivity and the refractivity of an atomic sample are proportional to its density. Only the atoms in the sub-levels that can interact with the light (i.e. that can absorb one unit of angular momentum) will contribute to the OAM signal. Therefore absorption coefficients for $\sigma+$ and $\sigma-$ light, and the respective indices of refraction $n+$ and $n-$ are strictly dependent upon the distribution of population in the ground state and the branching ratios of the optical transitions. The two circular polarisations experience a difference in absorptivity as a consequence of the

atomic polarisation created by optical pumping. The size of the effect is directly proportional to the distribution of atoms between the sub-levels and so proportional to the degree of polarisation of the atomic sample.

For the RF-OAM system presented in this thesis the rotation angle defined in equation (5.6) can be written as [34],

$$\theta = -\frac{\pi}{2} l n r_e c f_{D2} P_x D(\nu), \tag{5.8}$$

where r_e is the classical electron radius, n is the atomic vapour density, l is the the distance travelled by the probe within the medium, P_x is the atomic polarisation component along the direction of the probe beam propagation, f_{D2} is the oscillator strength of the D2 transition, which we assume to be equal to $2/3$ and $D(\nu)$ is the dispersive optical profile for the D2 transition, which depends on the relative strengths of the individual D2 hyperfine transition as a function of the atomic polarisation along the probe beam direction, the probe beam polarisation and detuning from the the resonance frequency of the hyperfine transition.

5.1.3 Radio-frequency OAMs

The realisation of an RF-OAM requires the presence of an external RF magnetic field in addition to the elements introduced in sections 5.1.1 and 5.1.2. The overall operation of the RF-OAM relies on two different transitions in the atomic sample.

The first ones are optical transitions, and are involved in the optical pumping and in the spin detection phases, which take place through transitions between different hyperfine levels of the ground and excited states of the alkali atoms. For these optical transitions the values of ΔF, which is the change of total angular momentum of the atom, can only be $0,\pm 1$.

The second type of transitions is generated by the introduction of an RF external magnetic field, according to the process discussed here. When interacting with a static external magnetic field $\mathbf{B_0}$, the degeneracy of the atomic magnetic sublevels m_F, which are the projections of the atomic angular momentum along the quantisation axis given by $\mathbf{B_0}$, is lifted. The difference in energy between those sub-

levels is proportional to the strength of the external magnetic field and is given by $\Delta E = g_F \mu_B m_F |\mathbf{B_0}|$ where g_F is the Landé g-factor and μ_B is the Bohr magneton. The external magnetic field $\mathbf{B_0}$, therefore, defines the energy shifts of the sub-levels

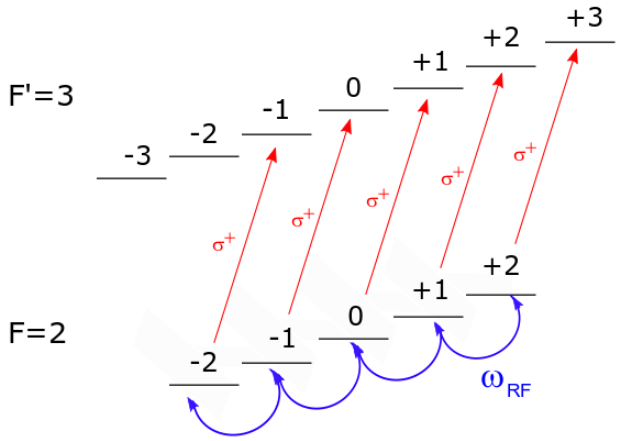

Figure 5.3: Schematic representation of the transitions involved in an RF-OAM operation. The ^{87}Rb $|F = 2\rangle \longrightarrow |F' = 3\rangle$ D2 optical transitions (red solid arrows) are a consequence of the optical pumping process. The transitions between different magnetic sub-levels within the ground state $|F = 2\rangle$ with $\Delta m_F = \pm 1$ (blue solid arrows) occur when an oscillating RF magnetic field $\mathbf{B_{RF}}$ is applied, whose radio frequency matches the Larmor frequency ω_0 of the Zeeman transitions.

and the corresponding Larmor frequency of the transitions between them, following the relation:

$$\omega_0 = \frac{\Delta E}{\hbar} = \gamma |\mathbf{B_0}|. \tag{5.9}$$

If an oscillating RF magnetic field $\mathbf{B_{RF}}$ is applied, whose frequency ω matches the Zeeman splitting, such that $\Delta E = \hbar\omega_0$, transitions between different magnetic sub-levels within the hyperfine structure are induced (same principle of the RF evaporative cooling seen in Section 2.2.1). This produces coherently driven Larmor precession at frequency ω_0. This can be considered, from the point of view of $\mathbf{B_{RF}}$ field, as a resonant process obtained when $\omega = \omega_0$. For these transitions, the variation ΔF of the total angular momentum will be zero, while the magnetic states will be coupled by $\Delta m_F = \pm 1$. These transitions constitute the second type of transitions necessary for operating an RF-OAM and are shown in Figure 5.3 by the solid

blue line. When $\mathbf{B_{RF}}$ is applied, the population of the magnetic Zeeman sub-levels is coherently driven within the ground states of the atomic structure. An oscillating transverse spin polarisation component is thus generated by these transitions and is then sensed by the probe beam, whose polarisation is oscillating at a frequency equals to the Larmor frequency ω_0. A schematic of this process is presented in Figure 5.4.

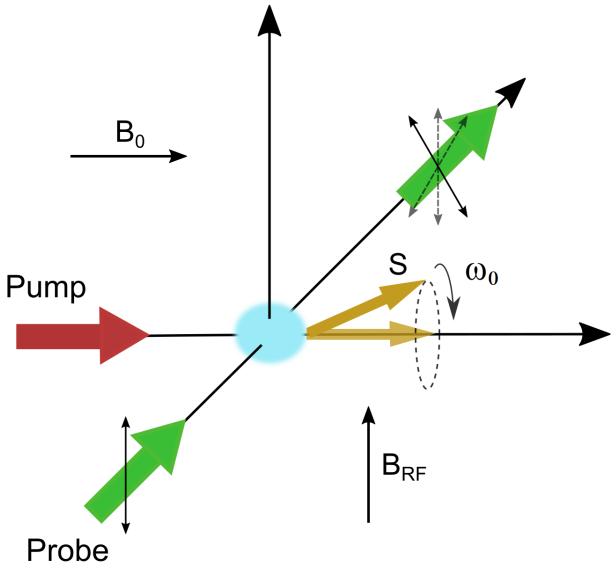

Figure 5.4: Schematic of the operation of an RF-OAM: Once atoms are optically pumped, a resonant RF magnetic field $\mathbf{B_{RF}}$ induces a transverse spin component that generates the coherent precession of the spin $\mathbf{S}$ at the Larmor frequency ω_0, imposed by the DC magnetic field $\mathbf{B_0}$, which results in the rotation of the polarisation of the probe beam.

5.1.4 Magnetometer Response

The measurement of the optical properties of an ensemble of atoms when a magnetic field is applied is the basis of OAM. Therefore showing how the macroscopic magnetisation of a spin ensemble evolves upon application of a magnetic field can be useful to understand the nature of the interaction and the limitations of this measurement technique. The interaction between atomic systems and magnetic fields is fully described by the evolution of the density matrix, which gives a statistical aver-

age of the total atomic spin by representing the dynamic of an ensemble of atomic spins. Another method was proposed by Bloch [111], who represented the spin evolution of an atomic ensemble via phenomenological equations, and it's adopted in this work to describe the atomic response of a RF-OAM. For a detailed description of the density matrix approach, the reader can consult [112].

Since the orientation of the electron spin indicates the orientation of the total atomic spin, the description of the interaction considers the total atomic spin $\mathbf{S} = \{S_x, S_y, S_z\}$. The evolution of the atomic spin $\mathbf{S}$ in an external magnetic field $\mathbf{B}$ is described by the Bloch equation [111],

$$\frac{d\mathbf{S}}{dt} = \gamma\mathbf{S} \times \mathbf{B} - \frac{S_x\mathbf{x} + S_y\mathbf{y}}{T_2} - \frac{S_z - S_0}{T_1}\mathbf{z} \tag{5.10}$$

where $\mathbf{x}, \mathbf{y}, \mathbf{z}$ are the unit vectors in the laboratory frame and $\gamma = \gamma_e/(2I+1)$ is the gyromagnetic ratio of the total atomic spin. Supposing a DC magnetic field is applied along the z-direction, S_z is the longitudinal spin polarisation, while the vectorial sum of S_x and S_y gives the transverse spin polarisation. The terms on the right-hand side of Equation 5.10 represent, respectively, the precession of the atomic spin about the external magnetic field $\mathbf{B}$, the depolarisation effect on the transverse component of the spin at a rate given by the transverse relaxation time, T_2, and the effect, due to optical pumping to polarise the spins along the z-direction. S_0 is the steady state longitudinal polarisation, reached when no magnetic fields are applied, and it is proportional to the optical pumping rate and to the longitudinal relaxation time T_1.

In detail, the external magnetic field $\mathbf{B}$ experienced by the atomic sample is given by the sum of the DC magnetic field $\mathbf{B_0}$ and the oscillating $\mathbf{B_{RF}}$, when an RF OAM is operated. The static magnetic field is given by

$$\mathbf{B_0} = \frac{\omega_0}{\gamma}\mathbf{z}, \tag{5.11}$$

which is the field that lifts the degeneracy of the magnetic sub-levels along the z-direction and coupled them by the Zeeman transition frequency ω_0. The oscil-

lating magnetic field $\mathbf{B_{RF}} = B_{RF}cos(\omega t)\mathbf{y}$ is applied along the y-direction and can be decomposed into two circularly polarised components that rotate in opposite direction with frequencies, respectively $\pm\omega$ and amplitude $B_{RF}/2$. In order to derive steady-state solutions for the Bloch equation it is useful to re-write the effective field experienced by the atoms and the equation 5.10 itself in the reference frame that is coherently rotating with the spins. In this new reference frame the co-rotating component of the oscillating field $+\omega$ is static[1] and the x-y plane in the laboratory frame is rotating around $\mathbf{B_0}$ at a frequency ω, which is the RF field oscillation frequency. The total effective field felt by the atomic spin in the rotating frame is

$$\widetilde{\mathbf{B}} = \left(B_0 - \frac{\omega}{\gamma}\right)\widehat{\mathbf{z}} + \frac{B_{RF}}{2}\widehat{\mathbf{y}} = \frac{(\omega_0 - \omega)}{\gamma}\widehat{\mathbf{z}} + \frac{B_{RF}}{2}\widehat{\mathbf{y}} \tag{5.12}$$

and the corresponding Bloch equation is

$$\frac{d}{dt}\widetilde{\mathbf{S}} = \gamma\widetilde{\mathbf{B}} \times \widetilde{\mathbf{S}} - \frac{\widetilde{S}_x\widehat{\mathbf{x}} + \widetilde{S}_y\widehat{\mathbf{y}}}{T_2} - \frac{(S_z - S_0)\widehat{\mathbf{z}}}{T_1}, \tag{5.13}$$

where S_0 is the atomic spin polarisation in equilibrium when the oscillating magnetic field is no longer present and $\widehat{\mathbf{x}}, \widehat{\mathbf{y}}, \widehat{\mathbf{z}} = \mathbf{z}$ are the unit vectors in the rotating frame. By imposing $\frac{d}{dt}\widetilde{\mathbf{S}} = 0$ is possible to find the steady solution of the Bloch equation in the rotating frame for the spin components

$$\begin{aligned}
\widetilde{S}_x &= \frac{\gamma(B_{RF}/2)T_2}{1 + \gamma^2(B_{RF}/2)^2 T_1 T_2 + \Delta\omega^2 T_2^2} S_0 \\
\widetilde{S}_y &= \frac{-\gamma(B_{RF}/2)\Delta\omega T_2^2}{1 + \gamma^2(B_{RF}/2)^2 T_1 T_2 + \Delta\omega^2 T_2^2} S_0 \\
\widetilde{S}_z &= \frac{1 + \Delta\omega^2 T_2^2}{1 + \gamma^2(B_{RF}/2)^2 T_1 T_2 + \Delta\omega^2 T_2^2} S_0,
\end{aligned} \tag{5.14}$$

where $\Delta\omega = \omega - \omega_0$. Performing the inverse transformation, from the rotating frame

[1] The counter-rotating component $-\omega$ can be neglected if the magnetic linewidth $\Gamma = \frac{1}{T_2}\sqrt{1 + \gamma^2(B_{RF}/2)^2 T_1 T_2}$ is much smaller than the Larmor frequency because its contribution becomes insignificant at frequencies near $+\omega_0$.

to the laboratory frame, the spin component can be written in the form

$$\begin{aligned} S_x &= \tilde{S}_x cos(\omega t) - \tilde{S}_y sin(\omega t) \\ S_y &= \tilde{S}_x sin(\omega t) - \tilde{S}_y cos(\omega t) \\ S_z &= \tilde{S}_z, \end{aligned} \tag{5.15}$$

that shows the role of the oscillating magnetic field $\mathbf{B_{RF}}$, which generates coherent precession of the atomic spin component in the plane perpendicular to $\mathbf{B_0}$. The probe beam, that propagates along the x-axis, detects the S_x component of the spin, that can be obtained by replacing the $\tilde{S}_x$ and $\tilde{S}_y$ in the first equation of 5.15 with the values obtained in equation 5.14

$$S_x = \frac{1}{2} S_0 \gamma B_{RF} \frac{T_2 cos(\omega t) + \Delta\omega T_2^2 sin(\omega t)}{1 + \gamma^2 (B_{RF}/2)^2 T_1 T_2 + \Delta\omega^2 T_2^2}. \tag{5.16}$$

The atomic response represented by Equation 5.16 is a Lorentzian curve with an absorptive component that is in-phase with the oscillating field and a dispersive component that is out-of-phase with the oscillating field. The absorptive curve is centred around ω_0 and its maximum amplitude is obtained when the amplitude of the oscillating magnetic field is $B_{RF} = 2/\gamma\sqrt{T_1 T_2}$. The magnetometer sensitivity is proportional to the gradient of the dispersive profile, which is maximised when $\omega = \omega_0$.

The Full-Width-Half-Maximum (FWHM) of the Lorentzian distribution is

$$\Gamma = \frac{1}{T_2} \sqrt{1 + \gamma^2 (B_{RF}/2)^2 T_1 T_2}, \tag{5.17}$$

and is also called magnetic linewidth. From Equation 5.16 it is easy to see that the magnetometer signal S_x is proportional to the polarisation S_0 along the DC magnetic field direction and to the amplitude of the oscillating RF field. The amplitude B_{RF} also affects the magnetic linewidth of the signal. Therefore this parameter must be chosen in order to obtain a large signal without causing an excessive broadening of the resonant line.

When a resonant oscillating magnetic field $\mathbf{B_{RF}}$ is applied and the atomic sample is highly polarised, then the transverse polarisation produced by $\mathbf{B_{RF}}$ along the x-axis is given by

$$P_x = \frac{1}{2}\gamma B_{RF} T_2 sin(\omega_0 t), \tag{5.18}$$

which is approximately the ratio between S_x and S_z calculated in Equation 5.16 and 5.14, respectively, and it is proportional to the angle of rotation of polarisation of the probe beam θ according to Equation 5.8. The measurement of θ therefore corresponds to a measurement of the oscillation of the transverse component of the spin at a frequency ω_0.

5.2 Magnetometer sensitivity

The sensitivity of a magnetometer is a fundamental parameter to evaluate the efficiency of these devices and a useful tool in order to characterise them. An RF-OAM measures variations of the coherently driven precession between Zeeman sub-levels of the atomic ground state, therefore the sensitivity of this magnetometer is related to the linewidth of the spectroscopic measurement of the energy splitting between those sub-levels. In detail, the proportionality between the sensitivity of an RF-OAM and the linewidth of the Zeeman transitions is given by [113]

$$\Delta B = \frac{\hbar}{g_F \mu_B} \frac{FWHM}{SNR}, \tag{5.19}$$

where $\hbar$ is the reduced Planck's constant, g_F is the Landé factor, μ_B is the Bohr magneton, FWHM is the Full-Width-Half-Maximum of the spectroscopic measurement and SNR is the Signal-to-Noise ratio (SNR). From Equation 5.19 it is clear that a smaller FWHM and a higher (SNR) of the transition result in a larger sensitivity of the magnetometer, defined as the smallest variation of a magnetic field ΔB that the device can detect. The magnetometer sensitivity can be improved by maximising the spin-polarisation lifetime as both the linewidth and the SNR in Equation 5.19 depend on relaxation processes. There are many different effects that can shorten the atomic spin-polarisation lifetime. Collisions between alkali atoms is the

dominant one. Other relaxation processes that depolarise atoms are the collisions between atoms and the wall of the cell and the interaction between atoms and the probe beam.

5.2.1 Spin-destructing collisions

At high vapour densities, collisions between alkali atoms are one of the main causes of atomic depolarisation because these collisions lead to a change of electron spins. Spin-destructing collisions can cause a change of hyperfine states for both atoms, causing a redistribution of the atomic population between the Zeeman sub-levels. The precessing motions of atoms in different sub-levels are characterised by approximately the same frequency but opposite directions, causing decoherence that leads to relaxation of the transverse spin components.

5.2.2 Probe beam interaction

Another process that contributes to the depolarisation of the atomic sample is the interaction between the atoms and the probe beam. The absorption of a photon from the probe beam destroys the atomic polarisation. Therefore minimising the probe beams perturbation results in a longer coherence lifetime of the atomic spin. The impact of the probe beam on the polarisation of the atomic sample can be reduced by decreasing the intensity of the beam and by detuning the beam far from resonance. The consequence of a weaker interaction between the atoms and the probe beam is a reduction of the SNR. Therefore an optimisation of these parameters must be performed in order to obtain the highest possible sensitivity.

5.3 Fundamental noise limits

The fundamental limit of sensitivity for an OAM is ultimately imposed by quantum fluctuations associated with the atoms, that constitute the sensor, and the photons which are probing it. In detail, the total quantum uncertainty in the measurement of the magnetic field is given by

$$\delta B = \sqrt{\delta B_{\mathrm{spn}}^2 + \delta B_{\mathrm{psn}}^2}, \tag{5.20}$$

where the two sources of quantum noises are the spin-projection noise and the photon shot noise, respectively. The first term refers to quantum mechanical uncertainty that arises when the projection of a spin-polarised atom is measured. The second term is related to the uncertainty in the number of photons within each of the two opposite circular polarisations composing the probe beam. For an RF-OAM, the oscillation of the spin-component along the direction of propagation of the probe beam is proportional to the amplitude of the detected magnetic field and the signal of the magnetometer is obtained by measuring the oscillation of this component. Therefore in order to evaluate the two uncertainty sources in Equation 5.20 in terms of noise in the magnetic field measurement, it is necessary to determine the proportionality between the spin polarisation physically measured and the magnetic field calculated.

5.3.1 Spin-projection noise

The spin-projection noise is a consequence of the commutation properties of the transverse component of the atomic spin and of the finite number of atoms involved in each measurement. Considering an atomic ensemble spin-polarised along the z-direction, the transverse components of the spin polarisation S_x and S_y do not commute and therefore their measurements are subjected to the quantum fluctuation governed by the uncertainty principle

$$\delta S_x \delta S_y \geq \frac{|\delta S_z|}{2}. \tag{5.21}$$

The uncertainty of the transverse component is minimised when the longitudinal component of the atomic spin S_z is maximised, that corresponds to maximise the degree of spin-polarisation. Assuming $\delta S_x = \delta S_y$, the uncertainty of the transverse component is

$$\delta S_x = \delta S_y = \sqrt{\frac{\langle \delta S_z \rangle}{2N}}, \tag{5.22}$$

where N is the number of atoms in the atomic ensemble. The spin-projection noise for an RF-AOM in terms of uncertainty in the magnetic field measurement is calcu-

lated in [76]

$$\delta B_{\mathrm{spn}} = \frac{1}{\gamma}\sqrt{\frac{8}{S_z N T_2}}. \tag{5.23}$$

5.3.2 Photon shot noise

The photon shot noise arises from the measurement of the Faraday rotation of the probe beam. In this work, this measurement is performed with a balanced photodiode, where the angle of rotation is measured via the variation of flux in the two arms of the polarimeter. The uncertainty in the photon flux in each detection arm leads to an uncertainty in the rotation angle ϕ given by

$$\delta\theta = \sqrt{\frac{1}{2\Phi}}, \tag{5.24}$$

where Φ is the total photon flux and the rotation angle has been assumed to be small, so the flux in the two arms Φ_1 and Φ_2 are similar and their uncertainties are $\delta\Phi_1 = \delta\Phi_2 = \sqrt{\frac{\Phi}{2}}$. The amplitude of the rotation angle is affected by the atomic polarisation component along the direction of the probe beam propagation, as seen in Equation 5.8, and the uncertainty over P_x is given by

$$\delta P_x = \frac{3}{\pi l r_e c n D(\nu)}\delta\theta. \tag{5.25}$$

which corresponds to an uncertainty in the magnetic field measurement

$$\delta B_{\mathrm{psn}} = \frac{6}{\gamma T_2 \pi l r_e c n D(\nu)}\delta\theta. \tag{5.26}$$

The photodiode efficiency must be taken into account when calculating the photon shot noise to avoid to over-estimate the effective number of atoms detected by the polarimeter. The photon shot noise will therefore increase by a factor $1/\sqrt{\eta}$, where η is the photodiode quantum efficiency.

5.4 Cold atoms magnetometer

Some of the relaxation processes mentioned in Section 5.2 are negligible when the sensor is constituted by ultra-cold atoms instead of a room temperature vapour. In detail, spins of alkali atoms at room temperature can depolarise immediately after colliding with the walls of the glass cell because this interaction completely randomises the orientation of the atomic spin, unless dedicated organic coatings such paraffin are employed [114, 115]. This relaxation effect, deeply detrimental with thermal atoms, is completely suppressed with a cold atoms RF magnetometer because of the high spatial confinement that characterises the atomic cloud and because of the different methodology adopted to acquire measurements. When using cold atoms, the signal cannot be continuously acquired for an indefinite amount of time, which is the case with thermal vapour. The duration of the acquisition time depends on the average lifetime of the atomic cloud, which is a fundamental factor when considering the coherence lifetime of the atomic spin in this type of magnetometer. Moreover, each measurement is likely to be destructive: after the acquisition of the signal, the atom cloud needs to be re-created and cooled. Therefore, just the trapped atoms will be optically pumped and analysed by the probe beam which means there are no interactions with the wall of the cell.

Factors that contribute to enlarging the linewidth in Equation 5.19, such as the Doppler broadening in the optical spectra and the collisional broadening due to interactions with a buffer gas, are negligible when ultra-cold atoms are adopted as a sensor. In this case, the detuning of the probe beam can be smaller, compared to a room temperature OAM, because of the narrower linewidth of the absorption transition and because of the inevitable destructive nature of the measurements, which results in a larger SNR. Also, for a cold atom RF magnetometer, the size of the probe beam has to match the size of the atomic cloud that constitutes the magnetometer sensor in order to interact with the largest number of atoms possible, and so maximising the optical signal acquired.

Moreover, the signal obtained in OAM with thermal atoms is usually characterised by motional averaging, where the atoms contained in the cell statistically contribute

to the signal because of their thermal displacement, the large volume of the sensor and the duration of the measurements. A different approach is adopted when the measurements are performed with cold atoms: the average thermal motion of the atoms is reduced resulting in a spatially confined atomic cloud in which, if overlapped to the region where pump and probe beam intersect, ideally all the particles contribute to the signal. Due to the small volume of atomic traps and to the low temperatures of ultra-cold atoms, these particles result to be highly spatially localised. The atoms, therefore, will evolve only under the local magnetic field and will not experience different precession frequency due to large magnetic field gradients along the cell, allowing high spatial resolution field measurements. The trapping techniques adopted through the cooling process increase the local atomic density and reduce the thermal atomic motion producing a near-stationary collection of atoms with long coherence times.

Despite these positive aspects, trapped atoms cannot provide the highest sensitivity to uniform magnetic fields when compared to a room temperature OAM. Due to the small volume of atomic traps and because of the limitation on spatial density, the total number of trapped atoms is typically on the order of $10^5 - 10^8$, much smaller than the typical number of atoms in a cm-sized cell typically used in a room temperature OAM ($10^{11} - 10^{15}$ atoms). Consequently the overall number of atoms interrogated by the probe beam is smaller for a cold atom magnetometer. Moreover, the possibility to acquire measurements in continuous mode in room temperature OAM allows the integration of the signal over time, increasing the sensitivity of the device. This implies that trapped atoms cannot provide the highest sensitivity to uniform magnetic fields but they are the ideal candidate for high spatial resolution measurements.

5.5 Towards the realisation of a cold atom magnetometer

In this section the experimental apparatus implemented to observe the atomic spin precession of cold ^{87}Rb atoms through Faraday rotation is described. As mentioned

in the Introduction, the final aim of the project is the realisation of a RF-OAM whose sensor consists of a ^{87}Rb BEC.

Once the experimental apparatus for the acquisition of magnetometry measurements was implemented, we decided to first obtain the Faraday rotation signal with laser-cooled atoms in order to characterise the system, before proceeding to perform measurements with the condensate. The atomic sample used in this first stage consisted of ^{87}Rb atoms trapped in a MOT and then further cooled through sub-Doppler technique as described in Section 4.4. This procedure allows us to have a dense atomic sample ($\sim 10^{11}$ atoms/cm^3) containing a large number ($> 10^8$) of cold atoms ($\sim 20\mu$K). Having a large dense cloud of atoms is a factor that facilitates the observation of the signal since the amplitude of the Faraday rotation is proportional to the distance l travelled by the probe within the sensor and to the atomic vapour density n as shown in Equation 5.8.

The work done so far to obtain the first RF-OAM signal is presented in the following section. For the time being, we successfully managed to observe the Faraday rotation signal and we are currently in the process of characterising and optimising the setup. Many parameters still need to be tested and, contrary to an OAM at room temperature, the measurements cannot be performed continuously and therefore the acquisition timing become essential and needs to be further investigated.

5.5.1 Experimental setup

The implementation of a cold atoms magnetometer required the addition, to the BEC apparatus, of few optical elements and the creation of a LabVIEW software for real-time acquisition of the signal. The DC magnetic field for the optical pumping and the pump beam were already implemented in the original setup, described in Chapter 3. Considering the reference system in Figure 3.1, the DC magnetic field is applied along the z-direction with the pump beam parallel to it, propagating along $-\mathbf{z}$. A zoom of the sensor area is shown in Figure 5.5, where the main components of the magnetometer are indicated. The beam used as a pump beam corresponds to the absorption imaging beam and overlaps with the MOT beams along the z-axis (see Section 4.5). The pump beam has a diameter of 1.5 cm and an intensity of

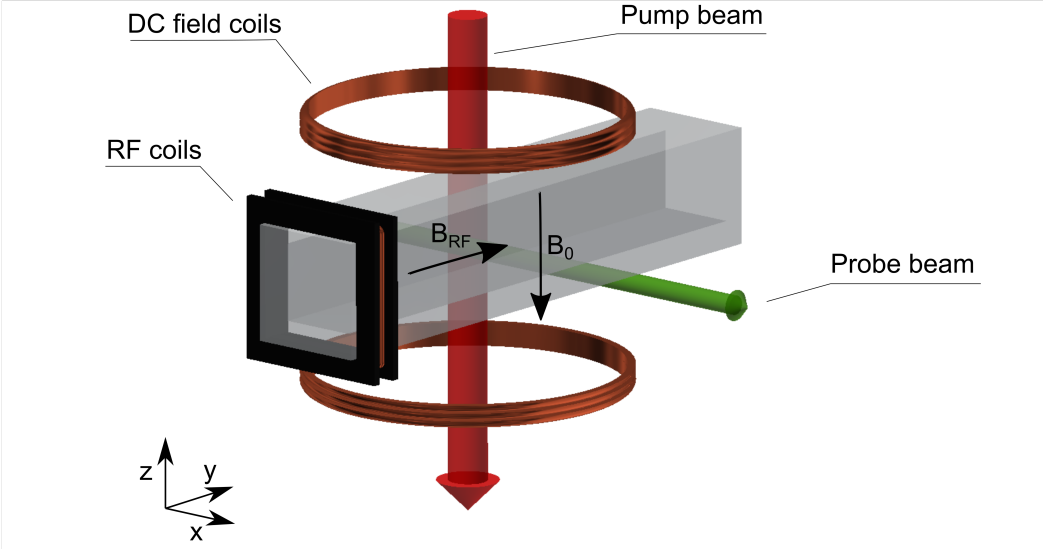

Figure 5.5: Schematic of the experimental setup in the region of the sensor. The pump beam (red line) propagates along the z-direction, parallel to $\mathbf{B_0}$ (generated by the two Helmholtz coils), while the probe beam (green line) propagates along the x-axis. The pump and the probe beam lie on the same x-z plane. The oscillating RF magnetic field is applied along the y-axis $\mathbf{B_{RF}} = B_{RF}cos(\omega t)\mathbf{y}$ via a coil directly attached to the cell.

$57\mu W/\text{cm}^2$. The beam is circularly polarised and it's resonant with the transition $|F = 2\rangle \longrightarrow |F' = 3\rangle$ of the ^{87}Rb D2 transition. The intensity and the detuning of this beam are controlled via an AOM[2]. The output light of the AOM is then fibre coupled and sent to the cell. A shutter, positioned before the AOM is implemented to ensure no light is arriving on the chamber when the pump beam is closed.

The amplitude of the actual magnetic field experienced by the atoms during the optical pumping stage $\mathbf{B_{TOT}}$ in the atomic region is produced by the 3 orthogonal compensation coils, as explained in 4.5. A critical step that we have identified in the experiment is the direct measurement of the amplitude of $\mathbf{B_{TOT}}$, which imposes the resonant frequency of the system. For obvious reasons was not possible to move the cell, that is attached to the ions pumps and to the first MOT chamber, to measure the amplitude of the total magnetic field in the atoms position. An estimation of it was obtained by measuring the magnetic field in different positions all around the cell and then extrapolating the value in the trap region. Direct ac-

[2]AA Optoelectronic, model: MT80-A 1,5-IR.

cess to the cell is reduced, partly due to the presence of optics but mainly due to the presence of the coils for the quadrupole field. A sensor[3] was used for this task, which dimensions are: 1.5 cm$\times$ 1.5 cm$\times$ 2 cm. The compactness of this sensor allowed us to measure the components of the magnetic field directly adjacent to the cell, in between the quadrupole coils. The gradients around the cell region were calculated and a calibration of the magnetic field $\mathbf{B_{TOT}}$ in the atoms position was performed by varying the current supplied to the coils. We firstly set the value of the compensations coils along the z-direction to obtain a DC magnetic field in that direction corresponding to a Larmor frequency of $\sim$ 100 kHz. Secondly, the magnetic field generated by the other two pairs of compensation coils and the Helmholtz coils along z (that overcompensate the field given by the compensation coils in this direction) was optimised in the sub-Doppler cooling stage. To ensure an efficient cooling process, once the quadrupole magnetic field is switched off, the coils must eliminate strong environmental magnetic gradients that might decrease the lifetime of the atomic molasses. The result of this stage is the reduction of the magnetic fields orthogonal to the DC field. The resulting component of $\mathbf{B_{TOT}}$ along z was 123 mG, giving a Larmor frequency of 86 KHz. This value was calculated knowing the conversion factor of the sensor (8.9 mV/mG) and the Zeeman splittings between adjacent magnetic sublevels in the ground state $|F = 2\rangle$ of the D2 lines.

The oscillating magnetic field along the y-direction is generated by an RF generator [4] connected to a coil placed 3 cm from the atoms position. The support of the coil is made of plastic and can be directly attached to the end of the cell, as shown in Figure 5.5. 40 turns of copper wire[5] were wrapped to make the coil, which is a square (3 cm$\times$ 3 cm), in order to fit the cell.

The probe beam propagates along $-\mathbf{x}$. Its intensity is controlled by an AOM[6]. The waist of the probe beam, measured with a beam profiler, is 5 mm, which is the same size as the atomic cloud. The power of the probe beam can be varied between 7 μW and 1 mW and its intensity is stabilised with a feedback loop via

[3]Bartington Instruments, model: MAG 612
[4]AGILENT KEYSIGHT 33210
[5]RS code: 357-744
[6]AA Optoelectronic, model: MT80-A 1,5-IR

a PID, that modulates the DC amplitude of the RF power sent to the AOM. The

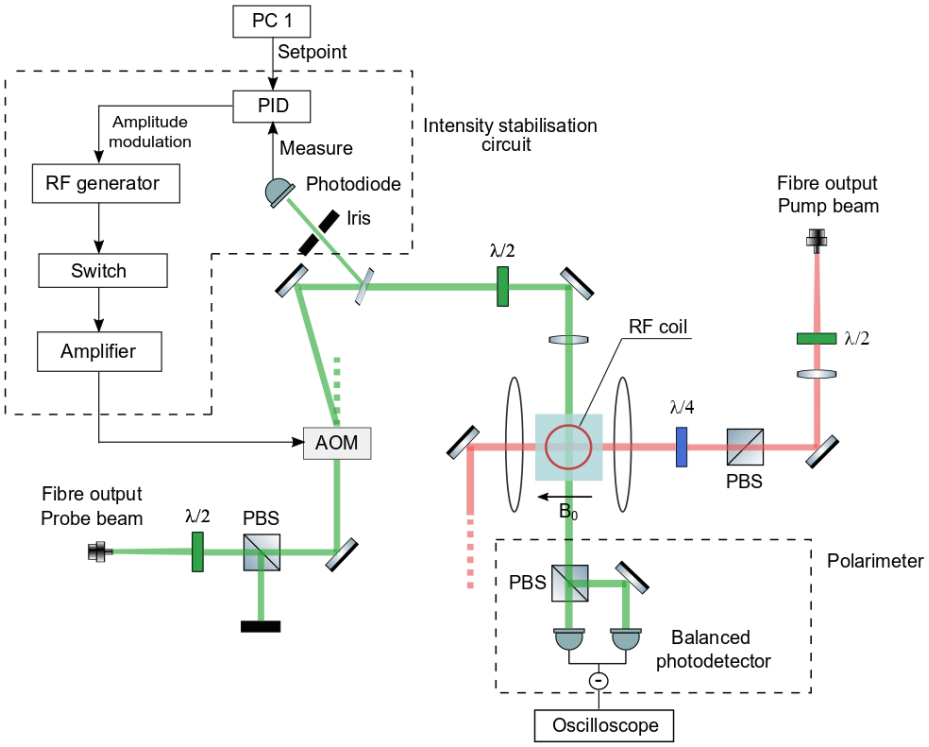

Figure 5.6: Experimental setup for the implementation of an RF-OAM, whit the power of the probe beam stabilised with feedback loop via a PID. The green line represents the probe beam while the red line represents the optical path of the pump beam. In order to give a clear idea of the system components the schematic pictures the projection of the experimental setup on a 2D surface. Only the experimental setup relevant to the RF-OAM process is pictured: all the optics for the cooling process are not represented for clarity.

probe beam was initially 2Γ red-detuned from the $|F = 2\rangle \longrightarrow |F' = 3\rangle$ transition between the hyperfine states of the ^{87}Rb D2 line and it was generated by a small fraction (30 mW) of the MOPA output (which is blue detuned of 68 MHz from the aforementioned transition), then injected into an optical fibre to bring the beam closer to the cell area. In that condition, a small variation of the frequency of the probe beam could have been provided via changing the RF frequency that drives the AOM. The range of variation that can be obtained with the AOM in use is ± 20 MHz from the central frequency, which is 80 MHz. Although small powers were used, the detuning of the probe beam was too small and, with this setup, no signal was observed. In order to have the possibility of exploring a larger range of detuning for the probe beam, a home-made laser in Littrow configuration was set-up

and tuned on the ^{85}Rb D2 line. The possibility, given by the high tunability of the cavity, to lock the laser on any of the ^{85}Rb D2 transitions allows a detuning of the probe beam of 1.25 GHz or 4 GHz for the less and the more energetic group of transitions, respectively. The laser frequency is stabilised by a Dichroic-Atomic-Vapor Laser Lock (DAVLL) system [116, 117] which exploits the saturated absorption spectroscopy signal and gives the possibility to lock the laser on the hyperfine transitions. The laser output is fibre coupled and, once delivered near the cell, stabilised in intensity. After the fibre, a Half Wave Plate (HWP) and a polarising beam splitter are subsequently positioned in order to control the power of the transmitted component of the PBS. The transmitted linearly polarised light is sent to the AOM, where the power in the first diffracted order is optimised and used as probe beam. The frequency of the probe beam, therefore, is detuned by 80 MHz after the passage in the AOM. A small fraction of the probe beam is collected after the AOM, with a thin glass, and sent to a photodetector to provide the measurement necessary for the stabilisation feedback loop, as illustrated in Figure 5.6. An iris is positioned before the photodetector to eliminate the stray light and to ensure only the -1 order from the AOM is detected. Before reaching the cell, the probe (which is already linearly polarised) travels through an HWP. By adjusting the position of the fast axis of this HWP, it is possible to balance the two orthogonal polarisations in the two channels of the polarimeter in order to have an RF signal that equals zero when the rotation in polarisation is absent.

After travelling through the cell, the rotation of the probe beam polarisation is detected by a polarimeter realised with a polarisation-dependent beam splitter, set at 45° to the initial polarisation direction, and a balanced photodetector. The two orthogonally polarised components of the probe beam are separated by the polarising beam splitter and then sent to the two branches of a PDB210 A/M Thorlabs balanced photodetector, which detects two separate beams with intensity respectively of I_1 and I_2. For small rotations $\theta \ll 1$, the difference of the two intensities gives the angle of rotation [76]

$$\theta = \frac{I_1 - I_2}{2(I_1 + I_2)} \tag{5.27}$$

The difference of the signals in the two arm is amplified by the photodetector and constitutes the polarimeter output.

5.5.2 Sequence routine

After the implementation of the experimental apparatus, we firstly attempted to observe a RF-OAM signal by using an atomic cloud cooled via polarisation gradient mechanism. The experimental routine performed to obtain the signal is schematically represented in Figure 5.7. After 20 s of MOT loading time, 12 ms are spent in

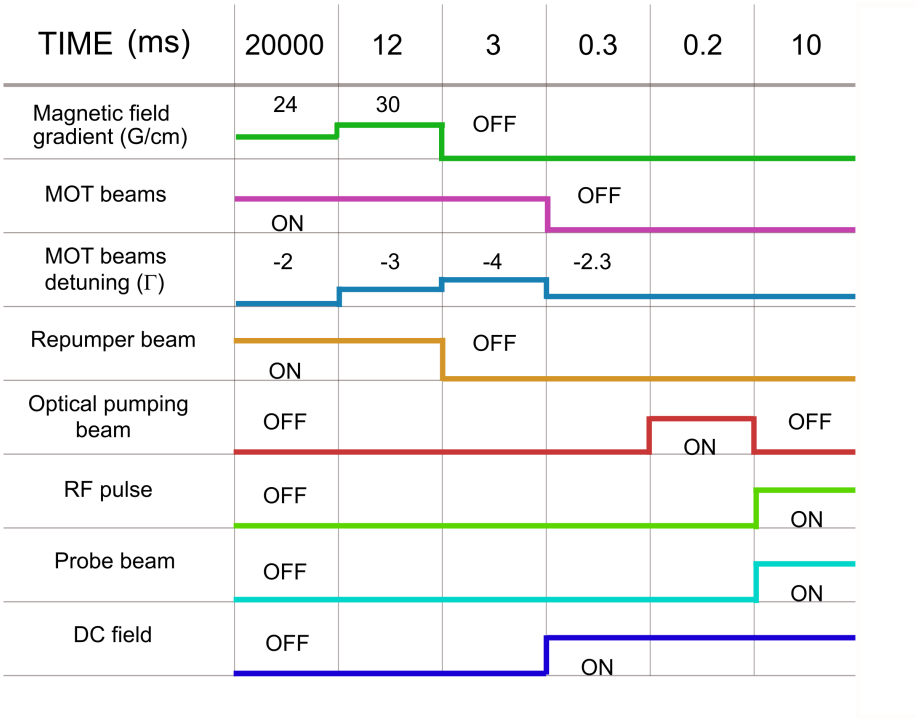

Figure 5.7: Diagram of the experimental sequence performed to generate and acquire an RF-OAM signal. The specifics of each phase is indicated, along with its duration (top row).

order to compress the MOT and to increase the atomic spatial density via changing the detuning of the MOT beams and the magnetic field gradient (C-MOT phase). Then the magnetic field gradient is switched off and, for 3 ms, the MOT beams are further detuned from the cooling transition, resulting in a polarisation gradient process able to cool the atoms at sub-Doppler temperature ($\sim 20\ \mu K$). External environmental magnetic fields are significantly suppressed and compensated by three orthogonal sets of Helmholtz coils surrounding the cell, that are constantly on for

the duration of the entire routine and allow us to efficiently trap the atoms and to decrease the noise in the measurement of the Faraday rotation. After the polarisation gradient cooling mechanism, the atoms are optically pumped by a circularly polarised light pulse along the z-direction, resonant with the cooling transition. The duration of the optical pumping pulse is 0.2 ms while the total duration of the DC magnetic field, necessary to create the spin polarisation along **z**, is 10.5 ms. The 0.3 ms delay is a practical choice dictated by the need of having sufficient time for the laser to reach the appropriate detuning. After having obtained an efficient spin-polarisation, the RF pulse is generated and, at the same time, the probe is switched on. The duration of this last phase is currently 10 ms. The intensity of the probe beam is controlled by the AOM, and is set via computer. In order to minimise the perturbation of the precessing atomic ensemble, the intensity of the probe beam is 60-100 μW, while the detuning is -4 GHz.

The signal we are looking for is an oscillation of the polarimeter RF signal, given by the rotation of polarisation of the probe beam, with a frequency equal to the Larmor frequency. Therefore an efficient way to extract information from the polarimeter signal is the calculation of its Fast Fourier Transform (FFT), which reveals the presence of a resonance peak in the frequency spectrum. In order to collect the data and quickly analyse them, the output of the balanced photodetector is read by an oscilloscope (TeKtronix, DPO2014B - Oscilloscope, DPO2000B Series, 4 Channel). When the probe beam is switched on, the signal is recorded by the oscilloscope and immediately sent to the computer, via USB cable, where it is acquired via bespoke LabVIEW software. Along with the storage of the data, this software is also able to perform the FFT of the polarimeter signal and to save the information. Moreover, through this software, the parameters of the $\mathbf{B_{RF}}$ generator are set (frequency, amplitude), along with the parameter to visualise the signal on the oscilloscope (time scale and amplitude scale of the signal). To synchronise the acquisition of the signal with the RF pulse and the probe beam all the elements are triggered by the same signal, as shown in Figure 5.8. The main trigger is generated by one computer (PC1), which is the computer that runs the entire experimental

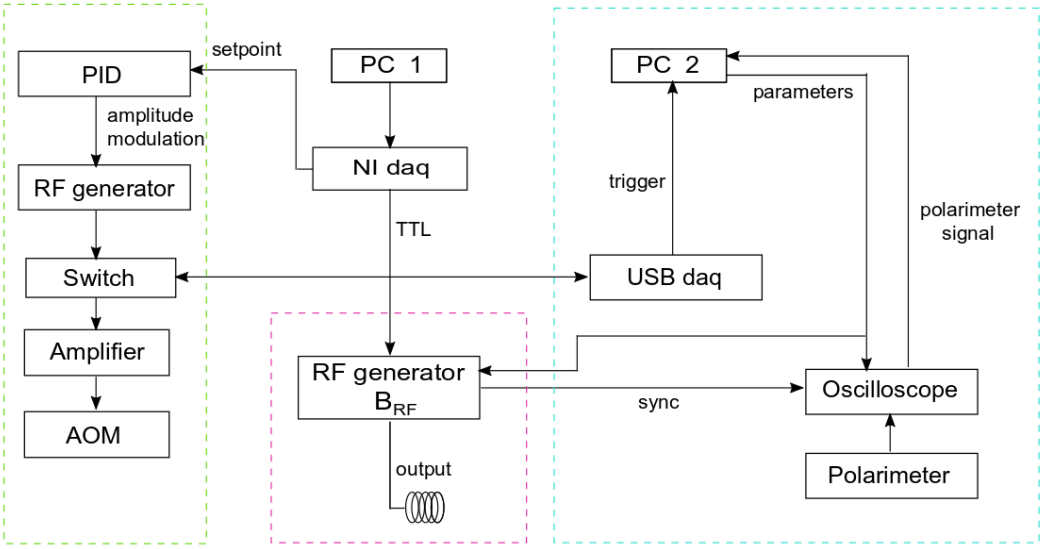

Figure 5.8: Diagram of the instrumentation connections to generate and acquire an RF-OAM signal. The trigger for the RF pulse is generated by a computer (PC1) via a NI DAQ and then sent directly to the RF pulse generator as an External trigger. The same TTL from the DAQ is used to drive a switch that, when open, supply power to the AOM for the probe beam, and is also sent to a second computer (PC2) via a USB board that triggers the acquisition of the signal via oscilloscope.

sequence, for the BEC experiment. The trigger is a TTL given by one of the digital channel in the software represented in Figure 3.8, physically generated by a NI DAQ board connected to PC1 and sent to three different instruments (see Figure 5.8):

- to the switch that is positioned between the RF generator (that supplies the RF power to the AOM controlling the probe beam) and the amplifier. The probe beam AOM is switched on via PC1 that set the beam power via the PID setpoint. The choice of using a switch (driven by a TTL signal) to open/close the flux of RF allows us to suppress possible gradients in the probe beam power due to transients in RF power. The RF generator is therefore switched-on 1 ms before the TTL signal is sent to the switch.

- to the RF generator to create the RF pulse. The RF generator is used in burst mode: its output is generated while the external trigger is on. The external

trigger is supplied by the NI DAQ connected to PC1 which is the same that drives the probe and the acquisition. The output signal of the RF generator is sent to the RF coil and it is synchronised with the oscilloscope acquisition: the SYNC signal from the generator constituted the oscilloscope trigger.

- to the USB DAQ that is connected with a second computer (PC2) to start the acquisition of the signal. The acquisition of the oscilloscope trace by the LabVIEW software is triggered by the TTL signal read from the USB DAQ. When the TTL is on, the polarimeter signal is acquired via oscilloscope for a duration that can be set via software and that must ideally cover the duration of the TTL signal.

5.5.3 Preliminary results

The first signal of our OAM was observed shortly before the submission of this manuscript, therefore only preliminary results are presented in this section.
In Figure 5.9 the blue solid curve shows the first signal observed of the Faraday rotation of the probe beam polarisation as a function of the frequency. Specifically, the graph represents the power spectrum of the RF polarimeter output and clearly shows a peak in frequency, corresponding to the oscillating field ω applied during the measurement (99 kHz). The green solid line is the signal collected when no optical pumping is performed during the sequence, resulting in a peak whose amplitude is 1/5 of the corresponding signal with atoms optically pumped. This is in accordance with the expectation: no optical pumping means that the atoms are equally distributed between the magnetic sub-levels and no macroscopic atomic polarisation is achieved. Only the fraction of atoms (roughly one-fifth of the population) in the sub-level $|F = 2; m_F = +2\rangle$ is actually contributing to the optical signal. The light-blue solid line represents the power spectrum of the RF polarimeter output when the quadrupole magnetic field is switched off and therefore no atoms are trapped. It is obvious to observe that without atoms the Faraday rotation signal is absent. These measurements were performed by running the experimental sequence described in Figure 5.7 and the signals were collected and averaged firstly when the atoms were

optically pumped, then when the optical pumping beam was switched off and finally when no atoms were present. It is important to stress that this last measurement was performed by maintaining the same sequence (i.e. oscillating field $\mathbf{B_{RF}}$ active along with the probe beam for the last 10 ms) in order to be used as a background measurement and test that no induction signals were picked by the polarimeter because of the $\mathbf{B_{RF}}$ field. The amplitude of the oscillating magnetic field during this measurement is 80 mG while the probe beam intensity is 0.17 mW/cm^2 and its detuning is $\Delta \simeq 4$GHz.

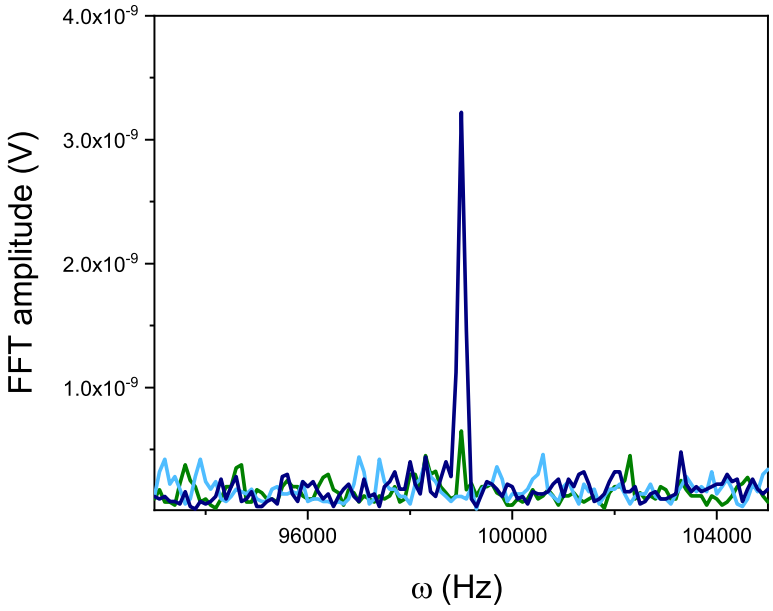

Figure 5.9: Power spectrum of the RF polarimeter output showing the Faraday rotation of the probe beam polarisation as a function of the frequency. The blue solid curve shows the first signal observed of the Faraday rotation of the probe beam polarisation when atoms are optically polarised. The green solid line is the signal collected when no optical pumping is performed during the sequence while the light-blue solid line represents the power spectrum of the RF polarimeter output when the quadrupole magnetic field is switched off and therefore no atoms are trapped. Each of the plotted lines is the average of 5 measurements.

An aspect worth investigating is how the response of the magnetometer changes when the frequency of the oscillating field ω is varied while the DC-field is constant. An example of this measurement is presented in Figure 5.10, where the first graph shows the superposition of 23 different power spectra of the polarime-

ter output acquired for 23 different values of ω. The ω frequencies were chosen in order to cover all the range of frequency, around the resonant one, where our magnetometer is sensitive. It's noteworthy to mention that, in a very short time, we managed to increase the SNR amplitude through a first rapid optimisation. Mainly we varied the amplitude of the probe beam, its intensity and detuning, the amplitude of the RF, and the temporal sequence of the whole process. The best parameters were chosen to perform the following measurements. In Figure 5.10 a) all the FFTs are plotted as a function of ω. Each plot is obtained by averaging 10 measurements and the frequency of the peak corresponds to the frequency ω applied in that specific measurement. The DC-field is fixed at a value corresponding to 84 kHz, which is in agreement with the result given by the Lorentzian fit in Figure 5.10 b), where the amplitude of the FFT peaks are plotted as a function of the frequency. The amplitude of the oscillating magnetic field during this measurement is 1.92 mG, the probe beam intensity is 0.17 mW/cm^2 and its detuning is $\Delta \simeq 4$GHz. From the graph in Figure 5.10 b) it is possible to derive a preliminary estimate of the sensitivity of our magnetometer, which is given by Equation 5.19. In this Equation, g_F is the Landé factor for the $|F = 2\rangle$ ground state of the D2 line of ^{87}Rb, FWHM is the measured Full Width Half Maximum of the fitted curve in Figure 5.10 b) and SNR is the Signal-to-Noise ratio given by the ratio between the amplitude of the peak and the averaged noise in the fast Fourier spectra. This preliminary measurement gives a sensitivity of 12.8 nT/$\sqrt{\text{Hz}}$[7]. The graphs in Figures 5.9 and 5.10 a) were obtained by calculating the FFT of the polarimeter output. An example of this signal is illustrated in Figure 5.11, where the trace acquired for 10 ms is shown. In the upper right corner a zoom of the trace is presented, where a solid red line represents the sinusoidal fit calculated over 11 periods. From the zoomed signal is possible to observe the modulation in the polarisation of the probe beam induced by the precessing atoms which occurs with a frequency equal to the resonant frequency of the system. The sinusoidal fit gives a frequency of 57 kHz, which is the frequency of the oscillating magnetic field ω applied during the measurement. By

[7]Undergoing optimisation of the system should significantly improve this performance in the short range.

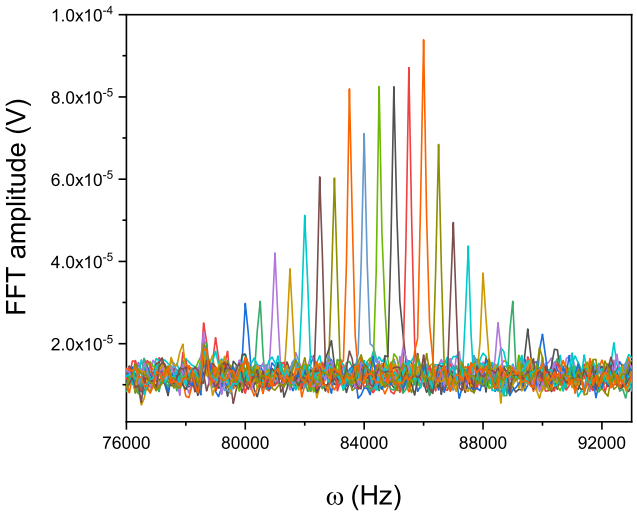

(a)

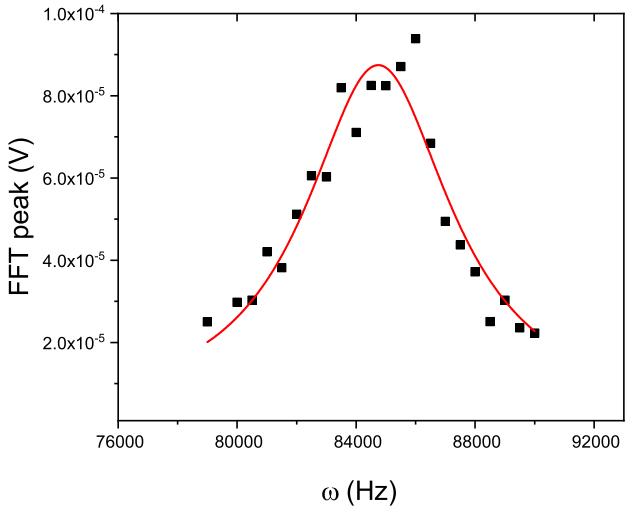

(b)

Figure 5.10: FFT of the polarimeter output as a function of ω, acquired for 23 different values of ω. In detail: a) Superposition of 23 different power spectrum of the polarimeter output acquired for 23 different values of frequency of $\mathbf{B_{RF}}$ within a range of $79-90$ kHz. b) For clarity, the amplitude of the 23 peaks of the FFTs are plotted as a function of ω and then fitted with a Lorentzian curve (red solid line) that gives a central frequency of 84 kHz.

fitting the full trace with a damped sine wave, we obtained an exponential time constant $\tau = 7.48 \pm 0.03$ ms, which is the interaction time between the atoms and the probe beam. The limited duration of the magnetometer signal is given by different

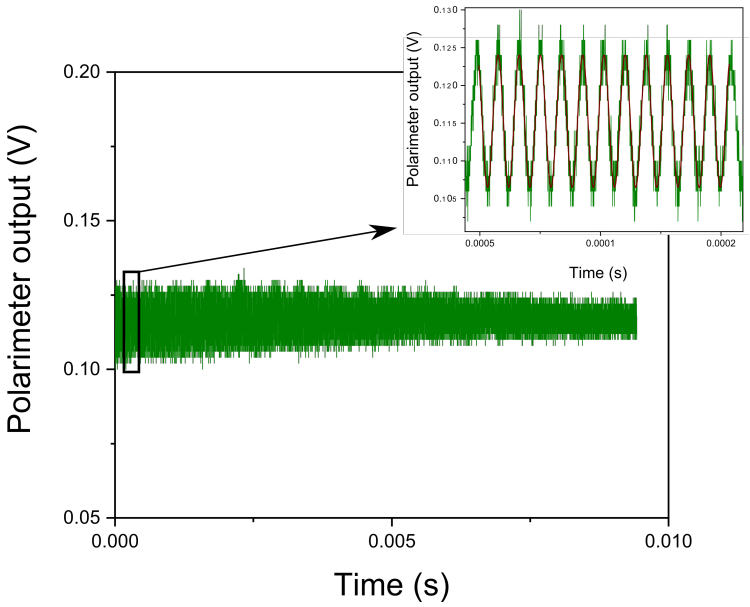

Figure 5.11: Polarimeter output, which is given by the subtraction of the signals collected in the two branches of the photodector. The signal was recorded for 10 ms. In the upper right corner of the graph, a zoom of the trace is presented, where a red solid line represents the sinusoidal fit calculated over 11 periods that gives a frequency of 57 kHz, which is the resonant frequency of the system. By fitting the full trace with a damped sine wave, we obtained an exponential time constant τ =7.48 ms.

factors. The main one we have to consider is the lifetime of the atomic cloud. When the atoms are released from the molasses phase they are free to expand. But they will only be spatially localised and coherently oriented only for a limited amount of time due to atomic collisions, thermal motion and gravity. Therefore, the sensing element used in this magnetometer can be probed for a limited amount of time.

The other main limiting factor is the interaction of the atomic cloud with the probe beam. Although a strong interaction between them gives a large optical signal, at the same time it leads to the depolarisation of the atoms. In our case, once the atoms are depolarised, they will no longer contribute to the signal and, as the probing phase goes on, a smaller number of atoms will contribute to the measurement. In order to increase the interaction time between the atoms and the probe beam, both the

aforementioned factors need to be considered. On one side a longer lifetime of the trapped atoms can be obtained, by further lowering their temperature. On the other side, a more controlled interaction with the probe beam can be tested, by finding the optimal detuning and intensity of this beam. It is important to investigate which factor is the most relevant one because the interaction time between the atoms and the probe beam is a limiting factors for the sensitivity of our magnetometer. The maximum sensitivity that can be obtained with our magnetometer, given an interaction time τ can be calculated with Equation 5.19, by estimating the FWHM with Equation 5.17 and considering the relaxation time τ instead of T_1 and T_2. This calculation of the sensitivity, based on the estimated linewidth, gives a sensitivity of 11.1 nT/$\sqrt{\text{Hz}}$. This value is in good agreement with the one calculated with the measured FWHM and indicates how the duration of the signal is the main limiting factors in this type of device. From Equation 5.19, it is intuitive to understand how

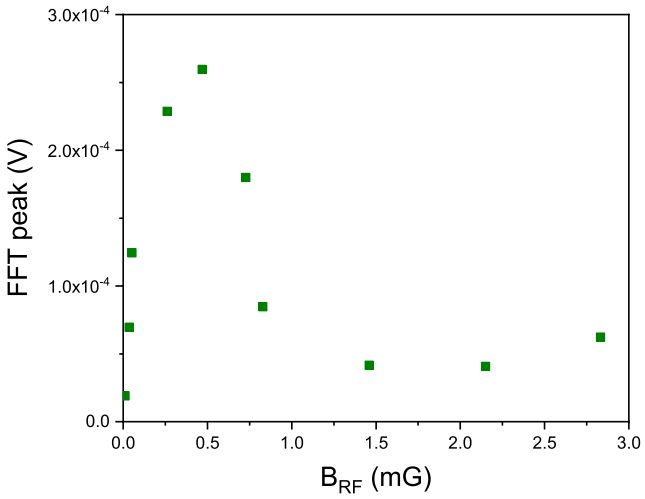

Figure 5.12: Amplitude of the peak of the FFT of the polarimeter signals plotted as a function of $|\mathbf{B_{RF}}|$. Each point represents the amplitude of the peak of the FFT obtained by averaging 10 measurements.

the sensitivity of the magnetometer depends on the ratio $\frac{FWHM}{SNR}$. It is therefore important to optimise both these factors in order to increase the sensitivity of our system. To do so, a systematic optimisation of the setup must be performed, consisting of sequential data collection where one parameter of the system is varied

whilst the others are kept constant. This approach was followed to acquire the measurement showed in Figure 5.12: the amplitude of the FFTs are plotted as a function of the amplitude of the oscillating magnetic field $\mathbf{B_{RF}}$. The Faraday rotation signals were collected following the routine in Figure 5.7. The resonant frequency of the system is 86 kHz, the probe beam intensity is 0.17 mW/cm^2 and its detuning is $\Delta \simeq 4$GHz. The amplitude of the oscillating magnetic field $\mathbf{B_{RF}}$ is varied between 2.83 mG and 0.011 mG during this set of measurements which are the maximum and the minimum magnetic field that we can obtain with our current setup. From Figure 5.12 is possible to observe how the maximum amplitude of the fast Fourier transform is achieved when the amplitude of the oscillating magnetic field is 0.46 mG. This measurement represents only the very first stage of the optimisation and characterisation process of the setup, which will take place in the coming weeks.

Chapter 6

Conclusion and outlook

The first part of this manuscript, reported on the design, implementation and characterisation of the experimental setup for realising a ^{87}Rb BEC. After capturing and pre-cooling the atoms in a magneto-optical trap, the atoms are further cooled and then adiabatically transferred into a hybrid trap, where they undergo forced evaporative cooling processes. The hybrid trap, obtained by overlapping a quadrupole magnetic potential and a far-detuned optical crossed dipole trap must be mechanically stable in order to avoid atomic heating and the resulting losses that would prevent the realisation of the condensate. Therefore, part of our work was dedicated to assemble a mechanically stable optical setup to guarantee an efficient loading and evaporation through a position and intensity stabilisation system. A ^{87}Rb Bose-Einstein condensate was realised with the described setup after an optical evaporation cooling of 6 s with a total number of atoms of 5×10^4. The corresponding critical temperature was 130 nK.

The second part of the thesis was dedicated to the realisation of a cold atoms magnetometer. The theoretical background and the basic principles behind the operation of OAM were introduced, along with the developed methodology for performing measurements through which first results were obtained. The first signal was observed shortly before the submission of this manuscript therefore only preliminary results were presented. Further work still needs to be done and a complete characterisation of the system will be soon performed.

6.1 Current situation and future perspective of the cold atoms magnetometer

Faraday rotation induced by an RF magnetic field in ultra-cold atoms was detected. In order to observe and characterise the signal the routine shown in Figure 5.7 was repeated while the frequency and the amplitude of the oscillating magnetic field were respectively varied. These preliminary tests allowed an estimation of the current sensitivity of the magnetometer, which is equal to 12.8 nT/$\sqrt{\text{Hz}}$ and is limited by interaction time between the atoms and the probe beam.

In the immediate future we plan to systematically run the experiment while sweeping other parameters, such as the detuning and the power of the probe beam, the power of the optical pumping beam and the duration of all the different phases, in the attempt to maximise the magnetometer sensitivity.

Once the optimisation process will be completed, a full characterisation of the apparatus will be performed which includes the study of the response of the system to different Larmor frequency that allows to understand in which range of frequencies our magnetometer can work and with which sensitivity. The spin relaxation time of the system need to be measured and the factors that affect the polarisation lifetime of the atoms will be studied and then accordingly changed to maximise this parameter. The complexity of the setup necessary to realise BECs allows us to have complete control on the atoms and gives the possibility to study the magnetometer response with different conditions of the interrogated particles (i.e. the temperature of the atomic cloud and number of trapped atoms).

To improve the control of the apparatus and its performance a new set of coils for optical pumping will be tested to precisely control the DC magnetic field and the resonant frequency of the system. Also, to carry out a precise characterisation of the apparatus, we plan to replace the oscilloscope with a lock-in amplifier to detect the resonant signal of the system. By supplying the lock-in amplifier with the frequency of the oscillating magnetic field as a reference, the lock-in will amplify the signal in correspondence of this frequency while discarding all the other components from the polarimeter output, maximising the signal-to-noise ratio.

Subsequently the focus will be on the next phase of the experiment: the use of a BEC as sensing element. Further adjustments will be required in this phase and attention will be particularly devoted to the signal acquisition system, which must be extremely stable and sensitive given the low number of atoms. After a characterisation of the device, the investigation of the role of the coherence of the BEC in the magnetometer sensitivity will be studied.

Appendix A

Logarithmic amplifier

The circuit diagram of the AD8304 logarithmic amplifier is shown in Figure A.1. The logarithmic amplifier is supposed to be supplied by a voltage of 8 V between

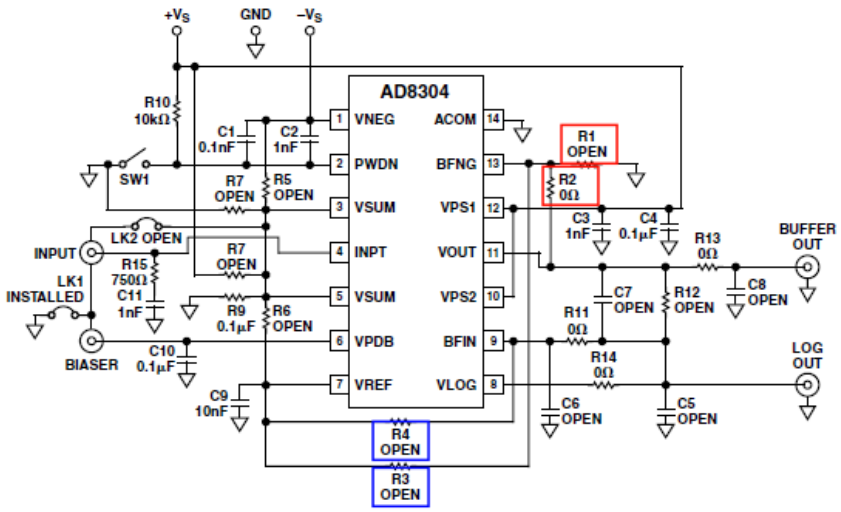

Figure A.1: Electronic circuit of the logarithmic amplifier AD8304. The diagram is taken from the data sheet of the AD8304 logarithmic converter. The highlighted components represent the modified resistors. The blue ones have been changed to adjust the effective logarithmic intercept; the red ones have been modified to adjust the gain of the amplifier.

the VPOS and AGND pins. But we decided to add an offset voltage and to supply a voltage of 8 V between VPOS and VNEG. The red and blue boxes in Figure A.1 show the parts that were modified. The resistor $R1 = open$ and $R2 = 0\Omega$ were both replaced by a 10 kΩ resistors to change the gain of the amplifier. We decided to optimise the gain value via a potentiometer and then to substitute it by a fixed resistors

to minimise the risk of thermal drifts. The resistor $R3 = open$ and $R4 = open$ were replaced by a 6.8 kΩ and 10 kΩ, respectively, to adjust the effective logarithmic intercept. The response of the amplifier system we have built is represented in Figure A.2. Figure A.2 shows that the logarithmic amplifier guarantees greater sensitivity

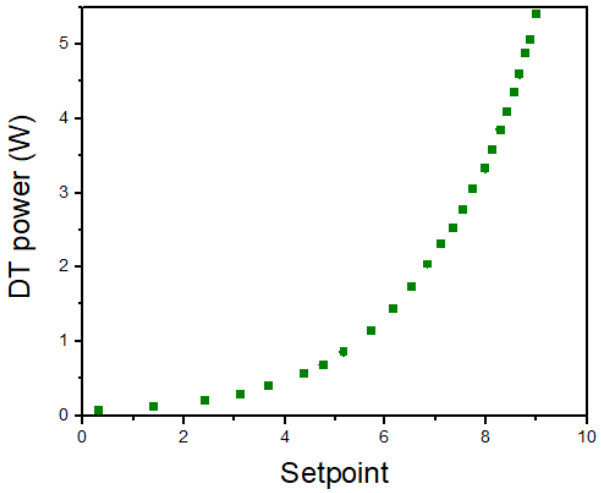

Figure A.2: Power calibration of the first dipole trap beam with the stabilisation system, where the chain of logarithmic and linear amplifiers have been inserted after the photodiode.

at low laser's power and therefore a better power stabilisation in that region. A linear amplifier (Stanford Research Systems - SIM 910 LinAmp) has been positioned between the logarithmic amplifier and the PID in order to extend the dynamic range of the stabilisation system and fully exploit the PID input range (10 V).

Bibliography

[1] S. N. Bose. Plancks Gesetz und Lichtquantenhypothese. *Z. Phys*, 26:178, 1924.

[2] A. Einstein. Quantentheorie des einatomigen idealen Gases. *Sitzber. Kgl. Preuss. Akad. Wiss.*, pages 261–267, 1924.

[3] A. Einstein. Quantentheorie des einatomigen idealen Gases. *Sitzber. Kgl. Preuss. Akad. Wiss.*, pages 3–14, 1925.

[4] C. J. Foot. *Atomic Physics*. Oxford University Press, Oxford, 2005.

[5] R. Nolli, M. Venturelli, L. Marmugi, A. Wickenbrock, and F. Renzoni. Compact setup for the production of ^{87}Rb Bose-Einstein condensates in a hybrid trap. *Rev. of Sc. Instr.*, 87(8):083102, 2016.

[6] D. J. Wineland, R. E. Drullinger, and F. L. Walls. Radiation-pressure cooling of bound resonant absorbers. *Phys. Rev. Lett.*, 40:1639–1642, 1978.

[7] H. F. Hess. Evaporative cooling of magnetically trapped and compressed spin-polarized hydrogen. *Phys. Rev. B*, 34:3476–3479, 1986.

[8] N. Masuhara, J. M. Doyle, J. C. Sandberg, D. Kleppner, T. J. Greytak, H. F. Hess, and G. P. Kochanski. Evaporative cooling of spin-polarized atomic hydrogen. *Phys. Rev. Lett.*, 61:935–938, 1988.

[9] M. H. Anderson, J. R. Ensher, M. R. Matthews, C. E. Wieman, and E. A. Cornell. Observation of Bose-Einstein Condensation in a Dilute Atomic Vapor. *Science*, 269:198 – 201, 1995.

[10] K. B. Davis, M. O. Mewes, M. R. Andrews, N. J. van Druten, D. S. Durfee, D. M. Kurn, and W. Ketterle. Bose-Einstein Condensation in a Gas of Sodium Atoms. *Phys. Rev. Lett.*, 75:3969–3973, 1995.

[11] C. C. Bradley, C. A. Sackett, J. J. Tollett, and R. G. Hulet. Evidence of Bose-Einstein Condensation in an Atomic Gas with Attractive Interactions. *Phys. Rev. Lett.*, 75:1687–1690, 1995.

[12] T.W. Hansch and A.L. Schawlow. Cooling of gases by laser radiation. *Opt. Com.*, 13(1):68 – 69, 1975.

[13] D. Wineland and H. Dehmelt. Proposed 1014 delta upsilon less than upsilon laser fluorescence spectroscopy on T1+ mono-ion oscillator III. In *Bull. Am. Ph. Soc.*, volume 20, pages 637–637, 1975.

[14] M. T. DePue, S. L. Winoto, D. J. Han, and D. S. Weiss. Transient compression of a mot and high intensity fluorescent imaging of optically thick clouds of atoms. *Opt. Com.*, 180(1):73 – 79, 2000.

[15] J. Dalibard and C. Cohen-Tannoudji. Laser cooling below the doppler limit by polarization gradients: simple theoretical models. *J. Opt. Soc. Am. B*, 6(11):2023–2045, 1989.

[16] P. D. Lett, R. N. Watts, C. I. Westbrook, W. D. Phillips, P. L. Gould, and H. J. Metcalf. Observation of atoms laser cooled below the doppler limit. *Phys. Rev. Lett.*, 61:169–172, 1988.

[17] J. Reichel, W. Hänsel, and T. W. Hänsch. Atomic micromanipulation with magnetic surface traps. *Phys. Rev. Lett.*, 83:3398–3401, 1999.

[18] A. L. Migdall, J. V. Prodan, W. D. Phillips, T. H. Bergeman, and H. J. Metcalf. First observation of magnetically trapped neutral atoms. *Phys. Rev. Lett.*, 54:2596–2599, 1985.

[19] E. Majorana. Oriented atoms in variable magnetic field. *Il Nuovo Cimento*, 9:43–50, 1932.

[20] W. Petrich, M. H. Anderson, J. R. Ensher, and E. A. Cornell. Stable, tightly confining magnetic trap for evaporative cooling of neutral atoms. *Phys. Rev. Lett.*, 74:3352–3355, 1995.

[21] T. Bergeman, G. Erez, and H. J. Metcalf. Magnetostatic trapping fields for neutral atoms. *Phys. Rev. A*, 35:1535–1546, 1987.

[22] C. J. Myatt, E. A. Burt, R. W. Ghrist, E. A. Cornell, and C. E. Wieman. Production of Two Overlapping Bose-Einstein Condensates by Sympathetic Cooling. *Phys. Rev. Lett.*, 78:586–589, 1997.

[23] T. Esslinger, I. Bloch, and T. W. Hänsch. Bose-Einstein condensation in a quadrupole-Ioffe-configuration trap. *Phys. Rev. A*, 58:R2664–R2667, 1998.

[24] M.-O. Mewes, M. R. Andrews, N. J. van Druten, D. M. Kurn, D. S. Durfee, and W. Ketterle. Bose-Einstein Condensation in a Tightly Confining dc Magnetic Trap. *Phys. Rev. Lett.*, 77:416–419, 1996.

[25] R. Grimm, M. Weidemüller, and Y. B. Ovchinnikov. Optical Dipole Traps for Neutral Atoms. *Adv. in At. Mol. and Opt. Ph.*, 42:95–170, 2000.

[26] M. D. Barrett, J. A. Sauer, and M. S. Chapman. All-Optical Formation of an Atomic Bose-Einstein Condensate. *Phys. Rev. Lett.*, 87:010404, 2001.

[27] C. S. Adams, H. J. Lee, N. Davidson, M. Kasevich, and S. Chu. Evaporative cooling in a crossed dipole trap. *Phys. Rev. Lett.*, 74:3577–3580, 1995.

[28] S. Inouye, M. R. Andrews, J. Stenger, H-J. Miesner, D.M. Stamper-Kurn, and W. Ketterle. Observation of Feshbach resonances in a Bose–Einstein condensate. *Nature*, 392(6672):151, 1998.

[29] D. Jacob, E. Mimoun, L. De Sarlo, M. Weitz, J. Dalibard, and F. Gerbier. Production of sodium Bose-Einstein condensates in an optical dimple trap. *New Journal of Physics*, 13(6):065022, 2011.

[30] Lin, Y.-J. and Perry, A. R. and Compton, R. L. and Spielman, I. B. and Porto, J. V. Rapid production of ^{87}Rb Bose-Einstein condensates in a combined magnetic and optical potential. *Phys. Rev. A*, 79:063631, 2009.

[31] C. J. Myatt, N. R. Newbury, R. W. Ghrist, S. Loutzenhiser, and C. E. Wieman. Multiply loaded magneto-optical trap. *Opt. Lett.*, 21(4):290–292, 1996.

[32] W. D. Phillips and H. Metcalf. Laser deceleration of an atomic beam. *Phys. Rev. Lett.*, 48:596–599, 1982.

[33] E. A. Hinds and I. G. Hughes. Magnetic atom optics: mirrors, guides, traps, and chips for atoms. *Journ. of Ph. D: Appl. Ph.*, 32(18):R119, 1999.

[34] J. Fortágh and C. Zimmermann. Magnetic microtraps for ultracold atoms. *Rev. Mod. Phys.*, 79:235–289, 2007.

[35] E. A. Hinds, C. J. Vale, and M. G. Boshier. Two-wire waveguide and interferometer for cold atoms. *Phys. Rev. Lett.*, 86:1462–1465, 2001.

[36] T. van Zoest, N. Gaaloul, Y. Singh, H. Ahlers, W. Herr, S. T. Seidel, W. Ertmer, E. Rasel, M. Eckart, E. Kajari, S. Arnold, G. Nandi, W. P. Schleich, R. Walser, A. Vogel, K. Sengstock, K. Bongs, W. Lewoczko-Adamczyk, M. Schiemangk, T. Schuldt, A. Peters, T. Könemann, H. Müntinga, C. Lämmerzahl, H. Dittus, T. Steinmetz, T. W. Hänsch, and J. Reichel. Bose-Einstein Condensation in Microgravity. *Science*, 328(5985):1540–1543, 2010.

[37] N. Abdul Wahab. *Transport of cold atoms in laser fields*. PhD thesis, University College London, 2013.

[38] Z. T. Lu, K. L. Corwin, M. J. Renn, M. H. Anderson, E. A. Cornell, and C. E. Wieman. Low-velocity intense source of atoms from a magneto-optical trap. *Phys. Rev. Lett.*, 77:3331–3334, 1996.

[39] J. L. Roberts, N. R. Claussen, James P. Burke, Chris H. Greene, E. A. Cornell, and C. E. Wieman. Resonant Magnetic Field Control of Elastic Scattering in Cold ^{85}Rb. *Phys. Rev. Lett.*, 81:5109–5112, 1998.

[40] J. L. Roberts, N. R. Claussen, S. L. Cornish, and C. E. Wieman. Magnetic field dependence of ultracold inelastic collisions near a feshbach resonance. *Phys. Rev. Lett.*, 85:728–731, 2000.

[41] S. L. Cornish, N. R. Claussen, J. L. Roberts, E. A. Cornell, and C. E. Wieman. Stable ^{85}Rb Bose-Einstein Condensates with Widely Tunable Interactions. *Phys. Rev. Lett.*, 85:1795–1798, 2000.

[42] S. Burger, K. Bongs, S. Dettmer, W. Ertmer, K. Sengstock, A. Sanpera, G. V. Shlyapnikov, and M. Lewenstein. Dark Solitons in Bose-Einstein Condensates. *Phys. Rev. Lett.*, 83:5198–5201, 1999.

[43] Immanuel Bloch. Ultracold quantum gases in optical lattices. *Nature Physics*, 1:23, 2005.

[44] M. Greiner, O. Mandel, T. Esslinger, T. W. Hnsch., and I. Bloch. Quantum phase transition from a superfluid to a mott insulator in a gas of ultracold atoms. *Nature*, 415:39, 2002.

[45] D. Jaksch, H.-J. Briegel, J. I. Cirac, C. W. Gardiner, and P. Zoller. Entanglement of atoms via cold controlled collisions. *Phys. Rev. Lett.*, 82:1975–1978, 1999.

[46] M. Schiavoni, L. Sanchez-Palencia, F. Renzoni, and G. Grynberg. Phase control of directed diffusion in a symmetric optical lattice. *Phys. Rev. Lett.*, 90:094101, 2003.

[47] T. Salger, S. Kling, T. Hecking, C. Geckeler, L. Morales-Molina, and M. Weitz. Directed transport of atoms in a hamiltonian quantum ratchet. *Science*, 326(5957):1241–1243, 2009.

[48] S. Denisov, S. Flach, and P. Hanggi. *Transporting Cold Atoms in Optical Lattices with Ratchets: Mechanisms and Symmetries, pages 181-194*. Springer Berlin Heidelberg, 2010.

[49] M. R. Andrews, C. G. Townsend, H.-J. Miesner, D. S. Durfee, D. M. Kurn, and W. Ketterle. Observation of Interference Between Two Bose Condensates. *Science*, 275(5300):637–641, 1997.

[50] I. Bloch, T. Haensch, and T. Esslinger. Measurement of the spatial coherence of a trapped Bose gas at the phase transition. *Nature*, 403:166–70, 2000.

[51] M.-O. Mewes, M. R. Andrews, D. M. Kurn, D. S. Durfee, C. G. Townsend, and W. Ketterle. Output Coupler for Bose-Einstein Condensed Atoms. *Phys. Rev. Lett.*, 78:582–585, 1997.

[52] W. Ketterle. Nobel lecture: When atoms behave as waves: Bose-Einstein condensation and the atom laser. *Rev. Mod. Phys.*, 74:1131–1151, 2002.

[53] M. R. Matthews, B. P. Anderson, P. C. Haljan, D. S. Hall, C. E. Wieman, and E. A. Cornell. Vortices in a Bose-Einstein Condensate. *Phys. Rev. Lett.*, 83:2498–2501, 1999.

[54] J. R. Abo-Shaeer, C. Raman, J. M. Vogels, and W. Ketterle. Observation of Vortex Lattices in Bose-Einstein Condensates. *Science*, 292(5516):476–479, 2001.

[55] B. DeMarco and D. S. Jin. Onset of fermi degeneracy in a trapped atomic gas. *Science*, 285(5434):1703–1706, 1999.

[56] R. Wynar, R. S. Freeland, D. J. Han, C. Ryu, and D. J. Heinzen. Molecules in a Bose-Einstein Condensate. *Science*, 287(5455):1016–1019, 2000.

[57] S. Jochim, M. Bartenstein, A. Altmeyer, G. Hendl, S. Riedl, C. Chin, J. Hecker Denschlag, and R. Grimm. Bose-Einstein Condensation of Molecules. *Science*, 302(5653):2101–2103, 2003.

[58] N. Ramsey. *Molecular Beams - International series of monographs on physics.* OUP Oxford, 1956.

[59] S. Gupta, K. Dieckmann, Z. Hadzibabic, and D. E. Pritchard. Contrast Interferometry using Bose-Einstein Condensates to Measure h/m and α. *Phys. Rev. Lett.*, 89:140401, 2002.

[60] H. G. Dehmelt. Modulation of a light beam by precessing absorbing atoms. *Phys. Rev.*, 105:1924–1925, 1957.

[61] W. E. Bell and A. L. Bloom. Optical detection of magnetic resonance in alkali metal vapor. *Phys. Rev.*, 107:1559–1565, 1957.

[62] C. Cohen-Tannoudji and A. Kastler. I optical pumping. In E. Wolf, editor, *I Optical Pumping*, Progress in Optics, pages 1 – 81. Elsevier, 1966.

[63] W. Happer. Optical pumping. *Rev. Mod. Phys.*, 44:169–249, 1972.

[64] P. Treutlein, P. Hommelhoff, T. Steinmetz, T. W. Hänsch, and J. Reichel. Coherence in microchip traps. *Phys. Rev. Lett.*, 92:203005, 2004.

[65] J. M. Higbie, L. E. Sadler, S. Inouye, A. P. Chikkatur, S. R. Leslie, K. L. Moore, V. Savalli, and D. M. Stamper-Kurn. Direct Nondestructive Imaging of Magnetization in a Spin-1 Bose-Einstein Gas. *Phys. Rev. Lett.*, 95:050401, 2005.

[66] T. Isayama, Y. Takahashi, N. Tanaka, K. Toyoda, K. Ishikawa, and T. Yabuzaki. Observation of Larmor spin precession of laser-cooled Rb atoms via paramagnetic Faraday rotation. *Phys. Rev. A*, 59:4836–4839, 1999.

[67] S. Franke-Arnold, M. Arndt, and A. Zeilinger. Magneto-optical effects with cold lithium atoms. *Journ. of Phys. B: At., Mol. and Opt. Phys.*, 34(12):2527, 2001.

[68] G. Labeyrie, C. Miniatura, and R. Kaiser. Large faraday rotation of resonant light in a cold atomic cloud. *Phys. Rev. A*, 64:033402, 2001.

[69] M. Vengalattore, J. M. Higbie, S. R. Leslie, J. Guzman, L. E. Sadler, and D. M. Stamper-Kurn. High-Resolution Magnetometry with a Spinor Bose-Einstein Condensate. *Phys. Rev. Lett.*, 98:200801, 2007.

[70] J. C. Allred, R. N. Lyman, T. W. Kornack, and M. V. Romalis. High-sensitivity atomic magnetometer unaffected by spin-exchange relaxation. *Phys. Rev. Lett.*, 89:130801, 2002.

[71] I. M. Savukov, S. J. Seltzer, M. V. Romalis, and K. L. Sauer. Tunable atomic magnetometer for detection of radio-frequency magnetic fields. *Phys. Rev. Lett.*, 95:063004, 2005.

[72] W. Chalupczak, R. M. Godun, S. Pustelny, and W. Gawlik. Room temperature femtotesla radio-frequency atomic magnetometer. *Appl. Phys. Lett.*, 100(24):242401, 2012.

[73] M. P. Ledbetter, V. M. Acosta, S. M. Rochester, D. Budker, S. Pustelny, and V. V. Yashchuk. Detection of radio-frequency magnetic fields using nonlinear magneto-optical rotation. *Phys. Rev. A*, 75:023405, 2007.

[74] D. A. Keder, D. W. Prescott, A. W. Conovaloff, and K. L. Sauer. An unshielded radio-frequency atomic magnetometer with sub-femtotesla sensitivity. *AIP Advances*, 4(12):127159, 2014.

[75] S.-K. Lee, K. L. Sauer, S. J. Seltzer, O. Alem, and M. V. Romalis. Subfemtotesla radio-frequency atomic magnetometer for detection of nuclear quadrupole resonance. *Appl.Phys. Lett.*, 89(21):214106, 2006.

[76] S. J. Seltzer. *Developments in Alkali-Metal Atomic Magnetometry*. PhD thesis, Princeton University, 2008.

[77] M. Stahler, S. Knappe, C. Affolderbach, W. Kemp, and R. Wynands. Picotesla magnetometry with coherent dark states. *Europhys. Lett.*, 54(3):323, 2001.

[78] D. Budker, D. F. Kimball, S. M. Rochester, V. V. Yashchuk, and M. Zolotorev. Sensitive magnetometry based on nonlinear magneto-optical rotation. *Phys. Rev. A*, 62:043403, 2000.

[79] P. D. D. Schwindt, B. Lindseth, S. Knappe, V. Shah, J. Kitching, and Li-A Liew. Chip-scale atomic magnetometer with improved sensitivity by use of the Mx technique. *Appl. Phys. Lett.*, 90(8):081102, 2007.

[80] L. Marmugi, L. Gori, S. Hussain, C. Deans, and F. Renzoni. Remote detection of rotating machinery with a portable atomic magnetometer. *Appl. Opt.*, 56:743, 2017.

[81] P. W. Anderson and J. M. Rowell. Probable observation of the josephson superconducting tunneling effect. *Phys. Rev. Lett.*, 10:230–232, 1963.

[82] Prof. Dr. John Clarke Prof. Dr. Alex I. Braginski. *The SQUID Handbook: Fundamentals and Technology of SQUIDs and SQUID Systems*. Wiley-VCH, 2005.

[83] A. Weis. Optically pumped alkali magnetometers for biomedical applications. *Europhys. News*, 43(3):20–23, 2012.

[84] V. V. Yashchuk, J. Granwehr, D. F. Kimball, S. M. Rochester, A. H. Trabesinger, J. T. Urban, D. Budker, and A. Pines. Hyperpolarized xenon nuclear spins detected by optical atomic magnetometry. *Phys. Rev. Lett.*, 93:160801, 2004.

[85] I. M. Savukov and M. V. Romalis. NMR Detection with an Atomic Magnetometer. *Phys. Rev. Lett.*, 94:123001, 2005.

[86] G. Bison, R. Wynands, and A. Weis. A laser-pumped magnetometer for the mapping of human cardiomagnetic fields. *Appl, Phys. B*, 76(3):325–328, 2003.

[87] H. Xia, A. Ben-Amar Baranga, D. Hoffman, and M. V. Romalis. Magnetoencephalography with an atomic magnetometer. *Appl. Phys. Lett.*, 89(21):211104, 2006.

[88] E. Boto, N. Holmes, J. Leggett, G. Roberts, V. Shah, S. S. Meyer, L. D. Muoz, K. J. Mullinger, T. M. Tierney, S. Bestmann, G. R. Barnes, R. Bowtell, and M. J. Brookes. Moving magnetoencephalography towards real-world applications with a wearable system. *Nature*, 555:657–661, 2018.

[89] L. Marmugi and F. Renzoni. Optical magnetic induction tomography of the heart. *Sc. Rep.*, 6:23962, 2016.

[90] D. A. Steck. Rubidium 87 D Line Data. Technical report, http://steck.us/alkalidata, revision 2.1.4, 2010.

[91] J.-F. Clément, J.-P. Brantut, M. Robert-de Saint-Vincent, R. A. Nyman, A. Aspect, T. Bourdel, and P. Bouyer. All-optical runaway evaporation to Bose-Einstein condensation. *Phys. Rev. A*, 79:061406, 2009.

[92] C.-L. Hung, X. Zhang, N. Gemelke, and C. Chin. Accelerating evaporative cooling of atoms into Bose-Einstein condensation in optical traps. *Phys. Rev. A*, 78:011604, 2008.

[93] S. R. De Groot, G. J. Hooyman, and C. A. Ten Seldam. On the Bose-Einstein condensation. *Proc. of the Royal Soc. of London A: Mathematical, Physical and Engineering Sciences*, 203(1073):266–286, 1950.

[94] F. Dalfovo, S. Giorgini, Lev P. Pitaevskii, and S. Stringari. Theory of Bose-Einstein condensation in trapped gases. *Rev. Mod. Phys.*, 71:463–512, 1999.

[95] K. Huang. *Statistical Mechanics*. Wiley and Sons, second edition, 1987.

[96] C. Pethick and H. Smith. *Bose-Einstein Condensation in Dilute Gases*. Cambridge University Press, 2002.

[97] N. N. Bogolyubov. On the theory of superfluidity. *J. Phys.(USSR)*, 11:23–32, 1947.

[98] E. P. Gross. Structure of a quantized vortex in boson systems. *Il Nuovo Cimento (1955-1965)*, 20(3):454–477, 1961.

[99] L..P. Pitaevskii. Vortex lines in an imperfect Bose gas. *Sov. Phys. JETP*, 13(2):451–454, 1961.

[100] T. A. Savard, K. M. O'Hara, and J. E. Thomas. Laser-noise-induced heating in far-off resonance optical traps. *Phys. Rev. A*, 56:R1095–R1098, 1997.

[101] M. E. Gehm, K. M. O'Hara, T. A. Savard, and J. E. Thomas. Dynamics of noise-induced heating in atom traps. *Phys. Rev. A*, 58:3914–3921, 1998.

[102] H. C. W. Beijerinck. Rigorous calculation of heating in alkali-metal traps by background gas collisions. *Phys. Rev. A*, 61:033606, 2000.

[103] B. Frohlich, T. Lahaye, B. Kaltenhuser, H. Kubler, S. Muller, T. Koch, M. Fattori, and T. Pfau. Two-frequency acousto-optic modulator driver to improve the beam pointing stability during intensity ramps. *Rev. of Sc. Instr.*, 78:043101 – 043101, 05 2007.

[104] W. D. Phillips. Nobel lecture: Laser cooling and trapping of neutral atoms. *Rev. Mod. Phys.*, 70:721–741, 1998.

[105] M. L. Harris. *Realisation of a cold mixture of rubidium and caesium*. PhD thesis, Durham University, 2008.

[106] T. Pyragius. Developing and building an absorption imaging system for Ultracold Atoms. *ArXiv e-prints*, 2012.

[107] H. J. Metcalf and P. van der Straten. Laser cooling and trapping of atoms. *Journ. Opt. Soc. Am. B*, 20(5):887–908, 2003.

[108] W. Petrich, M. H. Anderson, J. R. Ensher, and E. A. Cornell. Behavior of atoms in a compressed magneto-optical trap. *Journ. Opt. Soc. Am. B*, 11(8):1332–1335, 1994.

[109] A. L. Marchant. *Formation of bright solitary matter-waves*. PhD thesis, Durham University, 2012.

[110] C. J. Erickson. *Measurements of the magnetic field dependence of the spin relaxation rate in alkali metal vapors.* PhD thesis, Princeton University, 2000.

[111] F. Bloch. Nuclear induction. *Phys. Rev.*, 70:460–474, 1946.

[112] S. Appelt, A. Ben-Amar Baranga, C. J. Erickson, M. V. Romalis, A. R. Young, and W. Happer. Theory of spin-exchange optical pumping of ^{3}He and ^{129}Xe. *Phys. Rev. A*, 58:1412–1439, 1998.

[113] S. Pustelny, A. Wojciechowski, M. Gring, M. Kotyrba, J. Zachorowski, and W. Gawlik. Magnetometry based on nonlinear magneto-optical rotation with amplitude-modulated light. *Journ. of Appl. Phys.*, 103(6):063108, 2008.

[114] E. S. Robinson, H. G. Ensberg and Dehmelt H. G. Preservation of Spin State in Free Atom-Inert Surface Collisions. *Bull. of the Am. Phys. Soc.*, 3(1)(9), 1958.

[115] M. A. Bouchiat and J. Brossel. Relaxation of Optically Pumped Rb Atoms on Paraffin-Coated Walls. *Phys. Rev.*, 147:41–54, 1966.

[116] S. Imanishi, U. Tanaka, and S. Urabe. Frequency Stabilization of Diode Laser Using Dichroic-Atomic-Vapor Laser Lock Signals and Thin Rb Vapor Cell. *Jap. Journ. of Appl. Phys.*, 44(9R):6767, 2005.

[117] A. Millett-Sikking, I. G. Hughes, P. Tierney, and S. L. Cornish. DAVLL lineshapes in atomic rubidium. *Journ. of Phys. B: At., Mol. and Opt. Phys.*, 40(1):187, 2007.